Characteristics, Variability and Impact of Atmospheric Gravity Waves in the Thermosphere-Ionosphere as determined from Dynasonde Data

by

Cătălin Negrea

B.Eng. University of Bucharest, 2010

M.S. University of Colorado, 2012

A thesis submitted to the Faculty of the Graduate School of the

University of Colorado in partial fulfillment

of the requirements for the degree of

Doctor in Philosophy

Department of Electrical, Computer and Energy Engineering

August 2016

This thesis entitled

Characteristics, Variability and Impact of Atmospheric Gravity Waves in the Thermosphere-Ionosphere as determined from Dynasonde Data

Written by Cătălin Negrea

has been approved for the Department of Electrical, Computer and Energy Engineering

____

Nikolay A. Zabotin

____

Timothy J. Fuller-Rowell

Date _________________

The final copy of this thesis has been examined by the signatories, and we

Find that both the content and the form meet acceptable presentation standards

Of scholarly work in the above mentioned discipline.

Negrea, Cătălin (Ph.D., Electrical, Computer and Energy Engineering)

Characteristics, Variability and Impact of Atmospheric Gravity Waves in the thermosphere-Ionosphere as determined from Dynasonde Data

Thesis directed by Professor Nikolay Zabotin

Acoustic gravity waves (AGWs) and associated travelling ionospheric disturbances (TIDs) have a significant impact on the thermosphere-ionosphere, both by increasing ionospheric variability and transporting energy and momentum. This work demonstrates the use of Dynasonde data products (electron density, ionospheric tilts, Doppler speed) for the study of TIDs and AGWs. The features of Dynasonde-capable instruments make them uniquely fit for this purpose, allowing for the complete characterization of TID activity over large time periods. New spectral analysis techniques are developed, allowing for the accurate characterization of the TID spectrum from periods of several minutes (AGWs) to harmonics of 24 hours (atmospheric tides). A new approach for determining the mean Power Spectral Density (PSD) of TIDs is developed based on the Lomb-Scargle and Welch methods and its accuracy is demonstrated using both synthetic data and ionospheric tilt data from Wallops Island, VA. The method is then used to determine the seasonal variations in the ionosphere due to AGWs. PSDs and integral PSDs of the ionospheric tilts and Doppler speed are used to highlight the presence of a well-known winter peak in TID activity at mid-latitudes in the northern hemisphere, and also a less documented summer peak. The full set of propagation parameters (frequency, horizontal and vertical wavelength, propagation azimuth) is determined using the electron density and tilt data from Wallops Island. Using these results and the Whole Atmosphere Model (WAM), the agreement between the TID parameters and the gravity wave dispersion relation is demonstrated convincingly within the uncertainty for the first time. This further proves that the observed TIDs are caused by underlying AGWs. Using a month-long dataset obtained in October 2013 at Wallops Island, the statistical distributions of the propagation azimuth, vertical and horizontal wavelength and horizontal phase speed are studied, including their variation with altitude. The impact of AGW dissipation on the background thermosphere-ionosphere is investigated using gravity wave polarization relations and a model of the neutral-ion coupling, obtaining estimates of the momentum flux. In addition to the geophysical results obtained here, the general character of the methods used to obtain them will allow for further studies using Dynasonde data.

Acknowledgments

I would like to thank Nikolay Zabotin for the guidance and advice he provided, from introducing me to the Dynasonde technique of ionospheric sounding, to teaching me how to prepare successful conference presentations and journal articles.

I would also like to thank Tim Fuller-Rowell for his advice, support and patience. In particular, his approach to understanding complex scientific problems has been one of the most valuable skills I learned as a Ph.D. student. I also appreciate that both Nikolay and Tim gave me considerable latitude in selecting a thesis topic, while also allowing me to explore additional scientific topics that are of interest to me.

I would like to thank Albin Gasiewski for the guidance he provided as my academic advisor. He helped me understand exactly what a Ph.D. thesis should be and what makes a good thesis topic.

I am deeply grateful to Mihail Codrescu for his mentoring and help. My previous work with him was one of the factors in my decision to pursue a Ph.D. at the University of Colorado.

I would also like to extend my gratitude to Terrence Bullett, Rashid Akmaev, Mariangel Fedrizzi, Tzu-Wei Fang and Valery Yudin for helping me better understand the physics of the thermosphere-ionosphere system. And, I would like to thank Karen O'Loughlin for her help in developing my writing skills.

Finally, I would like to thank my committee members, Nikolay, Tim, Mihail, Al, Scott Palo and Edward Kuester. The time and effort that they invested into the proper evaluation of this thesis is greatly appreciated.

This work has been supported by the Cooperative Institute for Research in Environmental Sciences (CIRES) of CU-Boulder, by NASA through grant number NNX11A061G, by the Air Force Office of Scientific Research (AFOSR) through grant number FA9550-07-1-0565, and by the Office of Naval Research - Basic Research Challenge (ONR-BRC) through grant number N000141310348.

Contents

List of Tables

List of Figures

Chapter 1

INTRODUCTION

Acoustic gravity waves (AGWs) are known to have a significant impact on atmospheric dynamics. They are ubiquitous throughout all atmospheric regions but their characteristics can vary significantly depending on their source and background atmospheric conditions. The present work is focused on wave activity in the thermosphere-ionosphere system and in particular the bottom-side ionospheric *F*-layer. The principal information source used will be measurements from Dynasonde-capable instruments at Wallops Island, VA (37.85° N, 75.47° W), San Juan, PR (18.45° N, 66.07° W), and Tromso, Norway. In addition, model simulations are performed using the physics-based Whole Atmosphere Model (WAM) and the Global Ionosphere Plasmasphere (GIP) model, and their results are used to both describe the state of the background thermosphere-ionosphere and to investigate some aspects of wave propagation.

Waves propagating in the thermosphere differ from those in the lower atmospheric regions due to the much lower background density, the high variability of all background parameters, and the high degree of ionization (e.g., compared to the mesosphere). The medium of propagation is no longer an ideal fluid since neutral atoms and molecules collide with the ionized particles inducing perturbations of the ionospheric parameters. These perturbations can be used to detect wave activity using Travelling Ionospheric Disturbances (TIDs) as tracers. Although this approach can be used in conjunction with a number of remote-sensing techniques, our knowledge of AGW activity and its impact on the thermosphere has significant gaps.

Several remote sensing techniques are being used for the study of thermospheric AGWs (Figure 1.1): Incoherent Scatter Radars or ISRs (*Djuth et al*., 2010; *Ma et al*., 1997; *Nicolls et al*., 2004; *Nicolls and Heinselmann*, 2007), the Super Dual Auroral Radar (SuperDARN) Network (*Bristow et al*., 1994; *Frissell et al*., 2014, 2016; *Grocott et al*., 2013; *Ishida et al*., 2008), all-sky airglow imagers (*Shiokawa et al*., 2003), GPS Total Electron Content (*Afraimovich et al*., 1998, 1999; *Otsuka et al*., 2013; *Saito et al*., 1998) and Digisondes (*Forbes et al*., 2000). These are all ground-based, remote sensing techniques that can be used for the study of the ionospheric electron density in the 140–300 km altitude range. Ideally, one would need knowledge of five quantities in order to fully diagnose a given wave mode: frequency, amplitude, and the three wavevector components. The frequency and amplitude can be provided by all existing measurement techniques. The horizontal wavevector components can be derived using measurements in a horizontal plane and the vertical wave-vector can be obtained from height-stratified data. For statistically relevant studies, long term observations are necessary. Currently, no established remote sensing technique satisfies all the criteria described above. However, modern Dynasonde-capable instruments can obtain all necessary information to make valuable contributions to the ongoing discussion on gravity waves and their effect in the 140–300 km altitude range. It should also be mentioned that several other data sources can be used for the study of AGWs and TIDs at different altitudes, including LIDAR measurements below 120 km and data from the SWARM mission at 450 and 550 km. These are not discussed in detail as the altitude range they cover is significantly different from the 140–300 km range on which this work is focused.

The first and main objective of this work is to demonstrate for the first time the use of Dynasonde data products for the study of wave activity in the thermosphere-ionosphere. Dynasonde-capable instruments have been in operation for decades, but the use of these data for gravity wave studies of this kind is entirely new. The unique characteristics of the Dynasonde technique introduce unique problems that must be addressed.

Due to the natural ionospheric variability, measurements at any constant altitude contain significant data gaps of various size and distribution, which can vary depending on both solar and geomagnetic forcings or the very wave activity that is the focus of this study. **The second objective** of this work is to develop accurate spectral analysis tools suited for such extreme data gaps, and demonstrate their use for the analysis of Dynasonde data.

The third objective of this work is to obtain the full set of parameters (amplitude, vertical and horizontal wavelength, propagation direction, frequency) characterizing the observed TIDs and AGWs, demonstrate their agreement with gravity wave theory, and investigate their statistical distribution over time periods longer than a few days. Finally, in addition to the initial perturbations to the thermosphere-ionosphere, this work aims to obtain a first estimate of the impact of dissipating AGWs on the background system.

Dynasonde-capable instruments can operate on a continuous basis for very long time periods, and the datasets they provide are extensive. Manually processing these datasets is unfeasible except for small time intervals. A guiding principle of this work has been that results should be obtained by developing and then using automated data analysis techniques. This is also in-line with existing trends in the community. For example, the CEDAR Strategic Plan requires the development of precisely such methods (Strategic Thrust #6: "Develop advanced analysis techniques needed for effective fusion of observations into sophisticated inference models").

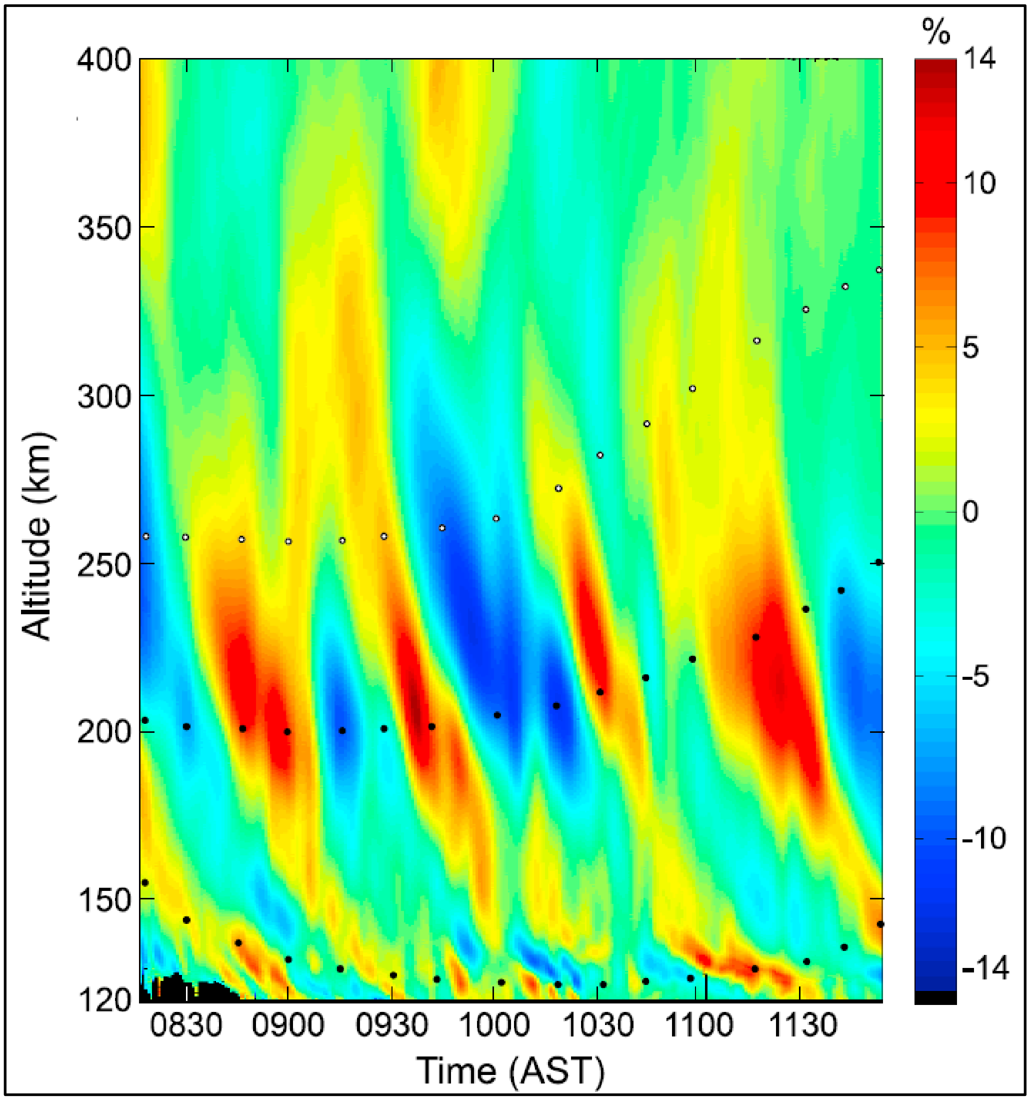

Figure 1.1. Relative perturbations in the detrended electron density measured at Arecibo on 6 June 2005. Note the Wave fronts due to Gravity Waves. "The white dots outlined in black show the location of the F region peak. Solid black dots represent the theoretically calculated altitudes for local peaks in percent n_e." Reproduced from Djuth et al. (2010).

This thesis is organized as follows. Chapter 2 provides a general overview of the thermosphere-ionosphere system and the main forcings that create its background structure. Chapter 3 describes the basic principles of operation of ionosonde instruments, and then in more detail the Dynasonde technique. The chapter ends with a comparative analysis of the advantages and drawbacks of the major remote sensing techniques used for studies of wave phenomena in the thermosphere-ionosphere above 120–140 km, compared to the advantages and drawbacks of the Dynasonde technique. Chapter 4 is focused on the spectral analysis of Dynasonde data, covering a wide range of frequencies. First, some of the inherent difficulties introduced by the non-uniform data sampling are discussed. A new method is developed to accurately evaluate the AGW spectrum in the presence of extensive data gaps. This is then used for the study the seasonal variability of AGWs and TIDs at Wallops Island and Tromso. The chapter ends with the investigation of the ionospheric signatures of tidal harmonics. Chapter 5 determines the full set of TID propagation characteristics, and demonstrates the quantitative agreement between them and the AGW dispersion relation. The statistical distribution associated with these parameters is then investigated over a broad altitude range. Chapter 6 uses the propagation parameters, AGW theory and WAM results to estimate the impact of dissipating AGWs on the background thermosphere-ionosphere. Finally, Chapter 7 summarizes the conclusions and discusses the possible continuations and applications of this work.

Chapter 2

THEMOSPHERE-IONOSPHERE

The region of interest for this study is the thermosphere-ionosphere, situated roughly between 100 and 600 km altitude. A number of reviews exist describing this region, amongst which are those by *Rishbeth and Garriott* (1969), *Bosinger et al.*, (2013), and *Fuller-Rowell* (2014). As the density in the region decreases exponentially with altitude and energy absorption per unit mass increases, the region is significantly more variable and dynamic when compared to lower atmospheric regions. Temperature increases with altitude and the dominant chemical components change from molecular oxygen and nitrogen to atomic oxygen (Figure 2.1). The plasma density varies strongly with altitude, with 4 plasma layers labelled, in the order of increasing altitude: D, E, F_1 and F_2 during daytime and generally a 2 layers at night: E and F_2 (Figure 2.2). In the vast majority of cases, the peak plasma density (the so called N_mF_2) is located in the F_2 layer, its altitude being referred to as the h_mF_2.

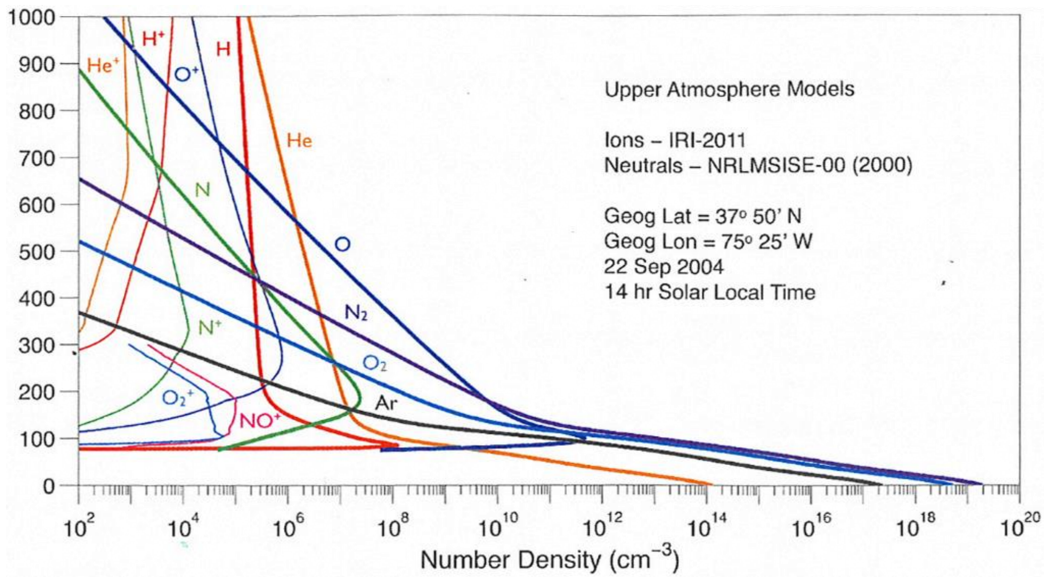

Figure 2.1. Major chemical components of the thermosphere-ionosphere, obtained using the IRI and MSIS empirical models. Reproduced from Bosinger et al. (2013).

The two main practical reasons why the region is important are satellite drag and communication and positioning. Neutral density is important in this context as it allows for an estimation of satellite drag and a better calculation of satellite orbits. Below 150 km, neutral density is too large to allow satellites without propulsion to maintain orbit. In this altitude range, a precise determination of satellite orbits is only possible with knowledge of thermospheric parameters. Satellite and ground-based communication and positioning signals interact with the ionospheric plasma. Their propagation can be drastically affected by changes in the ionospheric plasma density distribution. This can lead to decreased functionality of communication systems and large errors in positioning. In situations rather common during strong solar activity, these systems can end up failing, particularly at high latitudes.

The lower boundary of the thermosphere is the mesopause (the boundary between the mesosphere and the thermosphere), rigorously defined as the altitude where the temperature derivative with height changes its sign and the temperature starts to rapidly increase. The upper boundary of the thermosphere is the exobase (the boundary between the thermosphere and the exosphere), rigorously defined as the altitude above which the fluid approximation can no longer be used and the constituent atoms can be considered free particles, with a mean free path of the order of tens of kilometers. The altitude of these two boundaries can vary significantly, but they are roughly located at 100 and 600 km. In this volume, the ideal gas laws and fluid equations can be used.

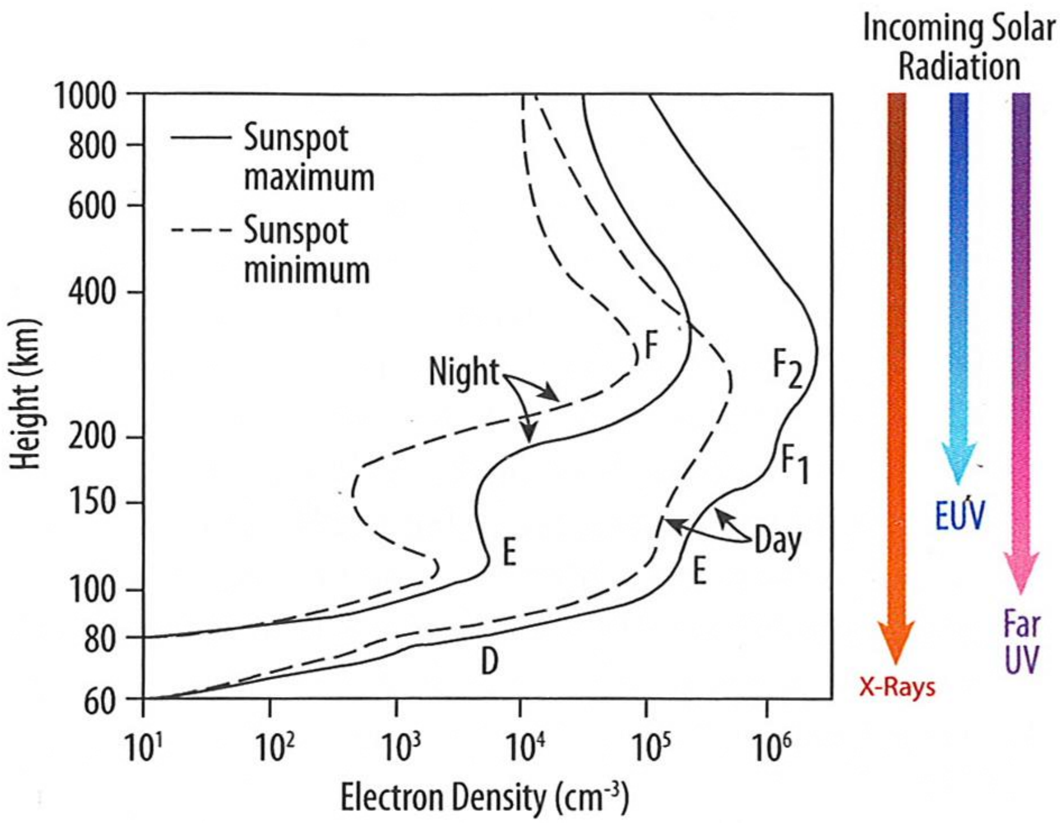

Figure 2.2. Major ionospheric layers. Reproduced from Bosinger et al. (2013).

The thermospheric gas is described by using the basic fluid properties: pressure (*p*), temperature (*T*), number and mass density (*n* and ρ), all related by the ideal gas law:

$$p = nk_BT \tag{2.1}$$

with $k_B = 1.3806488 * 10^{-23}\, J\, K^{-1}$ being the Boltzmann constant. The principle of hydrostatic equilibrium applies, meaning that the Earth's gravitational force requires that any change in pressure with height must be balanced by the mass of the fluid, or:

$$\frac{\partial p}{\partial z} = -\rho\, g \tag{2.2}$$

where z denotes the altitude and $g = 9.8\, m\, s^{-2}$ the Earth's gravitational acceleration (which can be safely assumed to be constant over the altitude range of interest). Equation (2.2) requires that the density of the neutral gas decrease exponentially with altitude, at a rate described by the so-called scale height (the altitude interval over which the neutral density decreases by a factor of $\frac{1}{e}$):

$$h = \frac{R\, T}{M\, g} \tag{2.3}$$

where h is the scale height, $R = 8.314\, J\, mol^{-1} K^{-1}$ is the ideal gas constant and M is the mean molecular mass in atomic mass units (1 a.m.u.=$1.67 * 10^{-27}\, kg$).

Both the thermosphere and ionosphere respond to changes in the levels of energy input. There are three main sources of energy and momenta for the system: solar irradiance in the 1-200 nm wavelength range, geomagnetic activity, and waves propagating from the lower atmosphere. Extreme Ultra Violet (EUV) and Ultra Violet (UV) radiation dissociates diatomic oxygen molecules and significantly increases the neutral gas temperature:

$$\mathrm{O_2} + h\nu \rightarrow \mathrm{O} + \mathrm{O} + thermal\ energy \tag{2.3}$$

As a result, atomic oxygen is the dominant specie above 150-200 km. The residual thermal energy in equation (2.3) is one of the causes for the increase in temperature in the thermosphere, along with residual heating due to photoionization and photoelectron heating. The region is characterized by much higher variability than the lower atmosphere due to the reduced density and due to changes of the EUV part of the spectra, both diurnal and associated with the solar cycle.

The ionospheric plasma generally amounts to less than 1% of the total mass contained in the thermosphere-ionosphere, but has considerable consequences for space-weather applications. The main mechanism for creating the ionosphere is photo-ionization, which depends the photon flux of the incoming radiation and on the density of the specific chemical species to be ionized. The ionization of atomic oxygen:

$$\mathrm{O} + h\nu \ \rightarrow \mathrm{O}^{+} + \mathrm{e}^{-} \tag{2.4}$$

is the main contributor to the creation of the F_1 Layer. The atomic oxygen density decreases with altitude while the EUV radiation intensity increases. The optimal altitude for the creation of O^{+} is reached around 150 km, with strong variations depending on location, solar activity and local time. A second, smaller ionization peak is reached around 100 km in the *E*-Layer. The dominant species here are NO^{+} and O_2^{+}, which result primarily through absorption of soft X-rays and EUV. These are not produced directly through photo-ionization as the corresponding cross-section is negligibly small. However, charge exchange can occur between molecular oxygen and nitrogen and atomic oxygen ions:

$$\mathrm{N}_2 + \mathrm{O}^{+} \ \rightarrow \mathrm{NO}^{+} + \mathrm{N} \tag{2.5}$$

$$\mathrm{O}_2 + \mathrm{O}^{+} \ \rightarrow \mathrm{O}_2^{+} + \mathrm{O} \tag{2.6}$$

Direct photo-ionization of atomic oxygen is a straightforward process. Direct radiative recombination of O^{+} is possible, but the reaction cross section is small. Loss of O^{+} is much more likely to occur through charge exchange producing $\mathrm{NO^+}$ and $\mathrm{O_2^+}$. These molecular ions have a shorter lifetime due to much more effective dissociative recombination:

$$\mathrm{O_2^+ + e^- \rightarrow O + O} \tag{2.7}$$

$$\mathrm{NO^+ + e^- \rightarrow N + O} \tag{2.8}$$

The peak altitude for O^+ production is in the *F*-Layer. The peak altitude for the loss of $\mathrm{O^+}$ through charge exchange is in the *E*-Layer due to the density of molecular species (equations 2.5 and 2.6, Figure 2.1). The amount of transport of $\mathrm{O^+}$ (both upward and downward) is thus vital for ionospheric dynamics. Meridional neutral winds and electric fields can impact the amount of diffusion of O^+. The balance between production, loss and transport create the height profile of plasma density (Figure 2.2). While the maximum production of plasma is in the F_1 Layer, the peak electron density is at higher altitudes, in the F_2 Layer, where the so-called hmF_2 (altitude of the F_2 peak) is located. At much higher altitudes (>500 km) the atomic hydrogen number density is high enough to reduce $\mathrm{O^+}$ density through charge exchange:

$$\mathrm{O^+ + H \rightarrow H^+ + O} \tag{2.9}$$

The ionosphere at high latitudes is a much more complex system than at low and mid latitudes. The magnetic dip angle is close to 90 degrees and for most practical purposes the field lines can be considered “open”. This allows for a strong coupling with the inner magnetosphere. Energetic electrons and associated field aligned currents are often the dominant source of ionization at high latitudes. The penetration altitude depends on the particles’ energy and on chemical composition. Electrons with energies of 10 KeV can reach altitudes of 100 km and produce molecular ions (NO^+ and O_2^+) while at higher altitudes (200-300 km) O^+ is produced by electrons with less than 1 keV. In addition to impact ionization, the coupling of the ionospheric plasma to the magnetosphere and the solar wind produces electric fields, with a dusk to dawn orientation.

Under the assumption of hydrostatic equilibrium, the “background” thermosphere responds instantaneously to solar radiation and particle precipitation. This approximation brakes down when considering spatial scales smaller than 100 km or time periods of tens of minutes or smaller. The convention made here is to define a “background” thermosphere and ionosphere, created by solar and geomagnetic forcings, and a superimposed “perturbation” due to Gravity Waves and associated Travelling Ionospheric Disturbances. The background ionosphere can generally be assumed not to contain large horizontal gradients (with the exception of two 1-2 hour intervals around local sunrise and sunset) and to vary slowly on time scales shorter than a few hours during both daytime and nighttime.

The basic physical processes responsible for controlling the background thermosphere-ionosphere are generally thought to be well understood. Over the past several decades, a number of global, coupled models of the thermosphere-ionosphere have been developed, such as the Coupled Thermosphere Ionosphere Plasmasphere model with electrodynamics (CTIPe) or the Thermosphere Ionosphere Electrodynamics General Circulation Model (TIEGCM). These models manage to capture the main characteristics of the response of the thermosphere-ionosphere to solar and geomagnetic activity in terms of composition and global dynamics, as well as large-scale gravity waves and TIDs. Based on this, the GIP model (which consists of the ionosphere, Plasmasphere and electrodynamics components of CTIPe) will be used here together with the WAM model to capture features of the background neutral density, temperature and winds.

In addition to photo ionization and particle precipitation, wave processes can impact the thermosphere-ionosphere by transporting energy and momentum between atmospheric regions, either vertically from the lower atmosphere (*Alexander and Rosenlof*, 2003; *Vadas et al*., 2014) or from high to mid and low latitudes (*Grocott et al.*, 2013; *Hernaandez-Pajares et al.*, 2012). Waves create perturbations in the atmospheric (density, neutral winds, temperature) and ionospheric (electron density, plasma drift, ionospheric tilts) parameters. Their characteristic periods of the wave phenomena of interest for this work range from harmonics of 24 hours (in the case of atmospheric tides) to minutes and tens of minutes (in the case of AGWs). Their corresponding horizontal spatial scales of AGWs extend from more than 1000 km (in the case of Large Scale TIDs, or LSTIDS) to tens of km. Finally, their typical vertical spatial scale is between several tens of km to 100-200 km (The statistical distribution of the horizontal and vertical wavelength of TIDs is addressed in Chapter 5). The primary sources of gravity waves are: wind shear over mountain ranges (orographic waves), waves from deep convection (both regular weather and dramatic events such as hurricanes) and heating in the auroral zones (*Yuan et al.*, 2005) due to particle precipitation. Other important category of waves in the thermosphere are secondary waves sourced by the dissipation of primary waves at lower altitudes (*Vadas et Liu.*, 2009), and waves from extreme events, such as earthquakes and tsunamis. In the middle atmosphere most wave dissipate when the background wind speed is equal to their phase speed. In the thermosphere above 150 km, viscosity and thermal diffusivity have a large importance (*Pitteway and* Hines, 1963; *Vadas and Fritts*, 2005; *Godin*, 2014).

CHAPTER 3

DYNASONDE TECHNIQUE

3.1. Ionospheric Sounding

Determining the plasma density (N_e), its variation with height and variability over both short and long time intervals is a topic of considerable interest. Measurements of the ionospheric N_e can be obtained using various remote sensing techniques. The results that are part of this thesis were obtained using the Dynasonde technique, so the focus here is on aspects regarding ionosondes in general and the Dynasonde technique in particular. An ionosonde is an HF radar that uses the principle of total internal reflection. To a good approximation, a plasma with a given number density will reflect electromagnetic pulses below a critical frequency and refract pulses with higher frequencies. This critical frequency is referred to as the plasma frequency and is proportional to the square root of the plasma density (*Chen*, 1983; *Gurnett and Bhattacharjee*, 2009):

$$f_p = \sqrt{\frac{N_e e^2}{\varepsilon_0 m_e} + \sum_{j=1}^{N} \frac{N_{ij} e^2}{\varepsilon_0 m_{ij}}} \tag{3.1}$$

where $m_e = 9.109 * 10^{-31}\ kg$ is the electron mass, $e = 1.602 * 10^{-19}\ C$ the electron charge, $e = 1.602 * 10^{-19}\ C$ the permittivity of free space, N_{ij} the number density of the ion specie j and m_{ij} the mass of the corresponding ion. The second term is a sum for all ion species present. Because of the much lower electron mass, the second term on the right hand side can be safely neglected, leading to the commonly used approximation:

$$f_p = 8.980\sqrt{N_e} \tag{3.2}$$

with N_e expressed in electrons per cubic m, and f_p in Hz.

Equation (3.1) ignores the effect of the Earth's geomagnetic field, and under this approximation, the refractive index (n) of an unmagnetized plasma depends on the pulse frequency and the plasma frequency (*Hunsucker*, 1991):

$$n^2 = 1 - \left(\frac{\omega_p}{\omega}\right)^2 \tag{3.3}$$

where $\omega_p = 2\pi f_p$ and ω is the pulse angular frequency. In the case of a magnetized plasma (such as the ionospheric plasma), the refractive index, *n*, depends on the polarization of the electric field vector of the radiated pulse via the Appleton-Hartree equation (*Hunsucker*, 1991):

$$n^2 = 1 - \frac{2\left(\frac{\omega p}{\omega}\right)^2\left(1-\left(\frac{\omega p}{\omega}\right)^2\right)}{2\left(1-\left(\frac{\omega p}{\omega}\right)^2\right)-\left(\frac{e}{m_e\omega}B_0\sin\theta\right)^2 \pm \sqrt{\left(\frac{e}{m_e\omega}B_0\sin\theta\right)^4+4\left(1-\left(\frac{\omega p}{\omega}\right)^2\right)^2\left(\frac{e}{m_e\omega}B_0\cos\theta\right)^2}} \tag{3.4}$$

The above formula shows a dependence of *n* on the angle *θ* between the direction of the wave vector and the ambient magnetic field. Total reflection will occur at two frequencies corresponding to the so called ordinary and extraordinary waves. The ordinary wave is the one that propagates most similarly to a wave in unmagnetized plasma. More importantly, the ordinary wave exhibits Right Hand Circular Polarization (RHCP) and the extraordinary Left Hand Circular Polarization (LHCP). The exact dependence of the critical frequency on plasma density can only be specified with complete knowledge of the magnetic field orientation and the direction of propagation. In practice, the Quasi-Transverse and Quasi-Longitudinal approximations can be used.

The basic operating principle of an ionosonde is to emit a sequence of pulses and record the time of arrival of the reflected pulse, for each of which a set of other characteristics can be determined (two angles of arrival, group range, Doppler, polarization, phase range and amplitude) based on phase variations. The group range vector, $\overrightarrow{p'}$, is the apparent position vector of the reflection point. Its modulus (also referred to as the virtual height) depends on the ionospheric plasma density below the reflection point through the refractive index of the plasma (*Hunsucker*, 1991):

$$\left|\overrightarrow{p'}\right| = \int_0^{z'} \frac{dz}{n(f,z)} \tag{3.5}$$

3.2. Dynasonde Method

Dynasonde-capable instruments use the “Stationary Phase Group Range” method, making use of precise phase measurements to determine $\left|\overrightarrow{p'}\right|$ with an accuracy down to a few tens of meters (*Paul et al.*, 1974). The phase transit time of a wave front (Δt), is used to define the so-called phase range (*Davies,* 1969):

$$|\vec{p}| = \frac{1}{2}\Delta t\, c = \frac{c}{\omega}\Phi(\omega) \tag{3.6}$$

where c being the speed of light and $\Phi(\omega)$ the phase difference between the transmitted and reflected pulse. The group range is then (*Davies*, 1969):

$$\left|\overrightarrow{p'}\right| = \frac{d}{d\omega}(\omega\,|\vec{p}|) = \frac{1}{2}c\,\frac{d\Phi}{d\omega} \tag{3.7}$$

The direction of $\overrightarrow{p'}$ (the angle of arrival) must necessarily be opposite to that of the wavevector $\vec{k}$ (*Paul et al.*, 1974):

$$\hat{p} = -\hat{k} = -\frac{c}{\omega}\vec{\nabla}\Phi \tag{3.8}$$

with $\hat{k} = \frac{\vec{k}}{|\vec{k}|}$, and $\hat{p} = \frac{\vec{p}}{|\vec{p}|}$. Equations (3.7) and (3.8) require precise phase measurements and impose requirements on the spacing of the receiving antennas and on the pulse set used by the instrument. The derivative with respect to spatial coordinates requires a set of closely spaced (when compared to the signal wavelength) receivers to determine the phase gradient. Calculating the phase derivative with respect to frequency requires a pulse sequence with groups of closely spaced frequencies. The data used here were collected using the so-called “Dynasonde B-mode” of operations (Figure 3.1), with groups of 8 pulses (referred to as a pulse set). Individual pulse envelopes are cosine squared with a temporal width of 60 μs, 30 KHz bandwidth and inter-pulse period of 5 ms.

To obtain results of the highest quality, the characteristics of an “echo” (ionospheric reflection) are determined using an entire pulse set. A least square fit procedure uses information on all pulses recorded by all receivers to simultaneously determine the echo parameters:

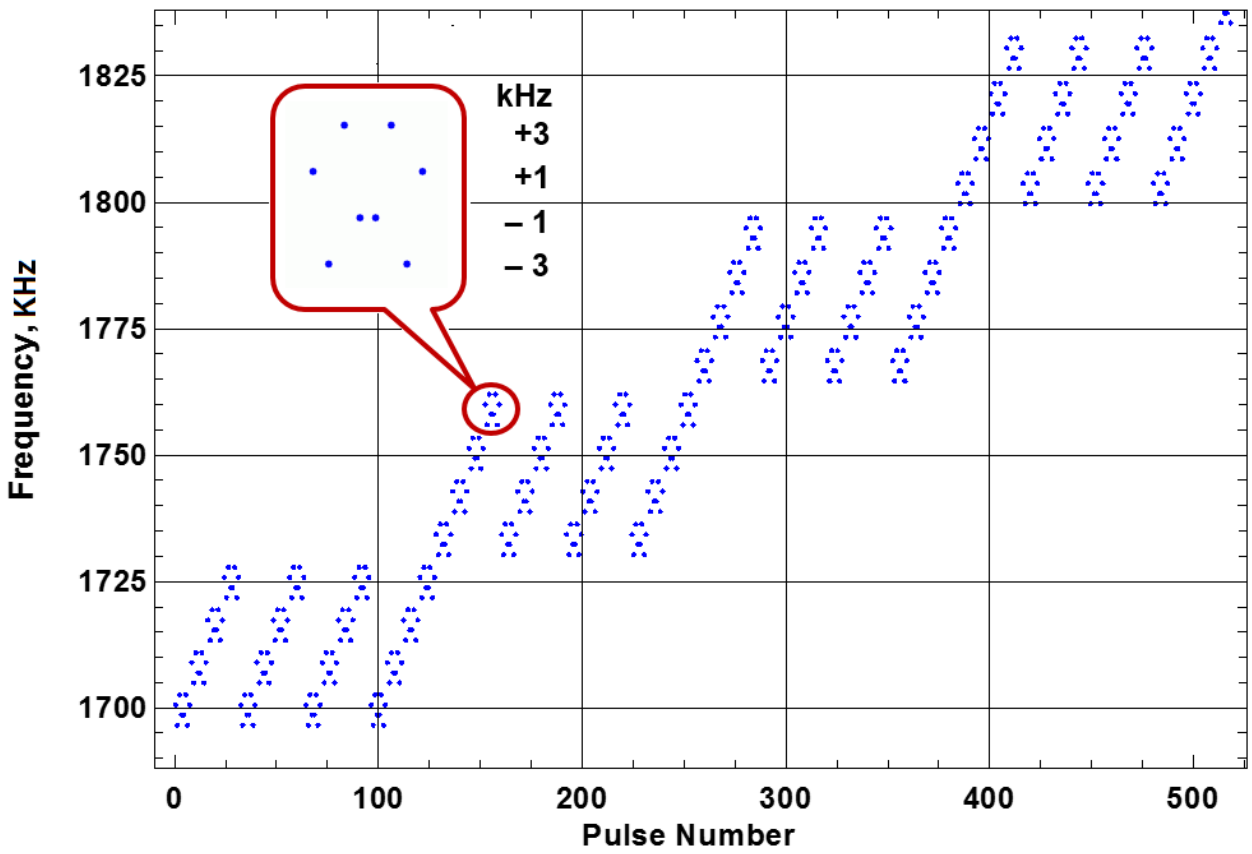

Figure 3.1. Schematic representation of the pulse set used in the Dynasonde "B" Mode of operations.

- The two angles of arrival, using equation (3.8), with an accuracy within 1°.
- Range of the echo, using equation (3.7), with an accuracy down to a few tens of meters.
- Echo Doppler velocity, from the phase differences among several pulse times
- Echo polarization rotation, using the orthogonality of east-west and north-south antennas
- Echo mean phase
- Associated phase error
- Mean echo amplitude

To obtain echoes at angles significantly off the vertical axis, the transmitting antenna needs to uniformly illuminate the ionosphere over a broad frequency range. Depending on geographical location, time of day and solar activity level, the peak plasma frequency can vary significantly. The radar hardware is capable of operating at frequencies of up to 25 MHz, which is higher than the typical peak plasma frequency and can account for cases of increase solar activity. Sounding the low-altitude ionosphere requires smaller frequencies (0.5-2 MHz), the lowest frequency that can be used being determined both by the antenna size and the ambient noise at the location of the instrument. The design requirements are then: an omnidirectional radiation pattern with similar performance for both LHCP and RHCP. Also, the peak gain should not vary significantly over the operating frequency range (Figure 3.2). The Wallops Island station utilizes a Zig-Zag Log Periodic Antenna, with 2 zig-zag planes arranged in a square, 76 m per side with the 4 supporting towers being 36 m high. Other designs can be used for the transmitting antenna, as long they provide a broad, vertically directed illumination pattern within the 1-25 MHz frequency band. The receiving arrays consist of several (8 at Wallops Island and San Juan and 6 at Tromso) dipole antennas, commonly grouped in two orthogonal lines with antenna separations varying between 10 and 140 m.

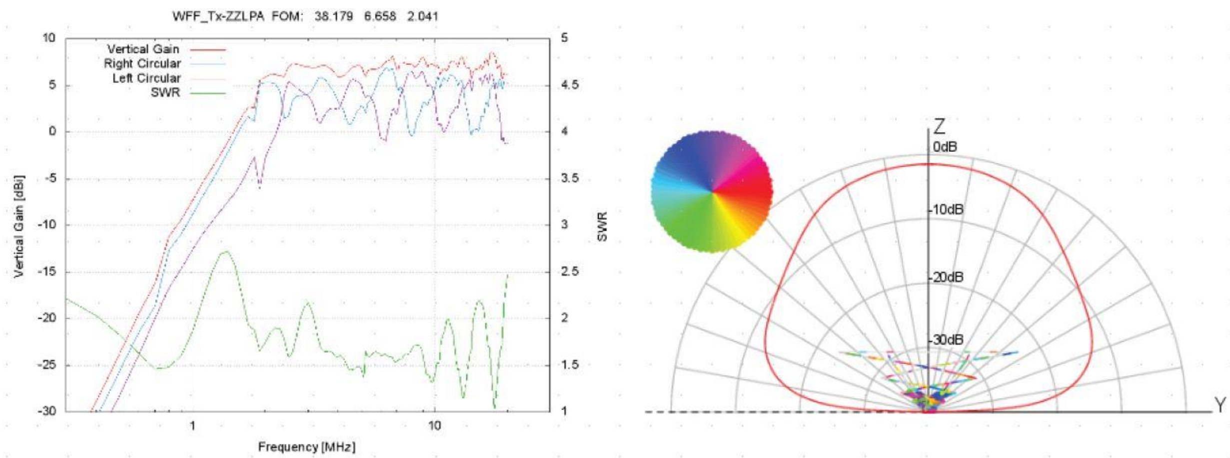

Figure 3.2. Left: Antenna peak gain as a function of frequency, with corrected vertical gain, LHCP and RHCP gain depicted. Gain is shown in dBi. Right: Gain pattern at 8.3 MHz. Courtesy of Terry Bullett (personal communication).

The full set of echoes obtained during a sounding session can be used to obtain the data products describing the local three-dimensional electron density distribution. For this, several processing steps are performed autonomously by the Dynasonde software, including phase-based echo recognition [*Wright and Pitteway*, 1999] and parameterization [*Wright and Pitteway*, 1979], echo classification into traces (such that reflections from the same ionospheric layer are ideally grouped into the same trace), and trace selection for higher-level analyses (such that traces due to sporadic plasma layers and secondary reflections are not used). The NeXtYZ inversion procedure (*Zabotin et al*, 2006) uses an iterative ray-tracing algorithm (Figure 3.3) to determine parameters of a three-dimensional model of the local plasma density called the Wedge-Stratified Ionosphere (Figure 3.4). In the WSI model, the plasma density surfaces are represented locally for small increments in plasma frequency f_p at a sequence of heights h_i along the vertical axis, by tilted sections of "frame" planes. The slope of each frame plane is characterized by the two horizontal components n_x, n_y of its normal unit vector, which are commonly referred to as the zonal and meridional ionospheric tilt. The two tilts are provided by NeXtYZ as separate outputs as they constitute distinct parameters of the WSI model, separate from the electron density. The normal to the plasma density surface determines the local direction of the total gradient in the layer:

$$\vec{n} = (n_x, n_y, n_z) = \frac{\vec{\nabla} N_e}{|\vec{\nabla} N_e|} \tag{3.10}$$

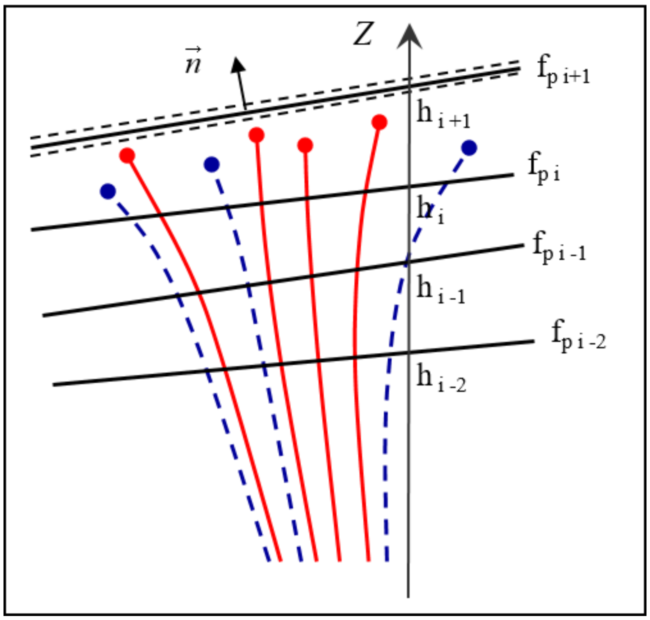

Figure 3.3. Schematic representation of the iterative ray-tracing algorithm used by NeXtYZ, showing both the ray-paths for ordinary (solid red lines) and extraordinary polarization (blue dashed lines). Adapted from Zabotin et al. (2006).

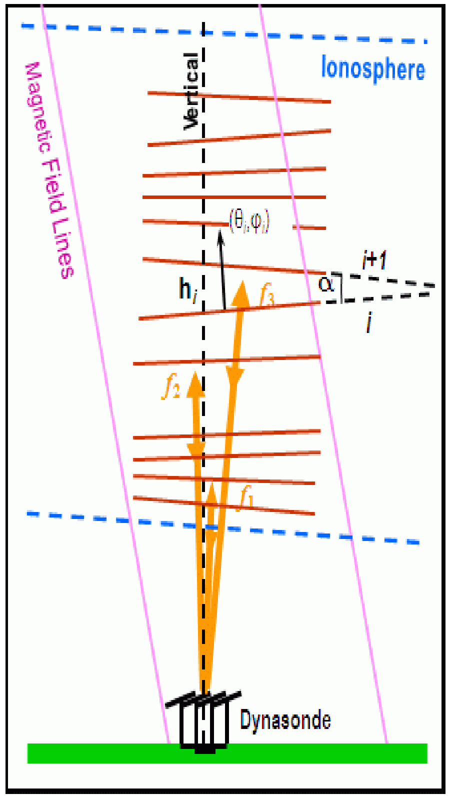

Figure 3.4. Schematic representation of the Wedge Stratified Ionosphere model. Courtesy of Nikolay Zabotin (personal communication).

Heights h_i and the components of the normal vector n_x, n_y are found by iterative ray tracing to match the observed ranges and angles of arrival of echoes reflected within the current wedge. The number of echoes attributed to individual wedges can vary, and this in turn influences the accuracy with which the parameters of a wedge are determined. Longer sounding sessions allow for more echoes to be obtained and produce more accurate results, but limit the temporal resolution of the final data products. The data used here were generally obtained with either a 1 or 2-minute resolution. NeXtYZ produces altitude profiles for several ionospheric parameters: the electron density with associated uncertainties, the zonal (west-east) and meridional (south-north) tilts and the vertical projection of the line-of-sight Doppler speed characterizing the motion of plasma contours. The original distribution of the profile points is non-uniform, with a typical spacing between adjacent points less than 1 km. For this work, all profiles were linearly interpolated to a uniform altitude grid with a 2 km resolution before further analysis. Figures 3.5 and 3.6 show sample NeXtYZ results obtained with the Tromso and Wallops Island Dynasondes. Figure 3.7 shows the results at Wallops Island, covering 24 hours.

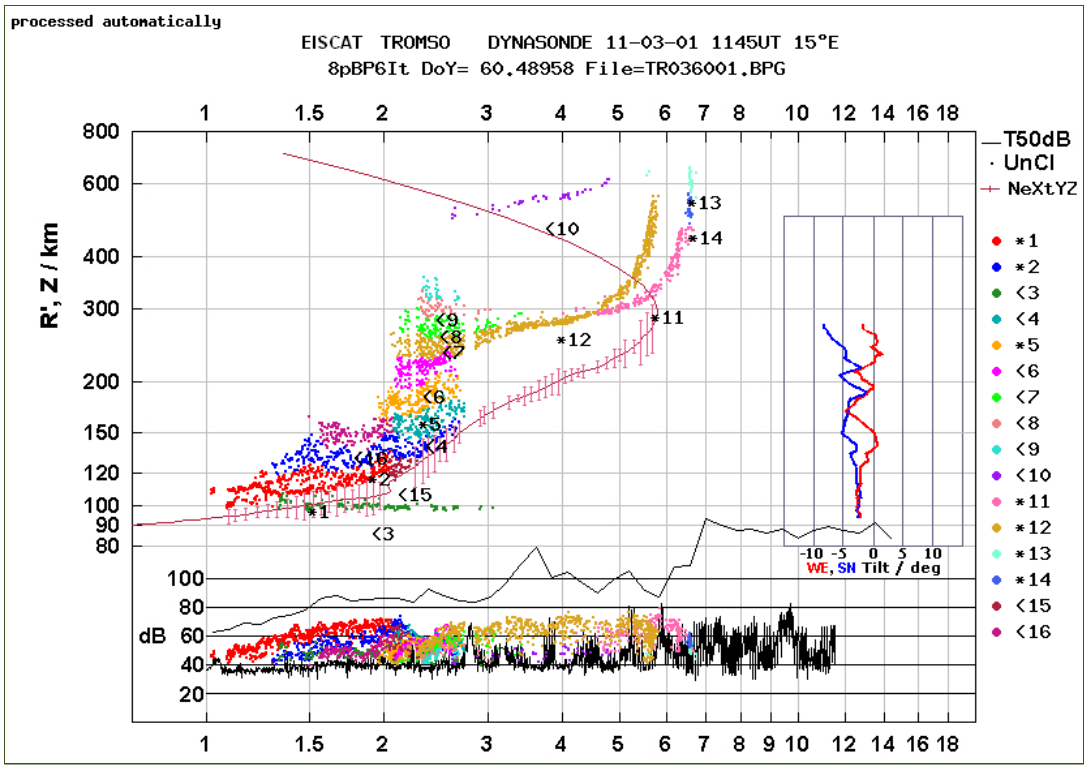

Figure 3.5. Sample results of the Dynasonde analysis software obtained using data from Tromso, Norway, on March 1, 2011, at 11:45 UT. Results from the Tromso Dynasonde can be obtained at http://dynserv.eiscat.uit.no/

In order to determine the full set of parameters characterizing AGWs and TIDs in the thermosphere-ionosphere, height-stratified measurements are required over a large altitude range, describing both the purely vertical electron density height profile and the local horizontal gradients. This allows for the determination of the full set of AGW parameters (vertical and horizontal wavelength, propagation direction, frequency, amplitude). In order to investigate the statistical distribution of these parameters and their long term variation, these measurements must cover time periods longer than several days. In the context of these requirements, a discussion is necessary on the advantages and drawbacks of the Dynasonde method, compared to the advantages and drawbacks of other methods.

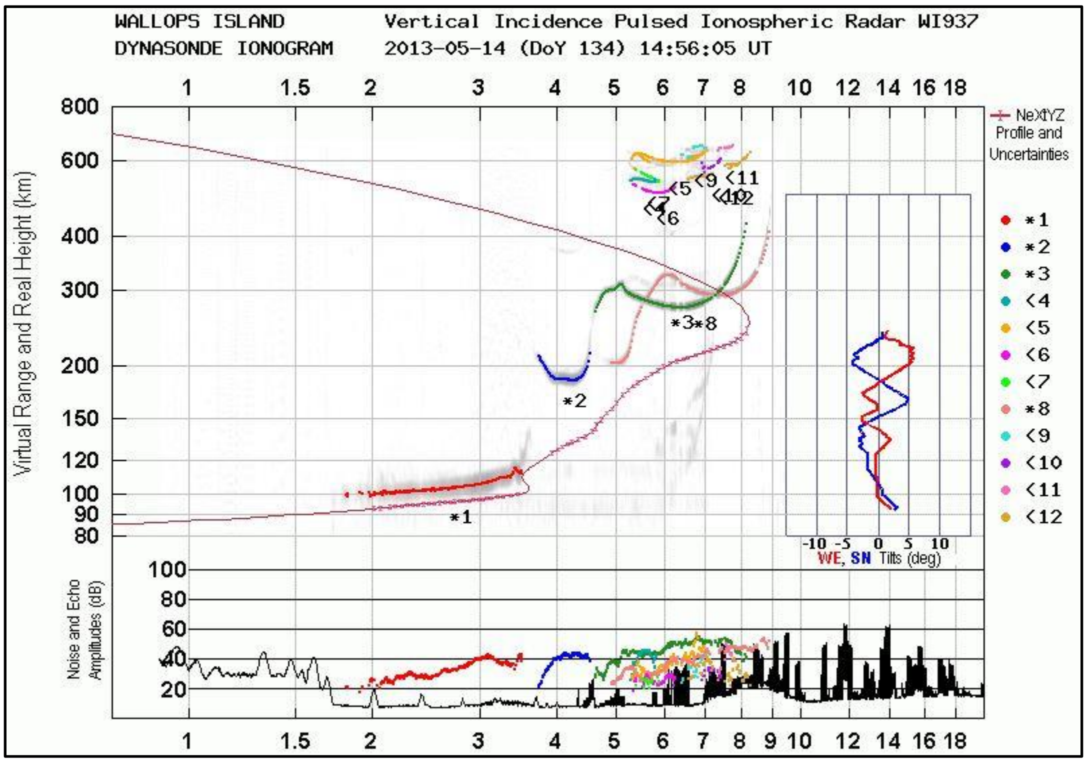

Figure 3.6. Sample results of the Dynasonde analysis software obtained using data from Wallops Island, VA, on May 14, 2013, at 14:56 UT. Results from the Wallops Island Dynasonde can be obtained at http://surf.colorado.edu/WI937.dcc

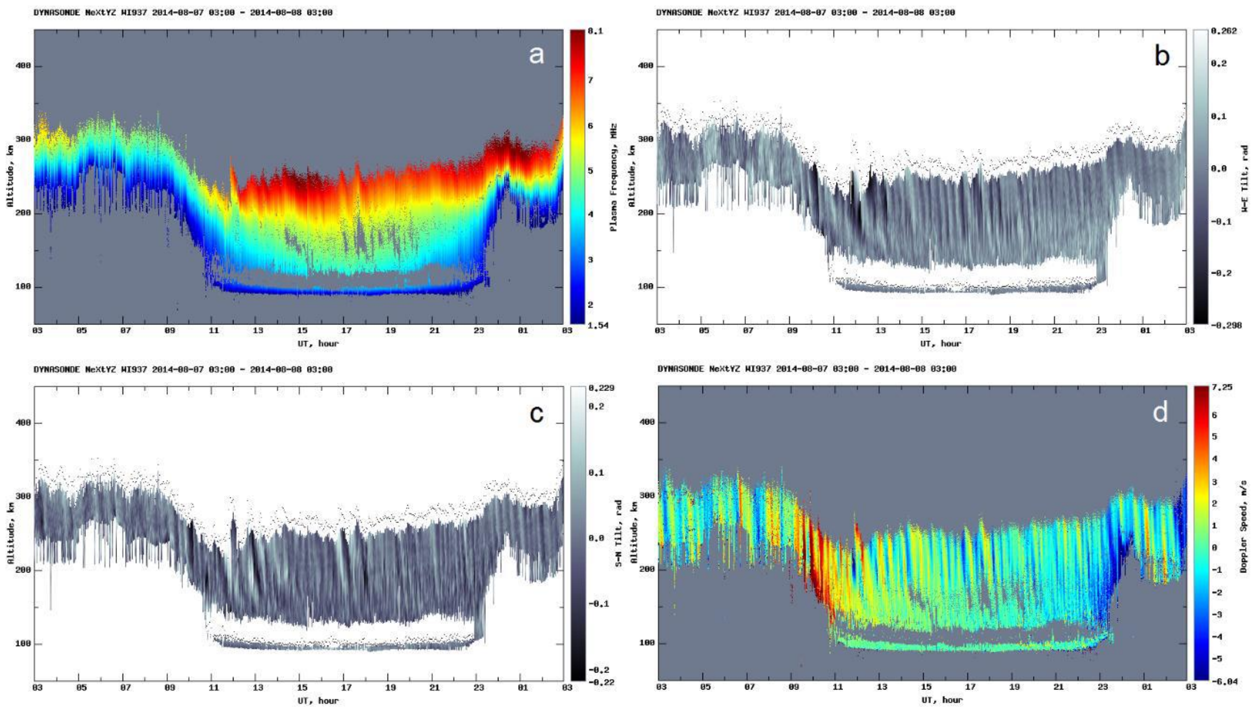

Figure 3.7. "One of the standard Dynasonde analysis products: a temporal scan of the vertical cross-section of several ionospheric parameters as a function of Universal Time and the true altitude over Wallops Island, VA" for August 7, 2014: (a) electron density, (b) zonal tilt, (c) meridional tilt and (d) Doppler speed. Evidence of TID activity is present in all four panels. Reproduced from Zabotin et al. (2016).

3.3. Advantages and Drawbacks of Ionospheric Remote-Sensing Methods.

One of the best-known datasets showing evidence of AGW activity are, probably, obtained with Incoherent Scatter Radar installations. *Djuth et al.* (2010) showed high quality ionospheric measurements taken at Arecibo, PR. Once detrended, the data exhibit clear downward phase propagation (Figure 1.1), typically indicative of upward propagating gravity waves. The relative perturbations reported by *Djuth et al.* (2010) were of 5-15% of the plasma density at any given altitude. These are significant levels that may have important implications since such gravity wave activity is quite common. Larger perturbations are possible, such as those reported by *Nicolls et al.* (2004), again using

ISR measurements at Arecibo (Figure 3.8). In both cases, purely vertical information was used. This allows the determination of temporal variability due to gravity waves. Through Fourier decomposition (or equivalent) techniques, spectral characteristics due to gravity waves can be determined. Obtaining spatial characteristics requires knowledge of the three-dimensional electron density distribution.

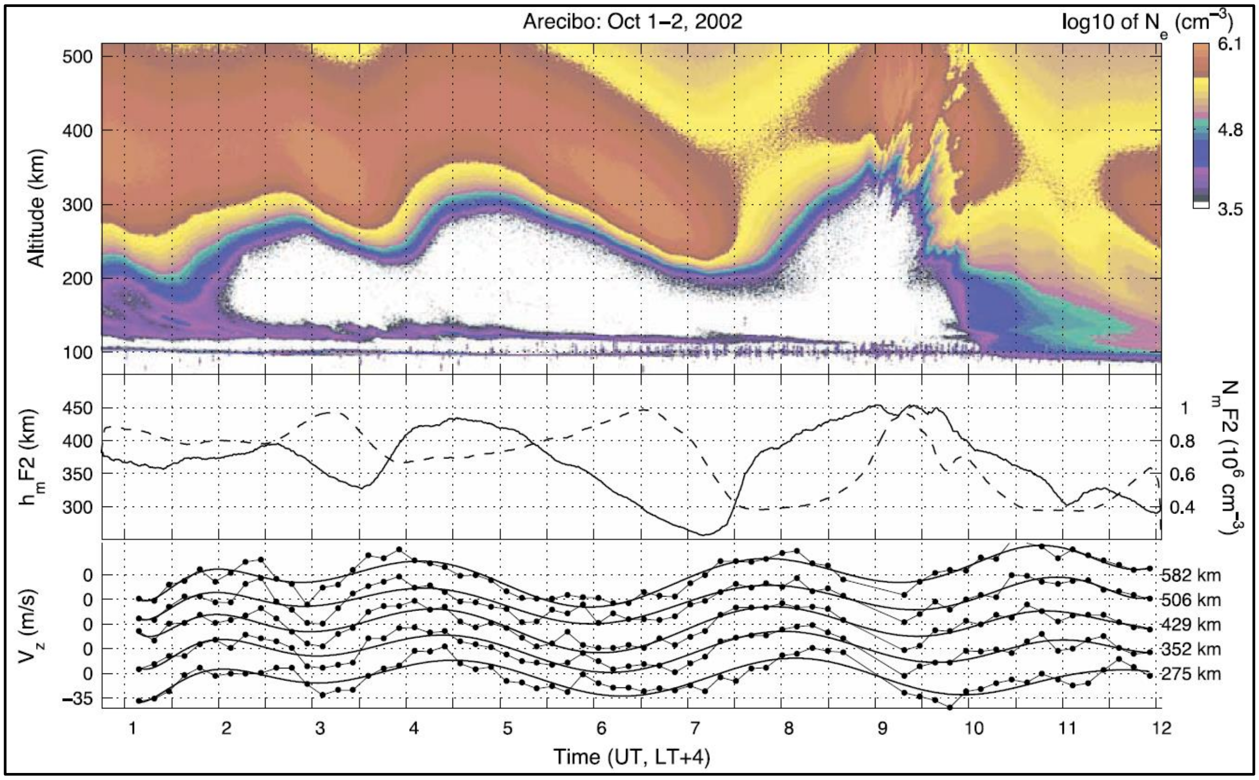

Figure 3.8. Large Scale TID detected with the Arecibo ISR during the "night of October 1-2 2002. The top panel is $\log_{10}$ of electron density, the middle panel is h_mF_2 (solid) and N_mF_2 (dashed), smoothed over 12 minutes, and the bottom panel is vertical ion velocity (points) with polynomial fits (solid). The tick marks in the V_z panel are separated by 35 m/s." Reproduced from Nicolls et al. (2004).

It is possible to collect off-vertical information from an ISR with scanning capabilities. The typical approach is to employ several scanning beams at varying angles. This can reduce the frequency at which data is collected, depending on the specific instrument mode used. For example, *Ma et al.* (1997) used the EISCAT ISR to obtain information on the local three-dimensional electron density distribution, but only with a 6 minute cadence. Another example is the Poker Flats ISR (e.g., *Nicolls and Heinselmann 2007, Figure 3.9*). In these cases "propagation characteristics" (*Ma et al.,* 1997) of gravity waves can be determined. With knowledge of both spectral and spatial characteristics (frequency, wavevector, amplitude), all other desired information can be potentially determined. This can be done over a large altitude interval with good accuracy. The main drawback of ISRs is the limited data availability, with datasets covering at most several days.

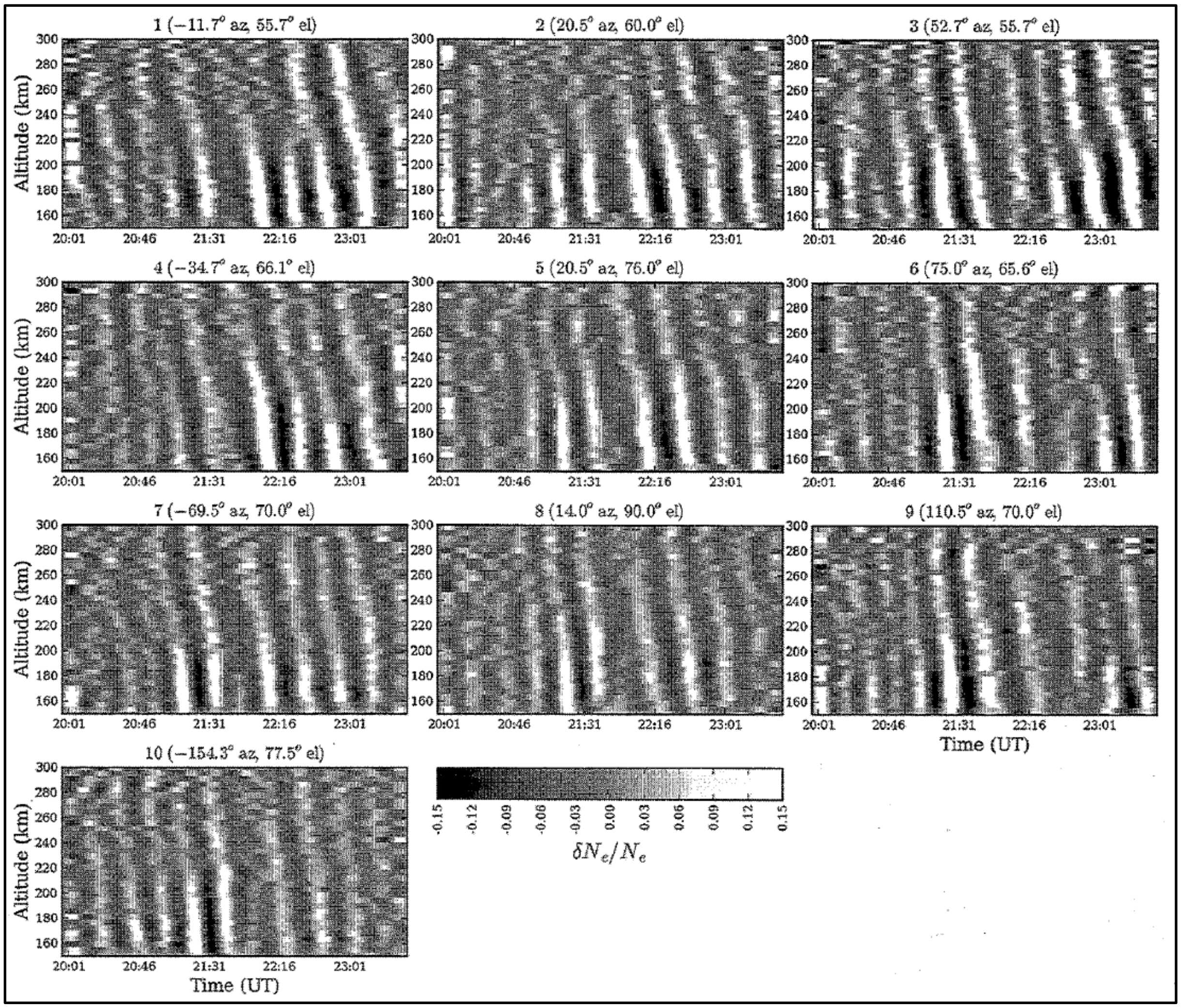

Figure 3.9. Relative electron densities reported by Nicolls and Heinselmann (2007). The 10 panels represent results with different scanning beams. Reproduced from Nicolls and Heinselmann (2007).

Other remote sensing techniques have been used for the study of gravity waves in the thermosphere-ionosphere. GPS derived Total Electron Content (TEC) can exhibit disturbances due to gravity wave activity (Figure 3.10). *Afraimovich et al.* (1998, 1999) determined characteristics of Large Scale Travelling Ionospheric Disturbances (LSTIDs) induced by associated large scale gravity waves. While the use of GPS data potentially allows for wide geographical (potentially global) coverage (*Otsuka et al.,* 2013, *Saito et* *al.,* 1998), the method has significant limitations. Due to the integral nature of TEC measurements, any detected perturbations cannot be traced to an exact location (latitude, longitude, altitude). Large scale, large amplitude waves can be detected, but difficulties arise in detecting multiple simultaneous wave modes. Thus, the method is appropriate in determining global characteristics of large scale gravity wave activity in the *F*-layer, but these results may not be entirely representative of the whole gravity wave spectra. In addition, any height variability cannot be determined.

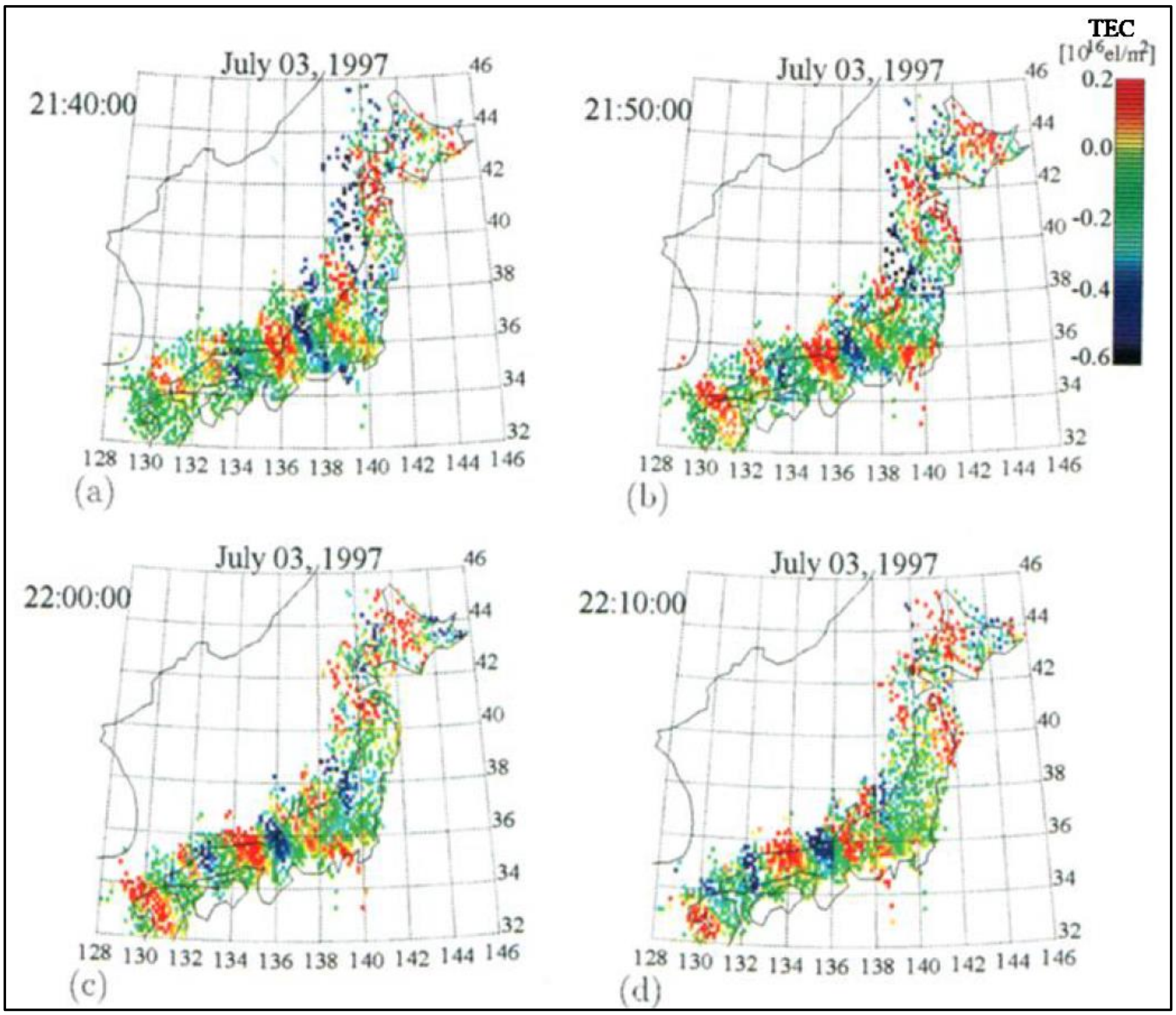

Figure 3.10. LSTIDs detected in the GPS TEC by Saito et al. (1998).

Characteristics of large amplitude waves can also be determined starting from Super Dual Auroral Radar (SuperDARN) Network data (*Bristow et al.* 1994; *Ishida et al.,* 2008). The method has significant potential since the network currently includes 35 instruments in both the Northern Hemisphere and Southern Hemisphere. Published results show Large- and Mid-scale TIDs observed as a function of range, and not exact coordinates. Figure 3.11 is an example of a dataset obtained with the Goose Bay SuperDARN on 6 December 1991. This introduces a limitation on the precision with which gravity wave activity can be localized. Additional limitations may be introduced due to a bias towards detecting waves with certain propagation directions (*Frisell et al.*, 2014).

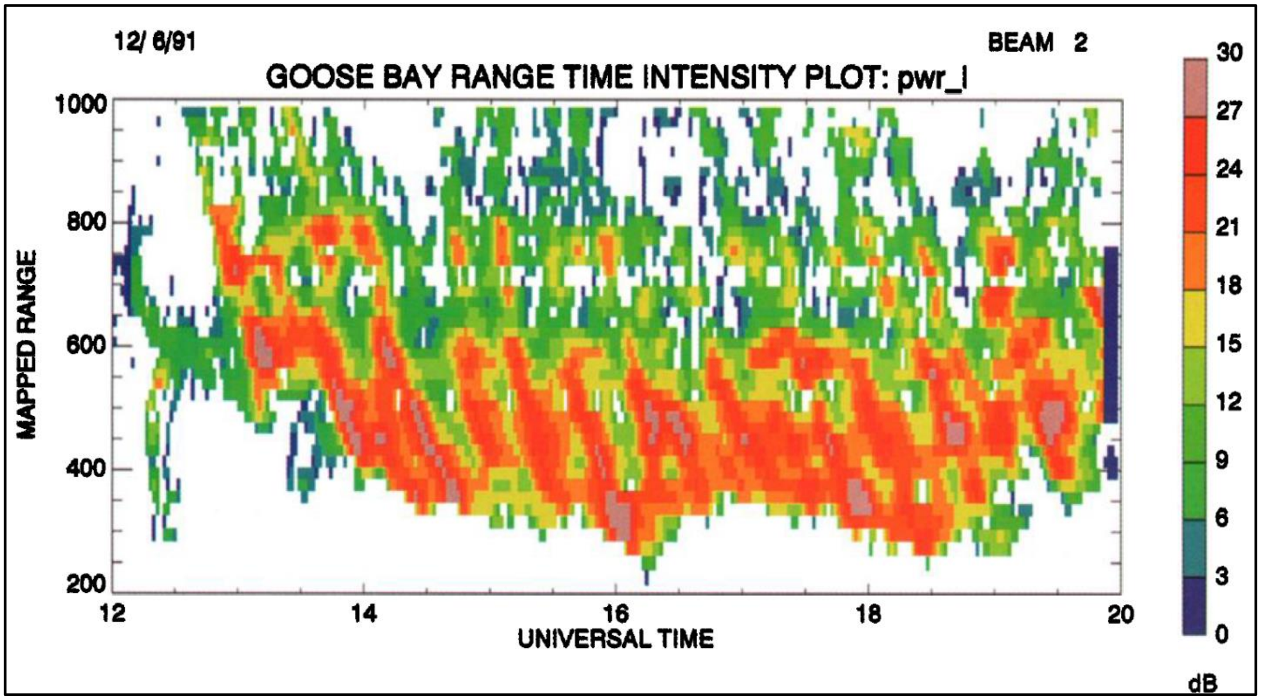

Figure 3.11. LSTIDs detected with the Goose Bay SuperDARN between 12:00 to 20:00 UT on 6 December 1991. "The power enhancements are due to local density minima causing a focusing of the reflected power." Reproduced from Bristow et al. (1994).

Airglow all-sky imagers use the OI (630 nm) emission to detect TIDs (*Shiokawa et al,* 2003, Figure 3.12). The result is an integral one, as with GPS TEC, representative for the bottom-side *F*-Layer (200-300 km). The technique is ground based, providing results within a field-of-view with a typical 500 km radius. This allows for a significant area to be covered and for the horizontal wavevector components of the detected waves to be determined, along with the direction of propagation. However, two drawbacks exist: measurements can only be obtained at night and they cannot provide any altitude dependence.

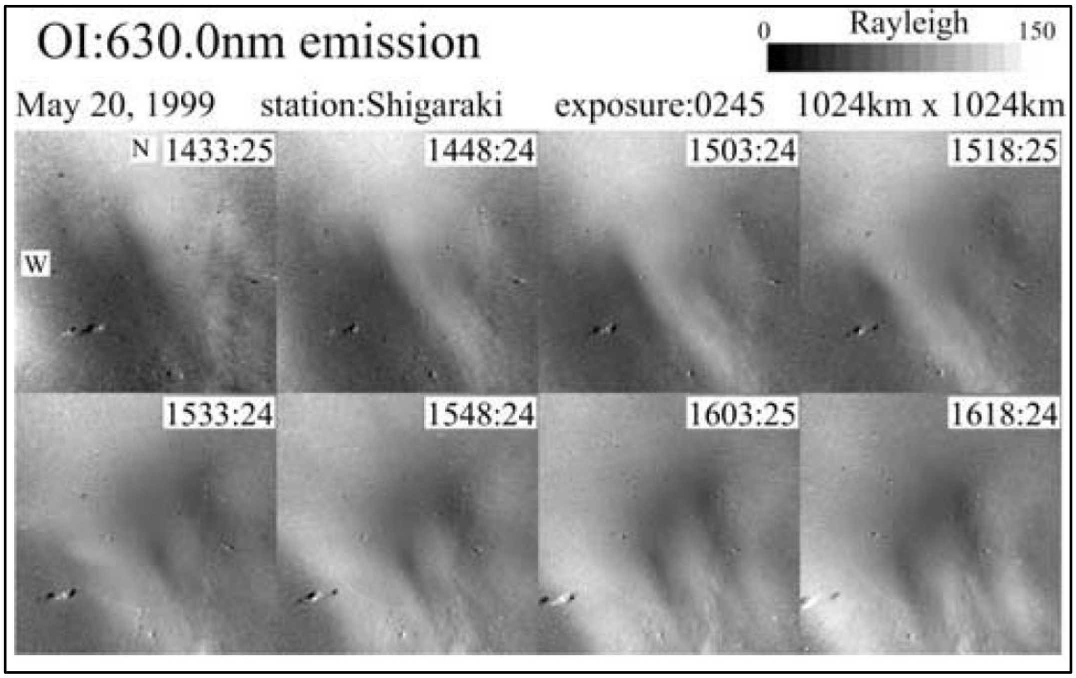

Figure 3.12. MSTIDs detected using all-sky imagers between 14:33 and 16:18 UT on 20 May 1999 at Shigaraki, Japan. Reproduced from Shiokawa et al. (2003).

Finally, the HF Doppler technique has been used in the past (*Crowley et al.*, 1987; *Georges*, 1968), and more recently by the so-called "Travelling Ionospheric Disturbance Detector Built in Texas" (TIDDBIT). The technique requires at least one continuous wave (CW) radio transmitter and receiver (for the study of TIDs, multiple transmitters are necessary) in the HF band, typically between 3 and 10 MHz (Figure 3.13). The signal will be reflected by the ionospheric plasma at an altitude depending on the frequency used.

If the respective ionospheric layer is moving, the reflected signal will be Doppler shifted by an amount directly proportional to the speed of the layer:

$$\Delta f = 2\frac{v}{c}f_0 \tag{3.11}$$

where Δf is the Doppler shift, f_0 is the frequency of the CW signal, and v is the line-of-sight speed of the plasma at the reflection point. The use of more than one frequency is possible, allowing for results corresponding to several altitudes to be obtained. The main advantages of this method are the possibility of continuous operations, with some datasets covering several years. However, the altitude associated with such Doppler measurements is not known with precision, and the variation of the TID activity with height is largely unknown.

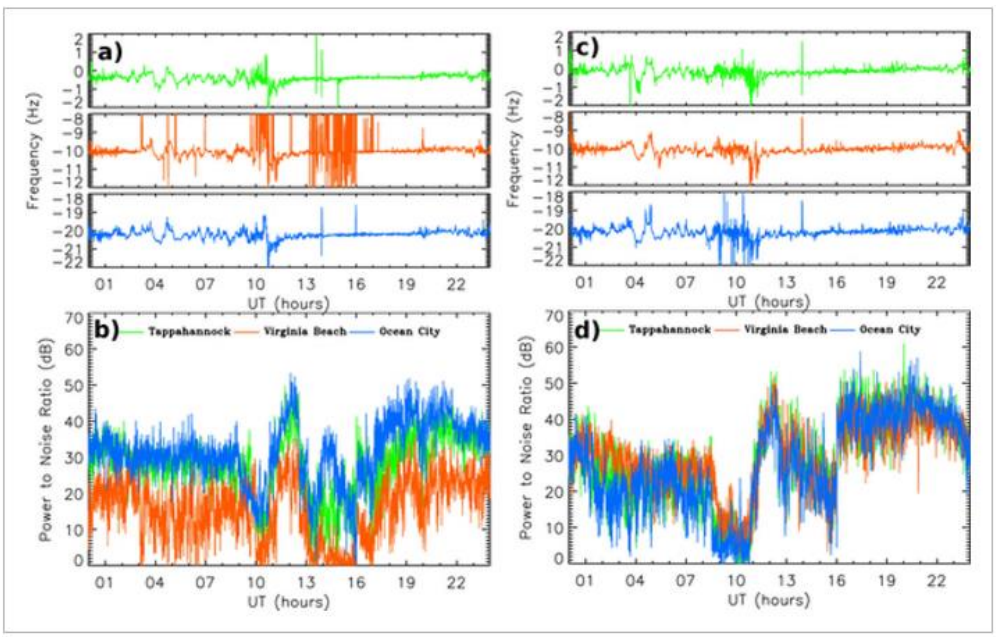

Figure 3.13. HF Doppler radar data obtained using the TIDDBIT instrument in the Chesapeake Bay are on 15 October 2006. "(a and c) Doppler shifts and (b and d) received power for 3.160 MHz X mode (a and b) and 3.517 MHz X mode (c and d)." Reproduced from Crowley and Rodrigues (2012).

Of the methods described above, the Dynasonde technique provides results most similar to those obtained using Incoherent Scatter Radars. *Sedgemore et al.* (1996) showed that Dynasonde and ISR data are either in very good agreement or complementary to each other (Figure 3.14). When collocated ISR and Dynasonde instruments perform simultaneous analysis of thermospheric AGWs, the results obtained with the two instruments are therefore expected to be in agreement. For example, *Zabotin et al.* (2016) show a dependence with altitude of the spectrum of the Arecibo ion and plasma line, which has many of the same properties as the spectrum of the San Juan Dynasonde Doppler speed data (Figure 3.15). ISR raw results are relative electron density profiles, while Dynasonde measurements can be inverted to obtain the true height profile of electron density. Results obtained with both methods for the bottom-side ionosphere are of similar quality. Dynasondes (like all ionosondes) cannot perform any measurements of the plasma density in the *E-F* “valley”. Also, ground based Dynasondes cannot obtain information on the topside ionosphere. However, due to competing research interests and technical limitations, existing ISRs typically do not provide continuous data sets of the size now provided by Dynasondes.

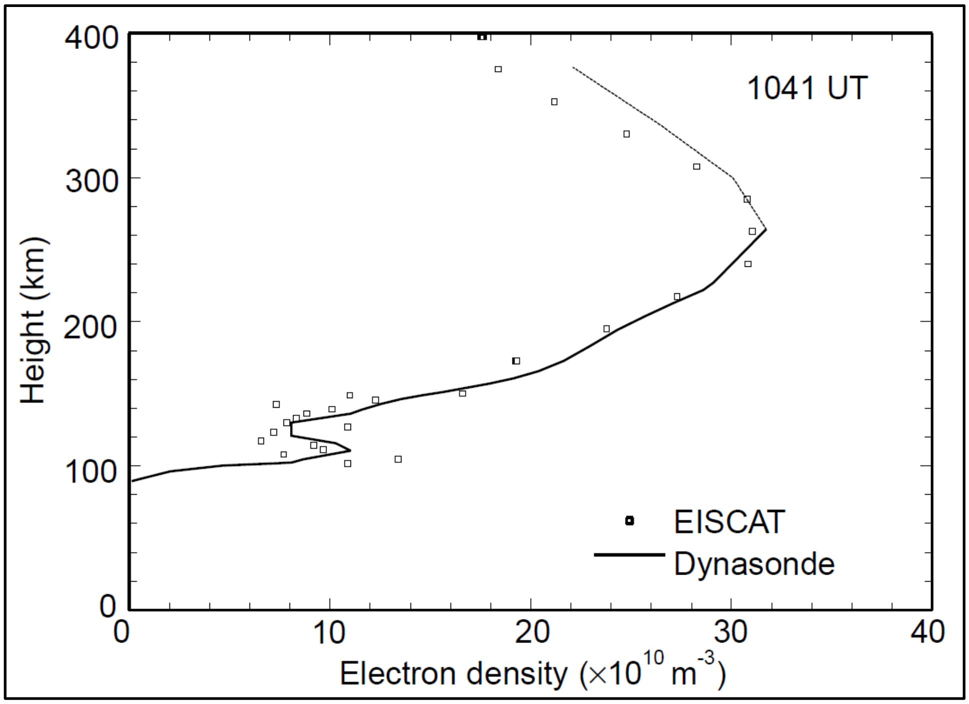

Figure 3.14. Comparison between electron density height profiles obtained by the collocated EISCAT ISR and Tromso Dynasonde at 10:41 on 20 May 1994. Reproduced from Sedgemore et al. (1996).

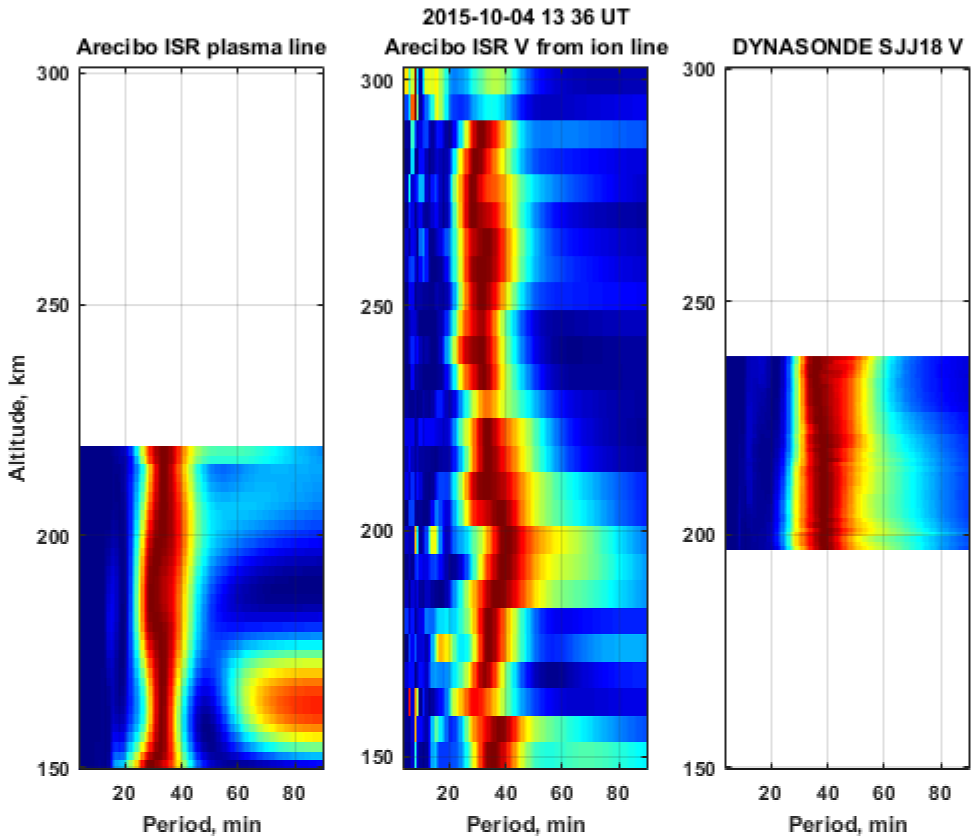

Figure 3.15. Dependence with altitude of the Arecibo plasma line (left panel) and ion line (middle panel) spectrum, and of the collocated San Juan Dynasonde Doppler speed spectrum (right panel). Reproduced from Zabotin et al. (2016).

CHAPTER 4

SPECTRAL ANALYSIS AND SEASONAL VARIABILITY

4.1. Introduction

The datasets provided by Dynasonde instruments cover time periods of several years. This allows for the study of atmospheric waves, their altitude variation and seasonal variability. This is achieved primarily by use of the Dynasonde measured tilt data, and also the electron density and Doppler speed. A fluid wave propagating through the thermosphere can generally be described by a plane wave model (*Fritts and Alexander,* 2003). The expanding and contracting neutral gas will induce wave-like variations in the local electron density (*Nicolls et al.,* 2013):

$$N_e(t) = N_{e0}\ e^{i(\boldsymbol{k}\cdot\boldsymbol{r}-\omega t)} \tag{4.1}$$

Equation (4.1) describes electron density variations referred to as TIDs, and while these are not waves, they are indicative of the underlying AGWs that induced them. If such a wave-like variation is produced in the ionospheric plasma, then a wave-like variation must necessarily be produced in the ionospheric tilts, and its exact for can be obtained using Equations (4.1) and (3.10):

$$n_{x,y} = \frac{k_{x,y}}{|\boldsymbol{\nabla} N_e|} N_{e0}\ e^{i(\boldsymbol{k}\cdot\boldsymbol{r}-\omega t)} \tag{4.2}$$

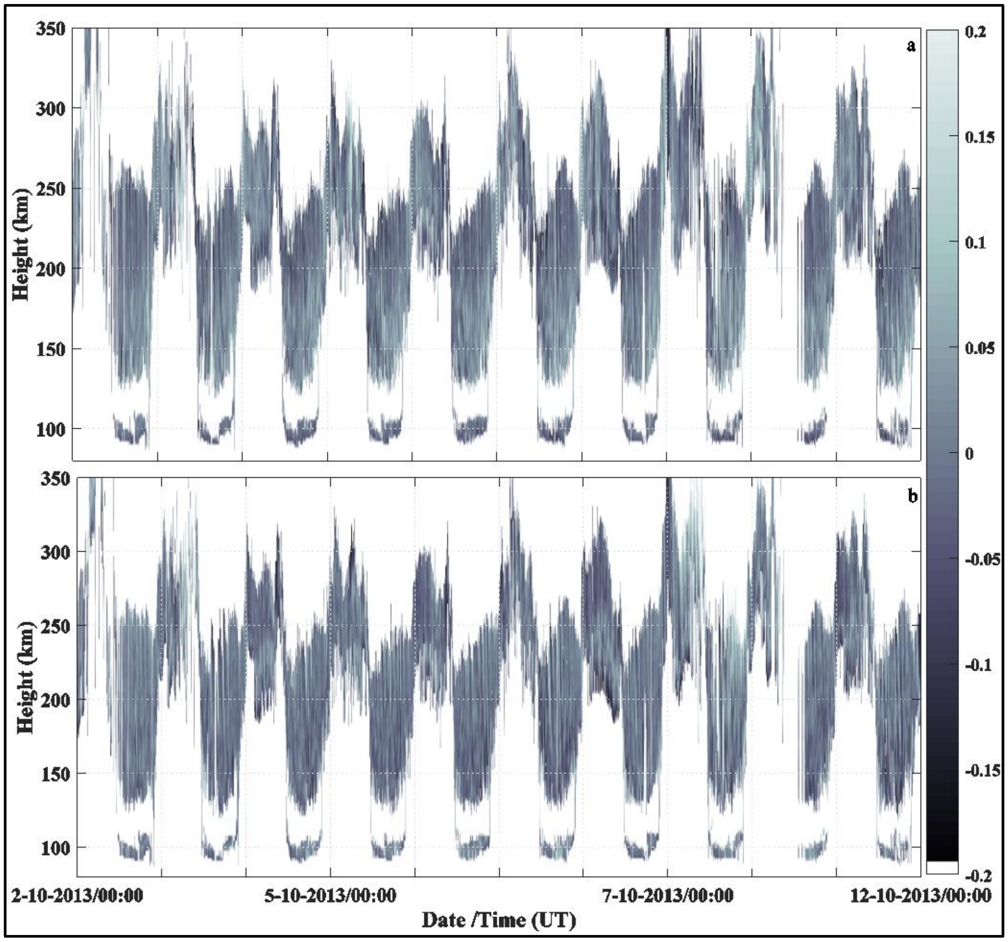

Figure 4.1. Temporal and altitude variability of the zonal (west-east) (a) and meridional (south-north) (b) tilt data. The dataset was obtained at Wallops Island, VA, and it covers the time interval from 2 October to 11 October 2013. Reproduced from Negrea and Zabotin, (2016).

where N_{e0} is the amplitude of the wave with ground based angular frequency $\omega = \omega_0 + \boldsymbol{u} \cdot \boldsymbol{k}$, ω_0 is the intrinsic wave frequency, $\boldsymbol{k} = (k_x, k_y, k_z)$ is the wavevector, $\boldsymbol{u}$ the neutral wind vector, $\boldsymbol{r}$ is the position vector, and t is the time. Also, the two tilt components provide differentiation between waves propagating in different directions through the $k_{x,y}$ term in equation (4.2). While the tilt measurements are currently unique to the Dynasonde technique, they are unambiguously related to the horizontal components of the electron density gradient, which has been previously used to determine the parameters associated with gravity wave induced TIDs (*Oliver et al.*, 1994; *Oliver et al.*, 1995).

Figure 4.1 shows the entire tilt data obtained at Wallops Island within the 10-day interval (2 – 11 October 2013). Note the variability of the altitude coverage of the data, with the day-to-night and the night-to-day transitions as a prominent feature. A more detailed image is necessary to highlight the individual wave signatures in the data. Figure 4.2 shows the zonal and meridional tilt data covering only 24 hours during 5 October 2013. Here the slightly inclined wave fronts (indicating downward phase propagation) characteristic of AGWs are clearly visible throughout most of the interval, with the dominant waves characterized by periods ranging from several minutes to a few hours.

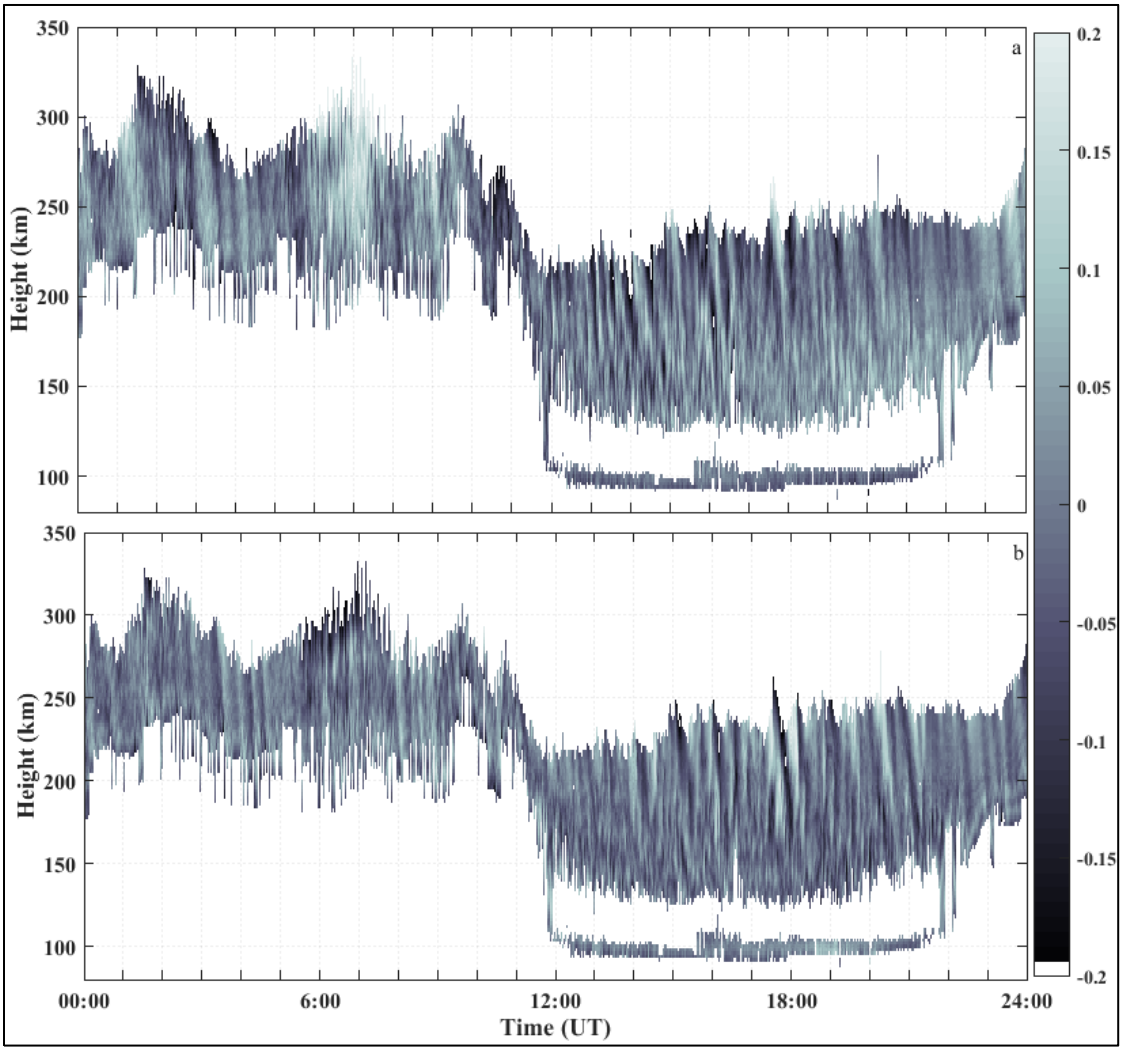

Figure 4.2. Same as Figure 4.1, but covering only 24 hours on 5 October 2013. The slightly inclined strips are indicative of the phase fronts created by upward propagating AGWs. Reproduced from Negrea and Zabotin (2016).

For datasets characterized by uniform sampling, it is possible to fully determine the power spectrum due to wave activity, as well as the time domain induced perturbation at any arbitrary time instance (*Shannon*, 1948; *Butzer and Stens*, 1992). In addition to the requirement for uniform sampling, another necessary condition is that the wave activity be limited to periods higher than twice the sampling rate (in this case, 2 min). This is a reasonable assumption as the peak in thermospheric AGW activity is generally associated with periods between a few hours to tens of minutes. However, both Figure 4.1 and Figure 4.2 show that, at any given altitude, there is a non-uniformly sampled time series when considering periods of several days. For some data processing applications, a technique referred to as downsampling can be applied, removing select data points in order to obtain a uniformly sampled dataset (e.g., *Eng and Gustafsson*, 2007). However, this is not an appropriate solution for this work due to the presence of periodic data gaps of approximately 12 hours.

The basic fast Fourier transform (FFT) cannot be used to accurately determine the power spectral density (PSD) in the case of non-uniformly sampled data. This is a well-known and general problem for the field of spectral analysis. Several solutions have been proposed in the existing literature, such as a more general implementation of the FFT, the non-uniform FFT (NUFFT). The technique attempts to compensate for the effects of data gaps while retaining the high computational efficiency of the FFT (e.g., *Nguyen and Liu*, 1999; *Fessler and Sutton*, 2003).

Another proposed approach determines the power spectrum through least-squared (LS) fitting. The number of operations required for such an approach makes it considerably slower than a NUFFT (*Press and Rybicki*, 1988). While this may be a somewhat important aspect when analyzing very large datasets, the rapid increase in processing power of modern computer systems makes LS methods feasible for the purposes of this study. A variation of LS fitting is the so-called Lomb-Scargle method, which yields the power spectrum $P(f)$ associated with a given time series as

$$P(f) = \frac{1}{N}\left[\frac{(\sum_i (x_i - \bar{x}) \cos \omega(t_i - \tau))^2}{\sum_i \cos^2 \omega(t_i - \tau)} + \frac{(\sum_i (x_i - \bar{x}) \sin \omega(t_i - \tau))^2}{\sum_i \sin^2 \omega(t_i - \tau)}\right] \tag{4.3}$$

with the parameters: $\bar{x} = \frac{1}{N}\sum_i x_i$, $\tan(2\omega\tau) = \frac{\sum_i \sin 2\omega t_i}{\sum_i \cos 2\omega t_i}$, $\omega = 2\pi f$ is the angular frequency and *N* is the size of the dataset (t_i, x_i). The method is widely used for spectral analysis of non-uniformly sampled data in a variety of scientific fields [*Horne and Baliunas*, 1986; *Schimmel*, 2001; *Thong et al.*, 2004; *Zhou et al., 1997*]. While it is debatable whether Lomb-Scargle offers a clear computational advantage to a more basic LS approach (*Stoica et al.,* 2009), the results obtained using either variant are equivalent. For the remainder of this work, Lomb-Scargle will form the basis of the spectral analysis techniques used.

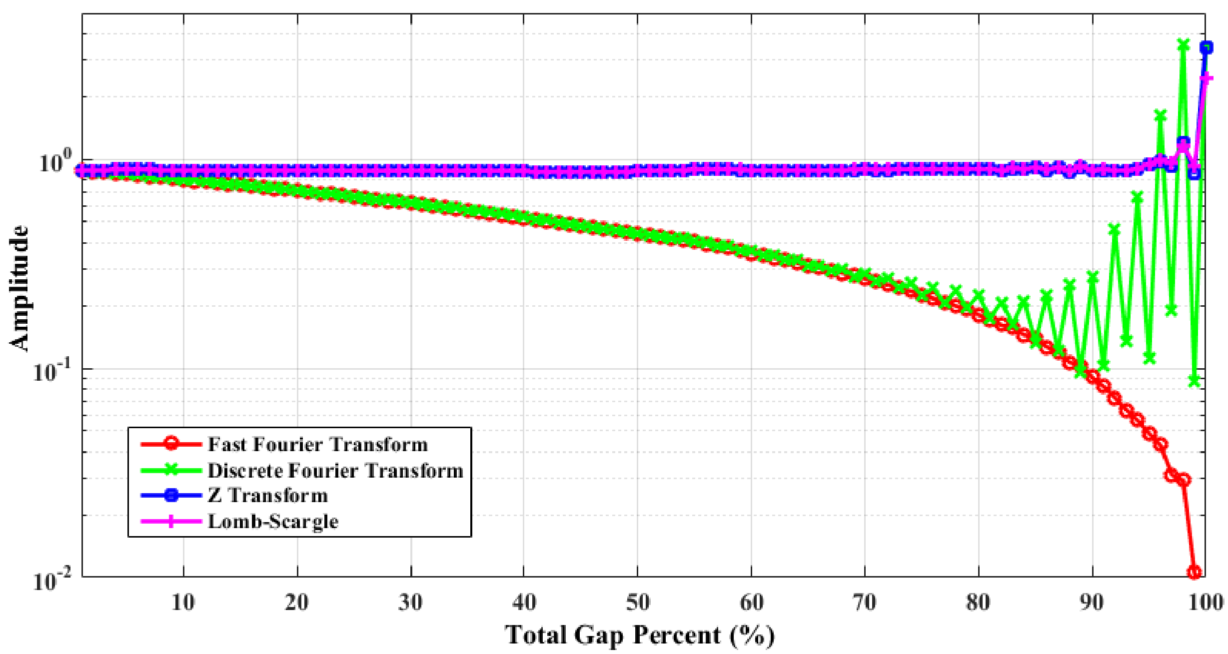

Figure 4.3. The spectral amplitude obtained using several spectral analysis methods in the presence of data gaps of varying size, in the case of a high amplitude, dominant spectral feature (such as those due to atmospheric tides). Notice the nearly constant results obtained using Lomb-Scargle, except for very large data gaps. Adapted from Munteanu et al. (2016).

Results of spectral calculations performed with a large time series can be subject to significant variations. Additional complications may be caused by inevitable noise in the data. Assuming this noise has a zero mean, the approach described by *Welch* [1967] can be used to mitigate the problem. The Welch method is used to determine the mean PSD by dividing the data into overlapping subintervals, calculating the PSD for each subinterval, and finally averaging results for all subintervals. This approach is typically used with a FFT implementation, but using the technique in conjunction with the Lomb-Scargle method is perfectly valid.

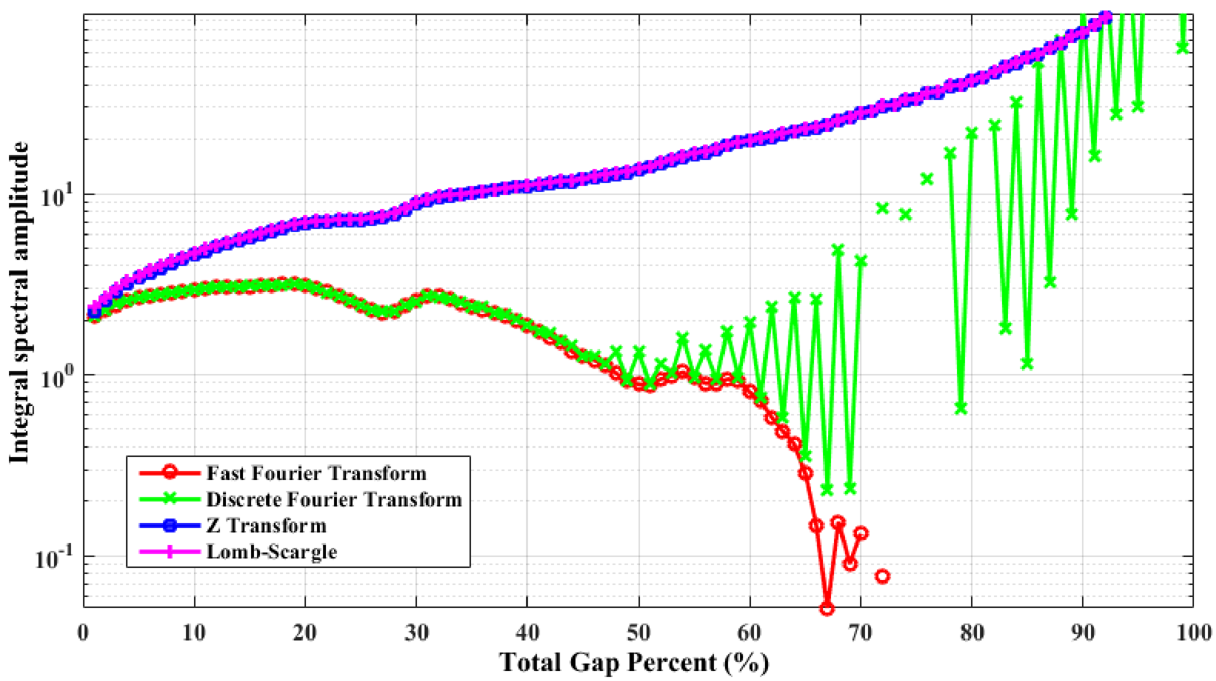

Figure 4.4. The integral spectral amplitude obtained using several spectral analysis methods in the presence of data gaps of varying size, in the case of a smooth, slowly varying spectrum with no dominant features (such as those due to AGWs). Notice the rapidly increasing errors associated with all methods. Adapted from Munteanu et al. (2016).

As shown by *Munteanu et al.* (2016), existing spectral analysis techniques suffer from higher errors and biases in the presence of extensive data gaps. While the specifics of these biases, such as their dependence on frequency and data gap size, can vary significantly depending on the technique used, currently, no known spectral analysis method can produce arbitrarily accurate results for data that is non-uniformly sampled. The spectral analysis techniques used for this work are based on the Lomb-Scargle method. The technique was originally used for the study of high-amplitude spectral features. As shown by *Munteanu et al*. (2016), the caveats of the method can be negligible if the spectral features of interest are very high amplitude and narrow bandwidth, such as those caused by atmospheric tides (Figure 4.3). As such, the method can be readily used for the study of tidal harmonics, and the height profile of the first three harmonics is discussed in Section 4.4. For the frequency range affected by thermospheric AGWs, the mean amplitudes over longer time intervals are generally smaller than those of tidal modes. In contrast, the associated bandwidth is much larger and the overall shape of the spectrum smoother. Tests performed by *Munteanu et al.* (2016) using data characterized by a similarly “smooth” spectrum have shown that if data gaps totaling more than 10–20% of the entire time series are introduced, the resulting error in the final result is significant (Figure 4.4) and frequency dependent (the error is larger at higher frequencies), leading to a spectrum that is deformed when compared to the expected result.

4.2. Determining the Mean Power Spectral Density.

In the case of the AGW spectrum, applying a filtering criterion of statistical significance would exclude most of the wave activity characterized by smaller amplitudes.

An alternative approach for calculating the mean Power Spectral Density (PSD) is presented, using an integral criterion to establish the validity of a whole PSD as opposed to individual harmonics. For a dataset characterized by a stationary spectrum and with minimal or no noise, the PSD must follow the identity

$$\sum_1^{N_f} P_i \cdot (t_N - t_1) \cdot \Delta f_i = \sigma^2 \tag{4.5}$$

which is consequence of Parseval's theorem and where P_i is the power calculated for frequency bin Δf_i using Equation (4.3), N_f is the total number of frequency bins, $t_N - t_1$ is the length of the time interval considered and σ^2 the variance in the time domain.

In the case of real data, Equation (4.5) is satisfied only approximately:

$$\sum_1^{N_f} P_i \cdot (t_N - t_1) \cdot \Delta f_i + \xi = \sigma^2 \tag{4.6}$$

where the extra term ξ sums up the effect due to noise, non-stationarity and, in the case of non-uniform sampling, data gaps. For the purposes of this work, ξ can be interpreted as an error. To determine an upper boundary for ξ, a test has been devised using synthetic data.

One hundred synthetic time series have been generated using an amplitude spectrum $A(f)$ that follows a Gamma distribution:

$$A(f) = \sqrt{\frac{2}{N} P(f)} = A_0 \cdot F(f, \alpha, \beta) + B_0 \tag{4.7}$$

where $F(f, \alpha, \beta) = \frac{1}{\left(\int_0^\infty x^{\alpha-1} e^{-\alpha} d\alpha\right) \beta^\alpha} f^{\alpha-1} e^{-\frac{f}{\beta}}$ is the standard Gamma Probability Density Function, α is the shape parameter, varying from 1.05 to 4.8, and β is the scale parameter, varying from $3 \cdot 10^{-4}$ to $6.5 \cdot 10^{-4}$. A further scaling factor A_0 of $1.1 \cdot 10^{-5}$ and a uniform background level B_0 of $3.5 \cdot 10^{-3}$ are applied. The time series equivalent to this spectrum is determined and, finally, the resulting ”dataset” is “polluted” using Gaussian distributed noise with mean zero and $2 \cdot 10^{-2}$ variance. The resulting datasets each contain 7200 points and are intended to mimic the expected thermospheric AGW spectrum, with the added noise component also introducing a degree of non-stationarity. Figure 4.5 shows the full set of PSDs characterizing the synthetic datasets. The choice in the values of the parameters in Equation (4.7) was made such that the resulting $A(f)$ would reproduce the main spectral features in ionospheric tilts.

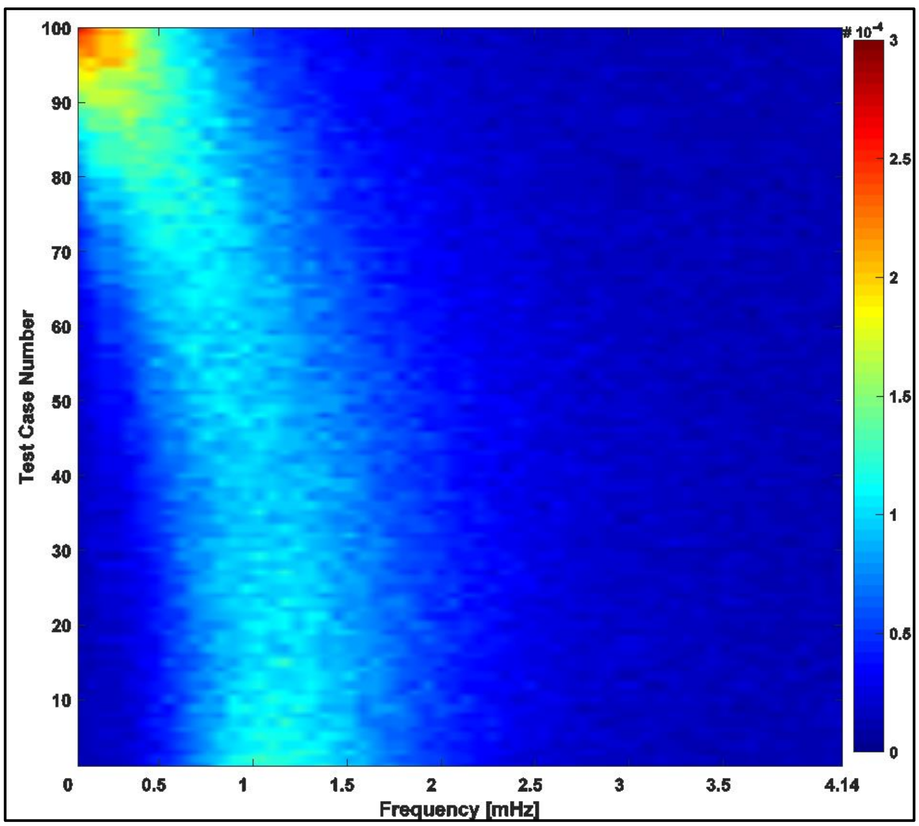

Figure 4.5. Power spectra characterizing the synthetic datasets. The dominant structure is similar to that produced due to the height variation of the AGW spectrum. The fine granular structure is due to the added noise term in Equation 4.7. Reproduced from Negrea and Zabotin, (2016).

The time series generated for each test case is separated into subintervals 120 points long, with a 10-point overlap. For each subinterval, both the time domain variance and the PSD integral are calculated and the relative error $\Delta\xi = \left(\sum_1^{N_f} P_i \cdot (t_N - t_1) \cdot \Delta f_i - \sigma^2\right)/\sigma^2$ is determined. Figure 4.6 shows the maximum value for $\Delta\xi$ obtained in any of the 65 subintervals in each test case. The values tend to locate between 2 and 4%, with a number of 4 outliers in Figure 4.6 with values higher than 4%. For the purpose of our calculations with Dynasonde tilt data, based on the results shown in Figure 4.6, a maximum acceptable value of $\xi_0 = .04 \cdot \sigma^2$ for ξ will be used to determine the validity of individual subintervals. Assuming a Gaussian distribution to the values of $\Delta\xi$, the chosen 4% value encompasses 96% of the obtained values, or approximately double the standard deviation.

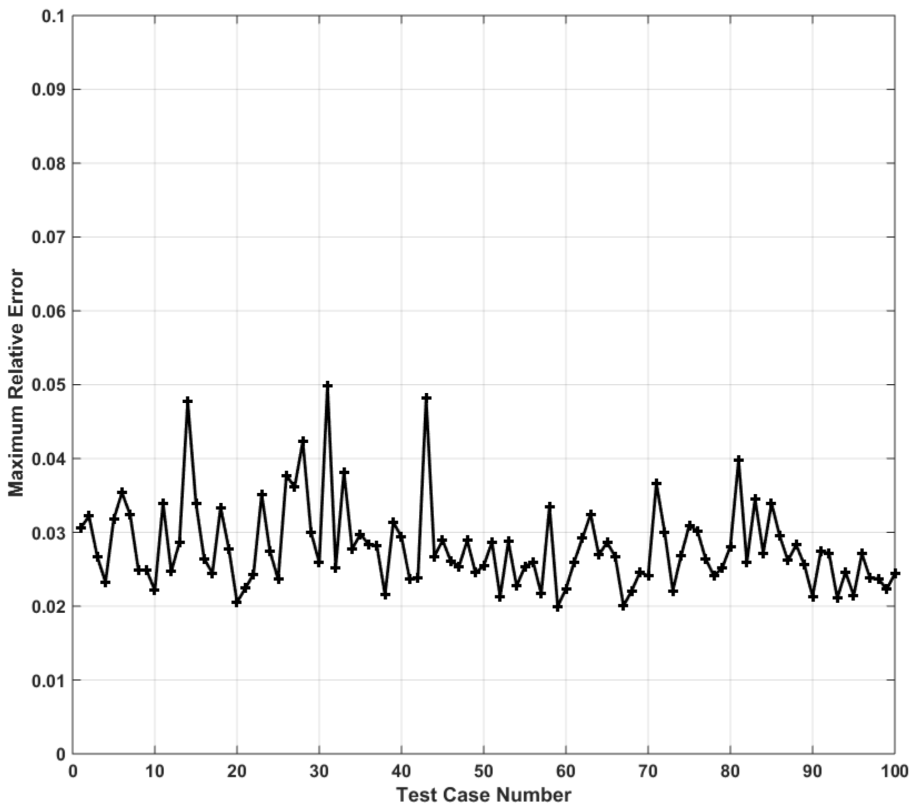

Figure 4.6. Maximum percent error obtained for each test case using a subinterval size of 120 points. The majority of the values are between 0.02 and 0.04, with 4 outliers closer to 0.05. Based on this result, a value of ξ_0=.04·σ^2 is chosen as the maximum accepted error. Reproduced from Negrea and Zabotin, (2016).

Because of the very different sampling throughout the altitude range of interest, it is essential that results at different heights be equivalent in their physical meaning. This is accomplished by using the method described here with an added oversampling factor of 10 (*Press et al.*, 1992), in conjunction with the threshold of 4% on $\Delta\xi$. To highlight the importance of filtering and of the derived criterion, the tilt power spectrum is calculated for the selected 10-day dataset in October 2013 using three methods. First this is achieved using our proposed approach, second this is done with a filtering criteria based solely on the size of the data gaps, and third, with no filtering at all. In all three cases, the subinterval length was 4 hours with an overlap of 20 min between adjacent subintervals.

Figure 4.7 shows the zonal tilt power spectra corresponding to the data shown in Figure 4.6. No filtering criteria were imposed, and as such, the averaging was performed using results for all subintervals that contained a minimum of 10 data points. The resulting average spectra contain several questionable features, such as the sudden changes in the background level around 210, 240, and 260 km. Below 150 km, the decrease in the number of subintervals causes an increase in the noise level, making interpretation difficult. Using this result, one could erroneously arrive at the conclusion that the waves propagating from lower altitudes are steadily attenuated as they reach higher altitudes, but have a higher level of wave activity between 210 and 240 km and above 260 km. This would imply some wave sources that are not directly linked to typical forcings in the lower atmosphere, a situation that, while possible, is highly unlikely. Since the buoyancy frequency decreases with altitude in the thermosphere, the highest intrinsic frequency at which non-evanescent gravity waves may exist also decreases with altitude.

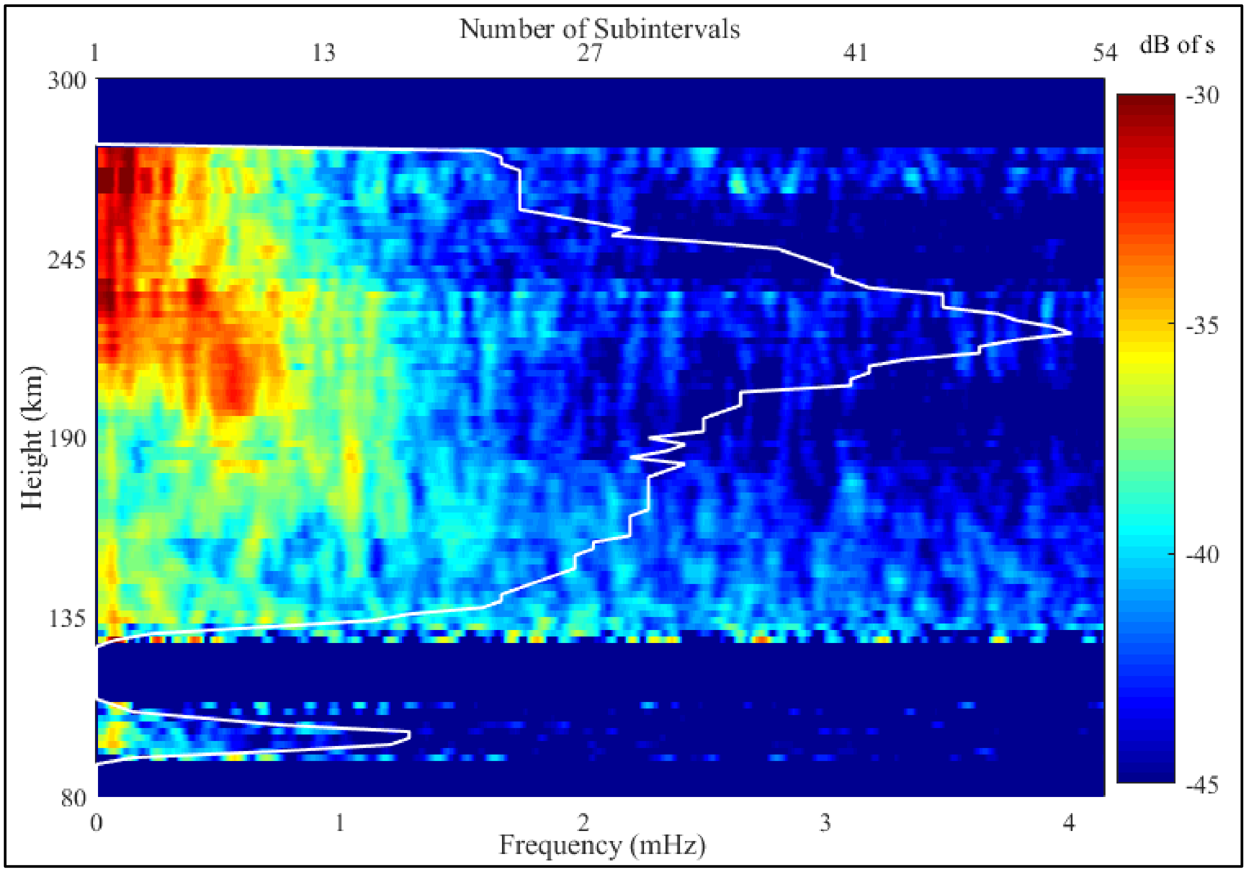

Figure 4.7. Zonal Tilt Power Spectra calculated using the Lomb-Scargle and Welch methods, with no restrictions on the number of points per subintervals and Power Spectral Density integral. The superimposed white line shows the number of subintervals that were used at each altitude to calculate the mean power spectra. Reproduced from Negrea and Zabotin, (2016).

Imposing a filtering criterion that is entirely based on the amount of data available produces better results, as can be observed in Figure 4.8. In this case, the mean spectrum was obtained using only those subintervals that contained a minimum of 80% of the ideal number of data points. The apparent quality of the result in Figure 4.8 is better than that in Figure 4.7, with some of the questionable features removed. Note that the overall height variation of the spectra is similar in the two figures, but the fine structure is more clearly defined in Figure 4.8. The background level above 260 km is again higher than that observed immediately below 260 km. This appears unrealistic, since the buoyancy frequency decreases with altitude, which would prevent the effective propagation of high-frequency components of the spectrum. It is much more likely that this is an artifact caused by the limited amount of data available above 260 km: the impact of a small number of erroneous spectra is augmented as the number of valid subintervals decreases. A threshold could be imposed to discard results calculated using a smaller number of subintervals. However, such a criterion could be somewhat subjective.

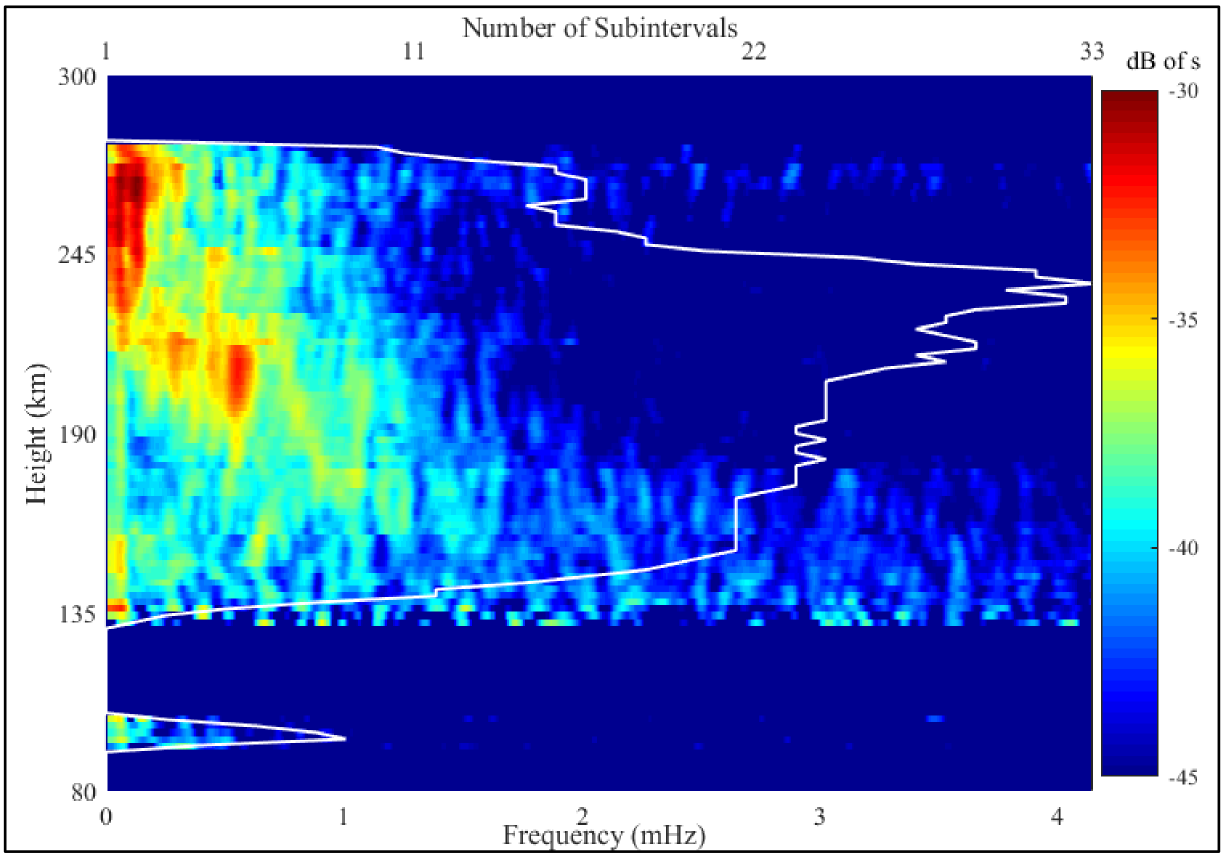

Figure 4.8. Zonal Tilt Power Spectra calculated using the Lomb-Scargle and Welch methods, discarding subintervals with less than 80% of the ideal number of points. The superimposed white line shows the number of subintervals that were used at each altitude to calculate the mean power spectra. Reproduced from Negrea and Zabotin, (2016).

Finally, Figures 4.9 and 4.10 show the zonal and meridional tilt power spectra calculated using our proposed method with a 4% threshold imposed on $\Delta\xi$. This approach has the starting advantage of being based on fundamental theoretical principles that remove the possible impact of subjectivity and assure that results obtained at different altitudes, times, and locations can be used for quantitative comparisons. Figure 4.9, when compared to Figures 4.7 and 4.8, is in much better agreement with existing knowledge on the height dependence of the AGW spectrum (e.g., *Djuth et al.* [2010]). Note that, as the number of subintervals in Figures 4.9 and 4.10 approaches 1, the results become noisier. This is because in these cases our method reduces to the classic Lomb-Scargle method, without the added noise reduction of the Welch method.

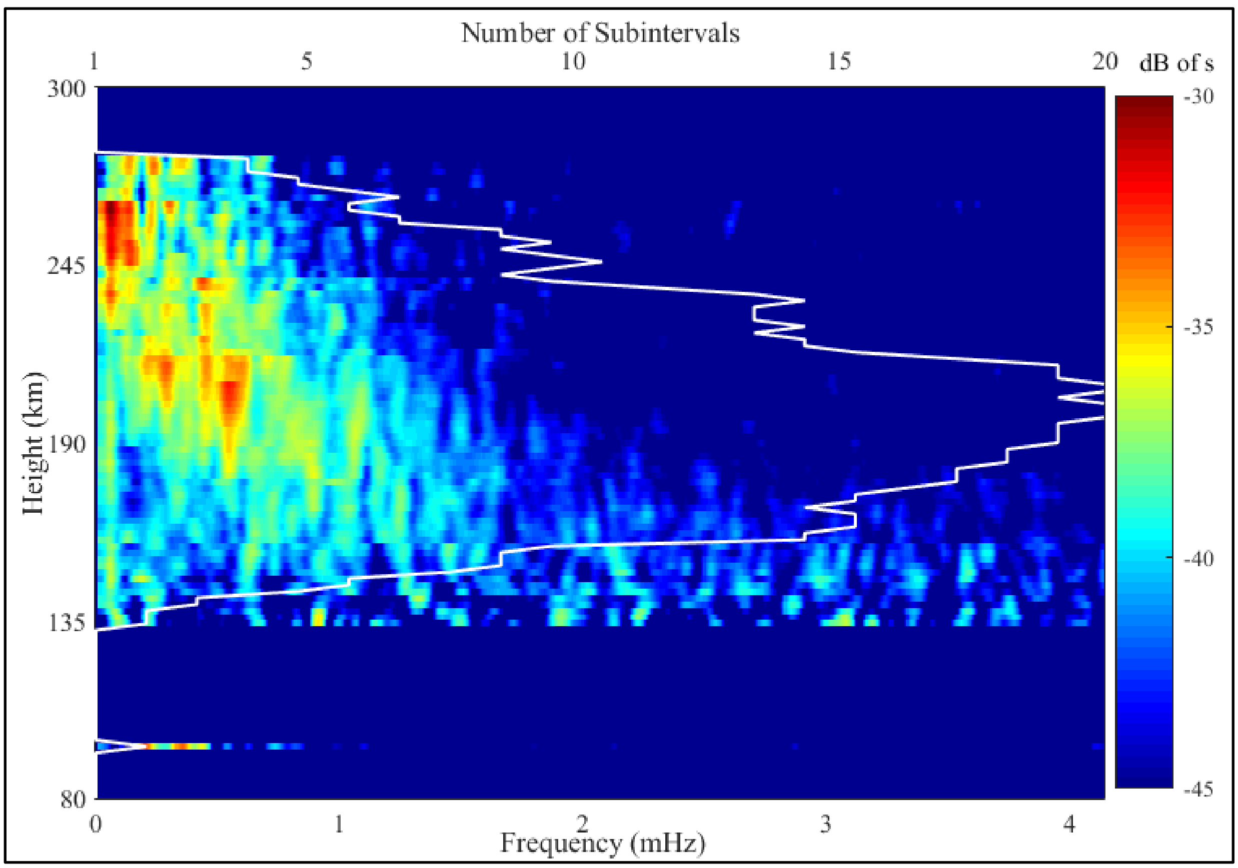

Figure 4.9. Zonal (South-North) Tilt Power Spectra calculated using the Lomb-Scargle and Welch methods, with a maximum tolerable error, $\Delta\xi$ of 4%. The superimposed white

line shows the number of subintervals that were used at each altitude in order to calculate the mean power spectrum. Reproduced from Negrea and Zabotin, (2016).

The approach proposed in this study produces a set of power spectra without introducing height-dependent artifacts while reducing noise as much as possible, allowing for valuable information on the average AGW activity to be obtained. At Wallops Island, for the time interval from 2 October to 11 October 2013, the height dependence of the wave spectrum is characterized by the slant shape, as can be observed in Figures 4.9 and 4.8, with the peak frequency of observed waves decreasing with height. Due to the natural ionospheric variability, the height interval from 80 km up to 220–240 km is mostly indicative of daytime wave activity, and the height interval from 220–240 to 280 km is mostly indicative of nighttime wave activity. A broadband maximum in the spectrum of both tilts is observed between 180 and 220–230 km and at frequencies between 0.1 and 0.8 mHz. A second maximum is observed in the zonal Tilt spectrum between 220 and 280 km at frequencies below 0.2 mHz. This implies a transfer of energy from waves with periods of several tens of minutes to waves with periods of more than one hour as we move up in the altitude. This is likely due to non-linear interactions (*Angelats i Coll and Forbes*, 2002) in addition to energy transfer from AGWs to the mean thermospheric flow and wave reflection due to critical layers (*Vadas et al.*, 2007, *Godin*, 2014). The higher spectral amplitudes more abundant in Figure 4.9 indicate a preferred direction of propagation in the horizontal plane along the West-East axis. This appears to be more pronounced above 220 km. The propagation direction of gravity waves are known to vary significantly with season and geographical position, and this seasonal variability is further investigated in section 4.3.

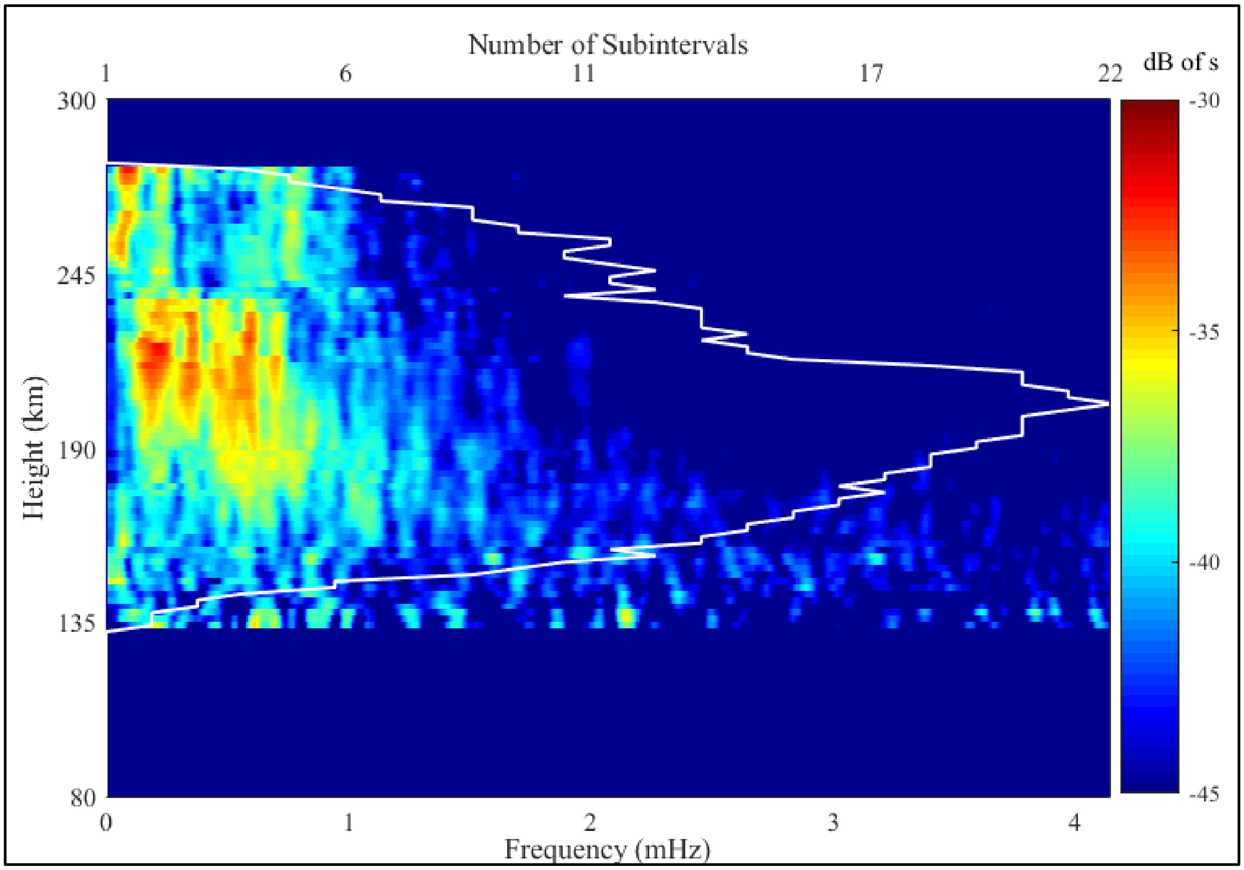

Figure 4.10. Same as Figure 4.9, but for Meridional (West-East) Tilt data. Reproduced from Negrea and Zabotin, (2016).

To summarize, the method proposed here provides clean and smooth results revealing largely expected properties of the thermospheric wave activity. For example, the peak frequency in the spectra decreases with the altitude indicating a transfer of energy from waves with periods of tens of minutes to waves with periods of more than one hour.

The fundamental assumptions behind Equations (4.5) and (4.6) require some discussion. Under ideal conditions, the integral over the entire PSD must equal the time domain variance. In practice, the integral is performed over a limited bandwidth, in this case covering periods from 4 min to 4 hours. At ionospheric altitudes, the diurnal, semidiurnal, and terdiurnal tidal modes constitute an additional source of variability. Since the periods of tidal modes are 24, 12, and 8 hours, respectively, their contributions are not included in the sum on the left-hand-side of Equations (4.5) and (4.6), while the impact on the actual ionospheric variability is present. Using a window of larger size is not desirable due to the high variability of the AGW spectrum that would result in much higher values for ξ_0. The net effect is that results for some subintervals may be discarded if the tidal amplitudes are significant when compared to the total AGW activity. However, this is unlikely to be a systematic problem: the bandwidth occupied by the tidal harmonics is infinitesimal in comparison to that occupied by the AGW spectrum, and their resulting contribution to the PSD integral is generally small.

Finally, a remark on the general validity of the results discussed in this section. The value $\xi_0 = .04 \cdot \sigma^2$ and the results in Figure 4.6 are partially dependent on the specifics of the synthetic datasets used (through the parameters in Equations 4.7). The values chosen here were intended to produce a dataset with characteristics similar to those found in Dynasonde-derived tilt data. While this method is generally valid and applicable to any type of data, the value of 4% for $\Delta\xi$ may not be. Determining an appropriate value for different applications is possible by following the methodology outlined here, with a suitable expression for $A(f)$.

The innovative method described here provides good spectral estimates in the presence of extensive data gaps. Starting from Dynasonde-derived tilt measurements, the AGW spectrum can be correctly obtained and its variation with altitude observed. The method is based on fundamental principles of spectral analysis and has a wide applicability for other types of data characterized by similarly smooth power spectra.

4.3. Seasonal variability of the AGW PSD

The method described in Section 4.2 is a robust spectral analysis technique, and the results shown in Figures 4.9 and 4.10 are accurate estimates of the mean TID PSD representative for the time interval used. The seasonal variability of this quantity is of significant interest and has been investigated using several remote sensing techniques. This section describes results obtained using Dynasonde-derived ionospheric tilts for Wallops Island, VA and Tromso, Norway, from May 2013 to April 2016, and also vertical Doppler speed measurements from Wallops Island, from May 2013 to December 2015. Neither instrument was continuously operational during the entire time interval, but gaps were generally limited to several days, and the spectral analysis technique used mitigates any potential artifacts due to such non-uniformities in the data sampling.

While most problems related to the data sampling have been properly accounted for, there are limitations to this. The spectral analysis technique will discard portions of data for which accurate results cannot be obtained due to the presence of data gaps. The validity of the final result depends on there being sufficient data for which accurate calculations are possible. This condition is not always satisfied. Most notably, the data from the San Juan Dynasonde had to be discarded for the purpose of this work. The operation of that instrument until October 2015 required a periodic data gap every 15 minutes due to operation of a collocated, different ionosonde. The spectral analysis of any dataset from the San Juan Dynasonde could therefore not be accomplished while maintaining the highest accuracy standards.

In addition to problems due to the data sampling, the data analyzed must be of sufficient quality. The zonal and meridional tilts were chosen partly because the SNR of this data product is very high in general, and in particular for the data obtained with the Wallops Island Dynasonde. The tilts themselves are highly susceptible to wave activity as wave-like fluctuations in the plasma density induce wave-like fluctuations in the ionospheric tilts (Equations 4.1 and 4.2), while fluctuations in the background ionosphere are unlikely to induce variations in the tilts, except for limited time intervals close to sunrise and sunset. This makes the tilts ideal indicators for the manifestation of AGWs in the thermosphere-ionosphere. However, the SNR of the tilt data from Tromso, Norway is lower. Figure 4.11 shows the zonal and meridional tilt data from Wallops Island and Tromso, both for the entire month of April 2014 and a 2 day subinterval.

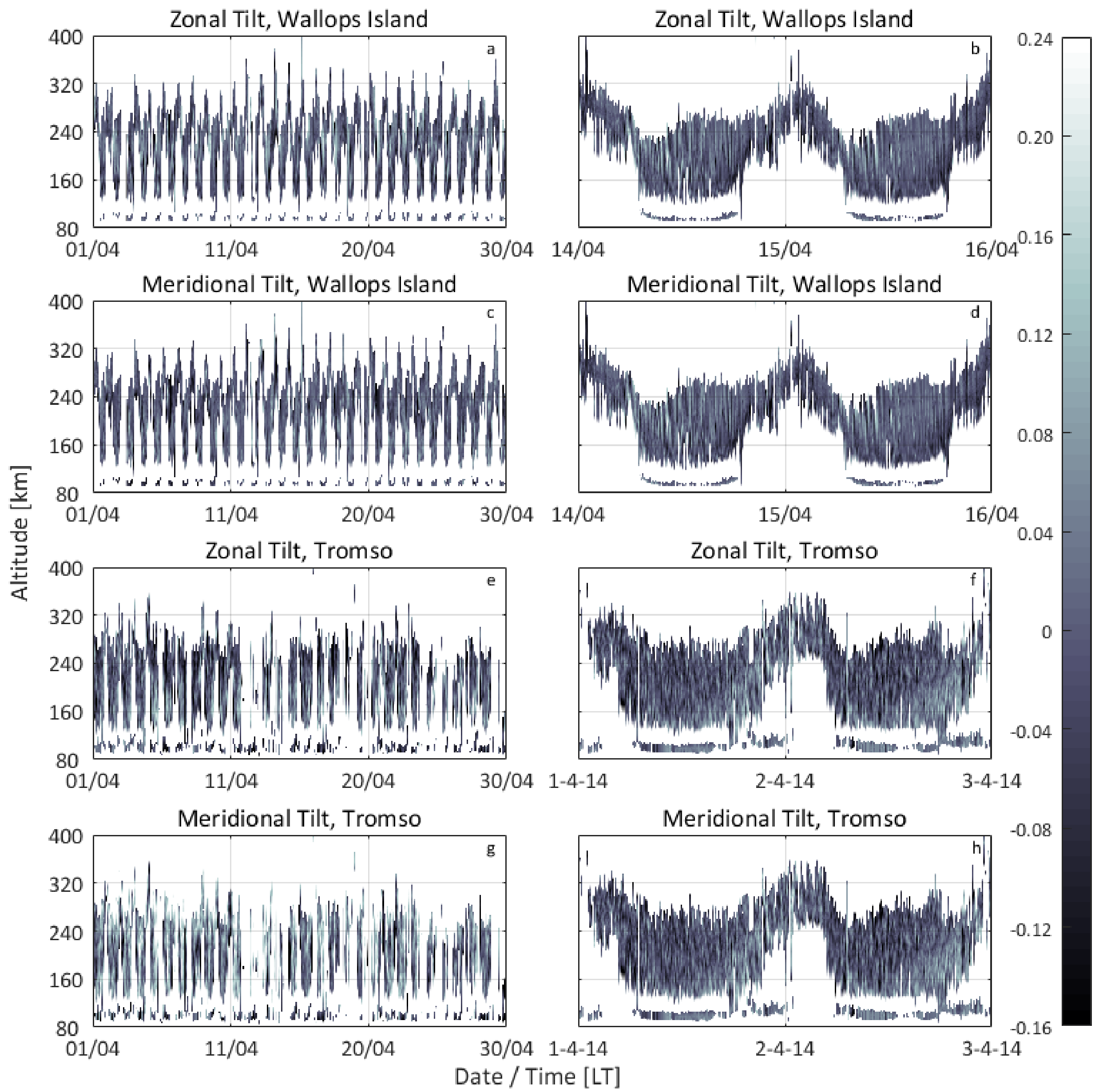

Figure 4.11. Zonal (a, b, e, f) and meridional (c, d, g, h) tilt data from Wallops Island (a, b, c, d) and Tromso (e, f, g, h), covering the whole month of April 2014 (a, c, e, g), and a two-day subinterval (b, d, f, h).

The panels in the left side column of Figure 4.11 (a, c, e, g) show the full extent of the tilt data obtained during a month, highlighting the data sampling. The panels in the right side column of Figure 4.11 (b, d, f, h) show a subset of the same data, highlighting the features due to wave propagation. The spectral characteristics of the data are obtained using the analysis methodology discussed in Section 4.2 (Figure 4.12), with a window size of 4 hours and an overlap between adjacent window positions of 3 hours. It is immediately obvious that the height dependence of the PSD is very different for the two locations. At Wallops Island (a mid-latitude station) we observe a peak in TID activity in an altitude range 60–70 km wide (Figure 4.12 a, b). It is unclear to what extent this is due to a peak in the amplitude of underlying AGWs or due to a stronger ionospheric response to AGWs. The observed peak power moves towards lower frequencies (larger periods) at higher altitudes, and the overall height variation of the spectrum shows a gradual change of the wave spectrum towards larger periods at higher altitudes, from typically 15–20 minutes at 170 km altitude to typically 60 minutes at 240 km. For this dataset, the peak amplitude for the zonal tilt was 1–2 dB higher than the peak amplitude for the meridional tilt. A clear difference between the results at Wallops Island and those at

Tromso is the higher noise level in the Tromso results. This is likely caused by the higher variability in the high-latitude ionosphere.

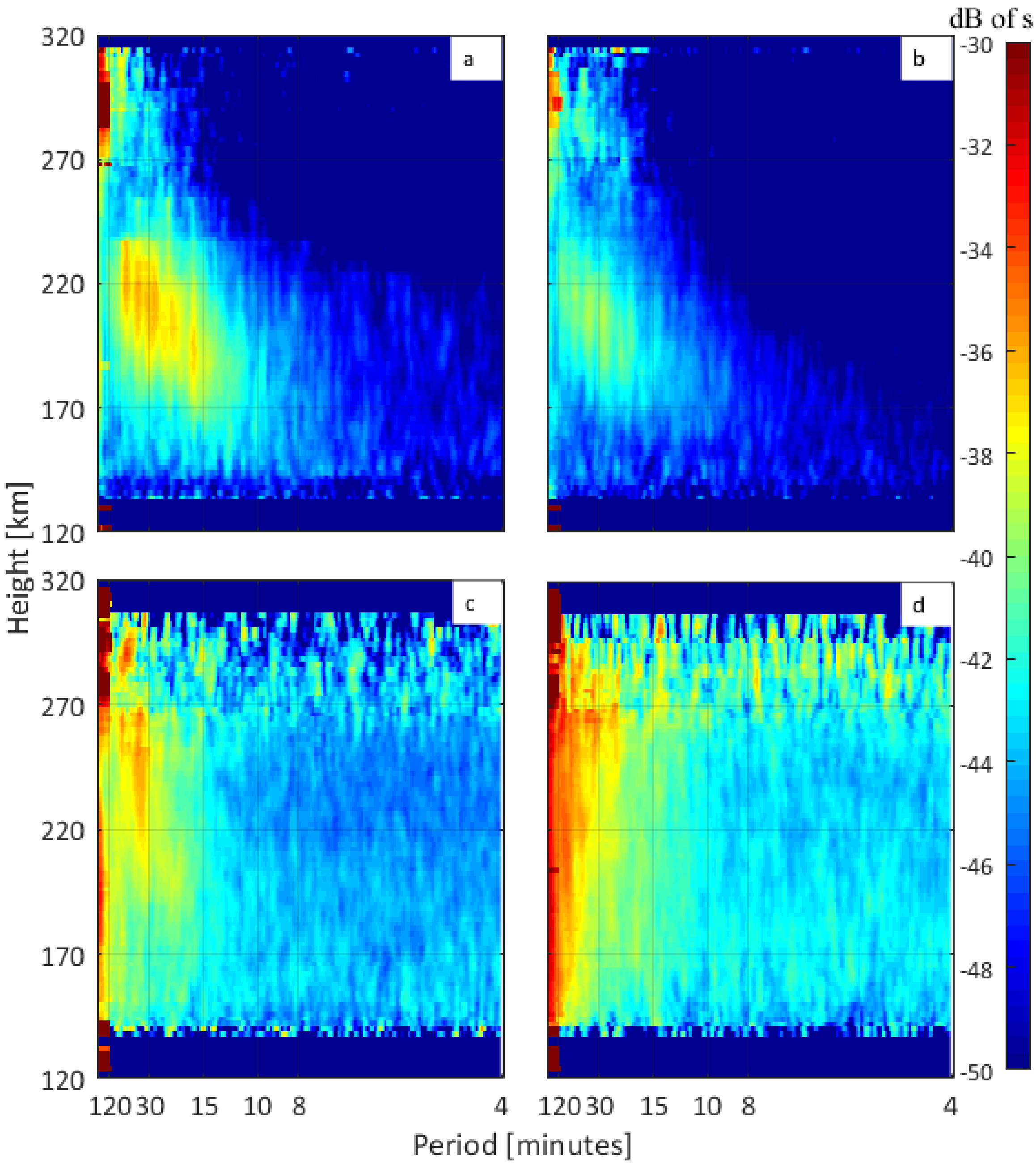

Figure 4.12. PSD during April 2014 for the zonal tilt (a, c) and meridional tilt (b, d), for Wallops Island (a, b) and Tromso (c, d).

By contrast, at Tromso the variation of the PSD with height is much less pronounced. The peak amplitudes for both tilts are at lower frequencies, corresponding to typical periods of 60 minutes and more. For the zonal tilt, there is a slight increase in the PSD corresponding to a period of 40 minutes between 200 and 270 km. The amplitudes for the meridional tilt are generally 1–6 dB higher than for the zonal tilt, and the integral of the meridional tilt PSD is significantly higher than the corresponding PSD integral for the zonal tilt. This is likely an indication of a preferred propagation direction, and is in line with existing knowledge on the nature of southward propagating AGWs generated at high latitudes (*Shiokawa et al.*, 2003; *Frisell et al.*, 2014; *Ishida et al.*, 2008).

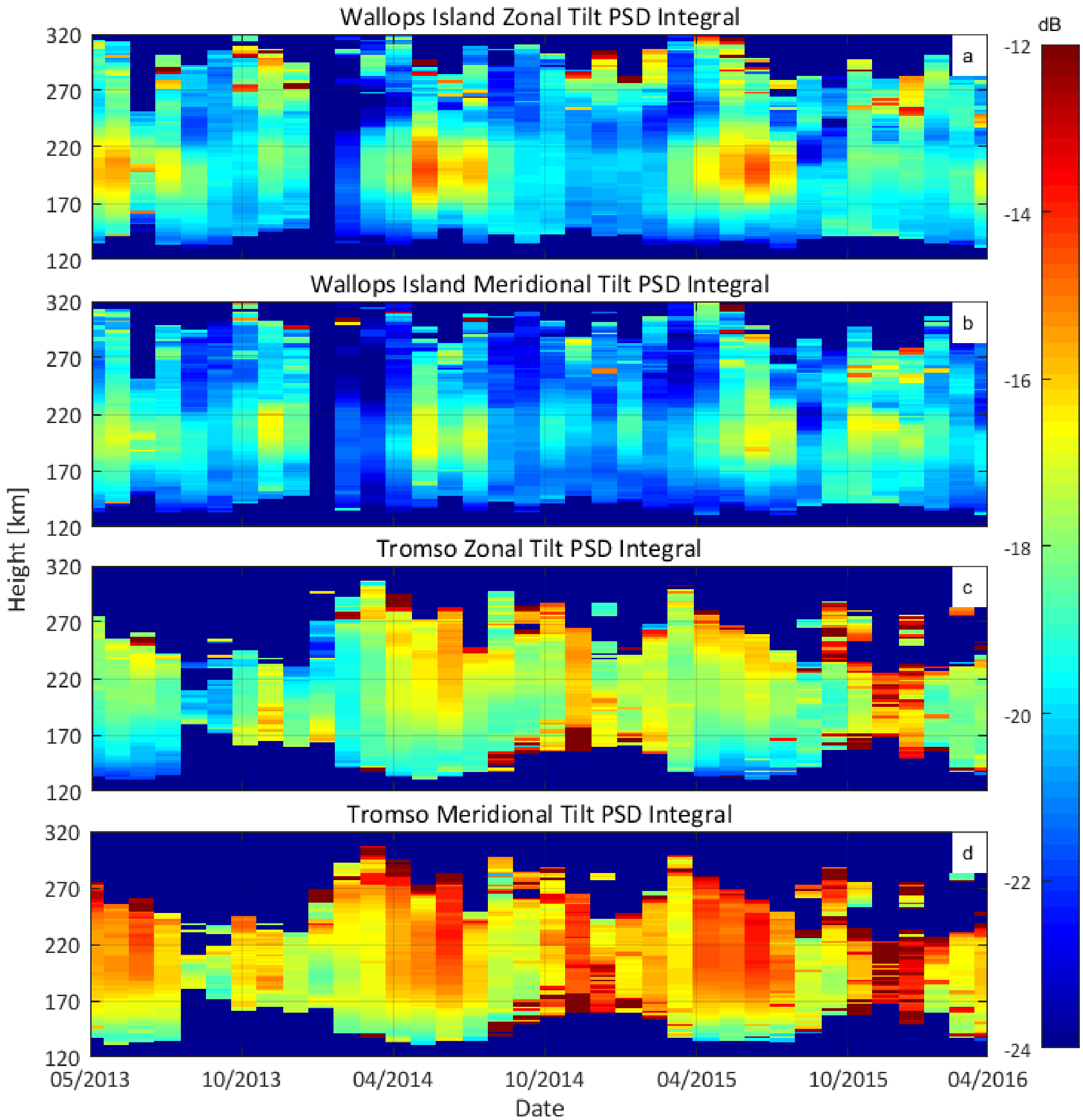

Figure 4.13. Seasonal variability of the PSD integral for the zonal tilt (a, c) and meridional tilt (b, d) obtained using data from Wallops Island (a, b) and Tromso (c, d). Each mean PSD was computed using the analysis methodology outlined in Section 4.2, covering one month, with a window size of 4 hours and a 3 hour overlap between adjacent windows.

The results shown in Figure 4.12 are a "snapshot" of the mean TID PSD, valid for a single month. This seasonal variability of the ionospheric tilts PSD would be an excellent estimator of the seasonal variability of TID activity, allowing for a climatology of TIDs to be formulated. For this purpose, three years of observations at Wallops Island and Tromso were analyzed using the same methodology and spectral analysis technique. 36 mean PSDs are obtained, for each month between May 2013 and April 2016. The PSD is then integrated over frequency at each height for each month. The resulting PSD integral is an estimator of the ionospheric variability due to TIDs. The result is shown in Figure 4.13, for the zonal and meridional tilt at both Wallops Island and Tromso. The differences between the results at the two locations are likely caused by the geographical position of the two instruments, with Wallops Island indicative of mid-latitude TIDs and Tromso for high-latitude TIDs.

The climatology of TID activity has been previously investigated using GPS TEC (*Hernandes-Pajares et al.*, 2006), airglow all-sky imagers (*Shiokawa et al.*, 2003), and SuperDARN radars (*Grocott et al.*, 2013; *Frissell et al.*, 2014, 2016). The major feature highlighted in the existing literature is a peak in wave TID activity during winter, with a sharp decrease during summer. The finer aspects of these studies vary significantly, and because of the individual characteristics of each technique, it is possible that they did not all focus on the exact same population of TIDs. Airglow imagers are susceptible to tropospheric weather due to cloud coverage, which can vary significantly depending on the season. In addition to the drawbacks discussed in Section 3, detection of TIDs using SuperDARN data is more difficult during summer. As discussed by *de Larquier et al.* (2011) and *Frissell et al.*, (2014), during the summer season, the ionospheric E and D layers are enhanced, compared to the winter season. The resulting increased ionospheric absorption suppresses ground scatter, creating this instrumentational bias.

The results for Wallops Island shown in Figure 4.12 (a, b) are in partial agreement with the existing literature, in that there is a clear peak in the meridional tilt PSD integral during the winter of 2013–2014, 2015–2016 and possibly 2014–2015, and a peak in the zonal tilt PSD integral during the winter of 2013–2014 and 2015–2016. However, we observe an increase in the PSD integral during summer for both tilts, for all of the three years analyzed. This is not necessarily a contradiction between the results discussed here and previous results obtained using other remote sensing techniques. The likely conclusion is that TID activity at mid-latitudes has two peaks, one during summer, and one during winter, a fact previously obscured due to observational biases in some studies.

The results for Tromso are shown in Figure 4.13 (c, d), and their interpretation is complicated by the natural seasonal ionospheric variability. During the summer season, the high-latitude ionospheric *F*–Layer occupies a large, and fairly constant altitude range during daytime, resulting in very few data gaps. By contrast, during winter, the number of data gaps is considerably higher, resulting in a smaller number of subintervals for which accurate spectral results can be obtained. The net effect is a more noisy winter PSD (and implicitly, a more noisy winter PSD integral), which can be calculated only for a smaller altitude range. This seems to constitute an observational bias for the time being, and no clear conclusion can be drawn regarding the TID activity at Tromso during the winter season. However, there is a clear increase in TID activity during summer, which is observed over a larger altitude range than at Wallops Island. This is consistent with the properties of the mean PSD noted in the discussion of Figure 4.12.

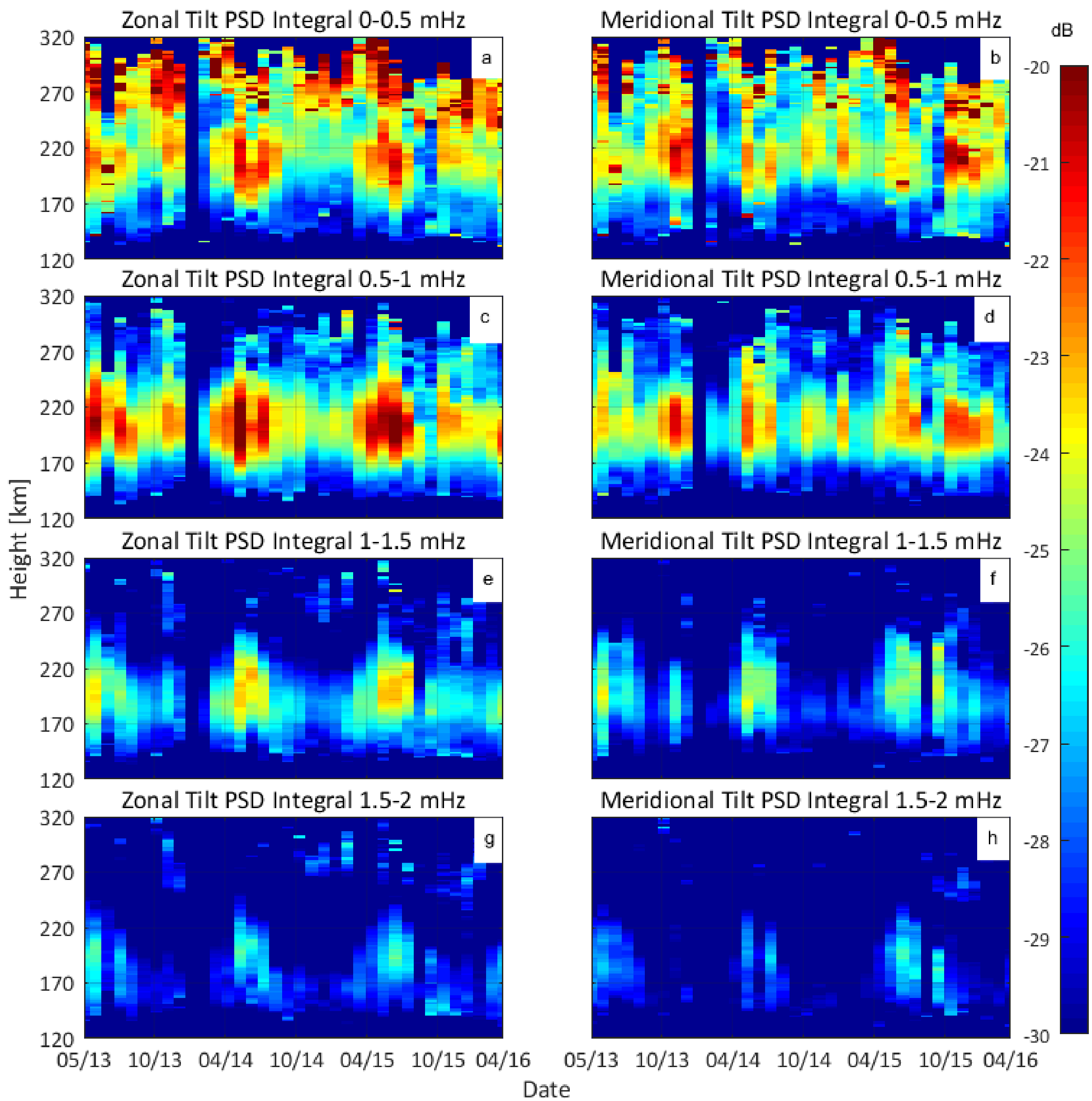

Figure 4.14. Seasonal variability of the Integral of the ionospheric tilts PSD at Wallops Island over 4 bandwidths: 0–0.5 mHz (a, b), 0.5–1 mHz (c, d), 1–1.5 mHz (e, f), 1.5–2 mHz (g, h), for the zonal tilt (a, c, e, g) and meridional tilt (b, d, f, h).

Additionally, a strong anisotropy can be observer, with the meridional tilt PSD integral being up to 4 dB higher than the zonal tilt PSD integral. This is indicative of a preferred southern propagation direction for these high-latitude TIDs.

While the PSD integral is a good estimator of the total ionospheric variability, Figures 4.9, 4.10 and 4.12 show that the PSD dependence on frequency and altitude can be quite complex. To further investigate the seasonal dependence of the ionospheric variability, the PSD integral is determined for four frequency bands (0 – 0.5 mHz, 0.5 – 1 mHz, 1 – 1.5 mHz and 1.5 – 2 mHz) for both locations. The results for Wallops Island are shown in Figure 4.14 and the results for Tromso in Figure 4.15. The increase in ionospheric variability during summer is approximately 4 dB for all bands. However, the winter peak can only be observed at frequencies below 1 mHz. At Tromso, the amplitude of the summer peak varies significantly with altitude, increasing up to 4 dB at 250–270 km. The anisotropy in the propagation direction is present for all bands, but it is much higher (by up to 6 dB) for small frequencies (Figure 4.15, a, b).

While the ionospheric tilt PSD is a strong indicator of ionospheric variability due to TIDs, it is not a direct measurement of TID amplitude, as can be seen in equation 4.2. The dependence of the two tilts on the horizontal wavevector components of the observed TIDs is a useful feature when analyzing spectral results, and can also be used to accurately determine the propagation direction (as will be discussed in more detail in Chapter 5). However, it is necessary to more accurately quantify the seasonal variability of the TID spectrum. For this reason, the Dynasonde Doppler speed measurements are also analyzed for comparison. The mean vertical component of this line-of-sight Doppler speed was determined using all echoes within a given wedge, creating a height profile of the vertical plasma speed. This result was then interpolated to a fixed height grid with a 2 km resolution. Figure 4.16 displays a two-day subset of the Doppler speed data from

Wallops Island. The phase fronts due to AGW propagation can be clearly seen in the data, for most of the length of the dataset.

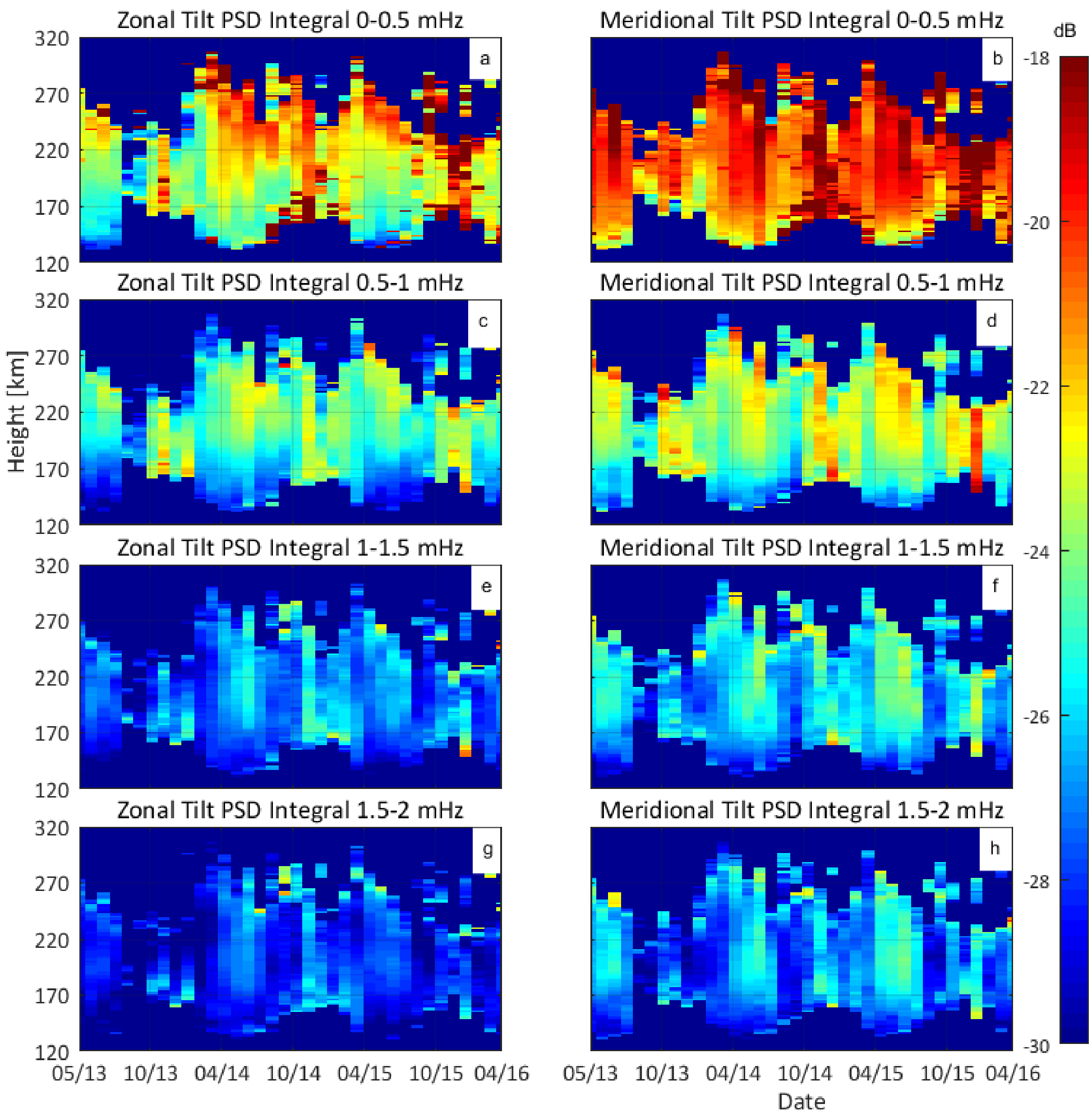

Figure 4.15. Same as Figure 4.14, but for Tromso, Norway.

The spectral analysis procedure used for the tilts is applied to the Doppler speed data, with the added mention that outliers more than one standard deviation from the mean of a 4-hour interval were excluded. The mean PSD for each month is determined, and the integral PSD is determined as before. The result is displayed in Figure 4.17,

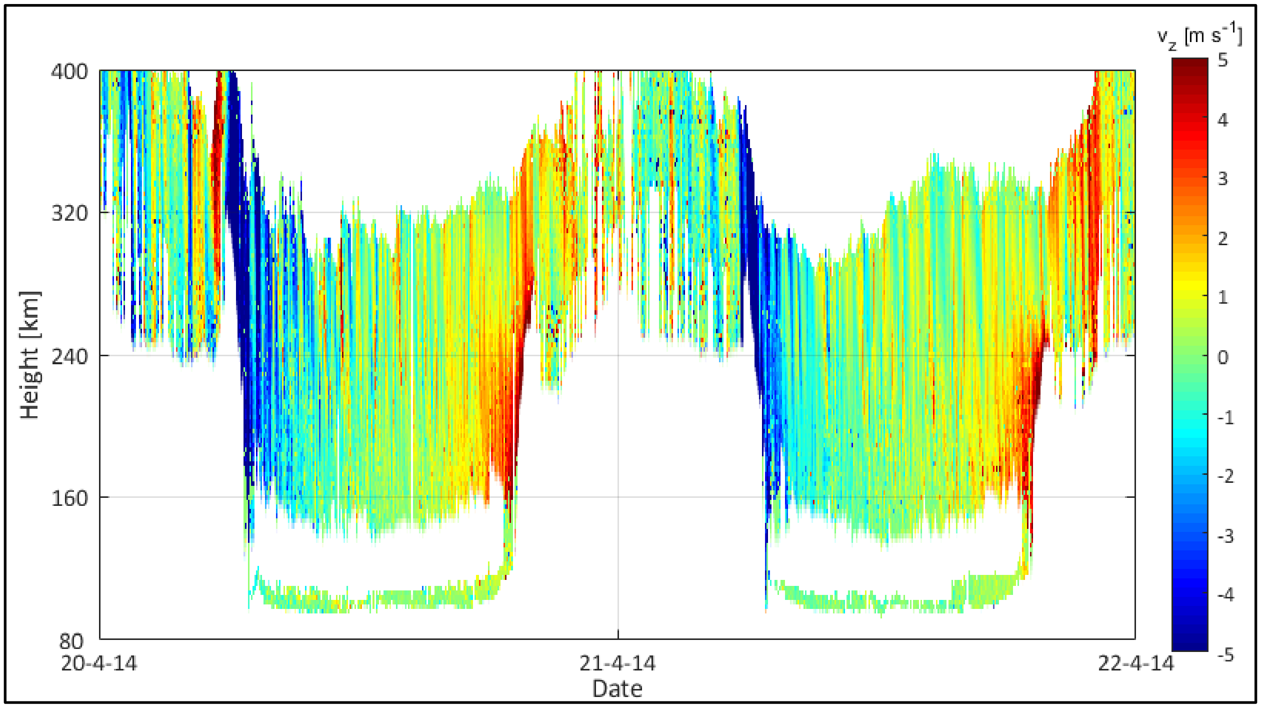

Figure 4.16. Vertical component of the line-of-sight Doppler speed for the whole month of April 2014 (a), and for a two-day subinterval (b). Notice the sharp discrepancy between results obtained before April 20 (with a one minute cadence) and results obtained after that date (with a two minute cadence).

showing the seasonal variability of the vertical plasma speed, which is in itself an indication of the TID activity. The temporal coverage is slightly more reduced than for the ionospheric tilts, between May 2013 and December 2015. The seasonal dependence of the Doppler speed PSD integral shows two peaks every year, one in summer and one in winter. This confirms the conclusions based on the tilt PSD integral. However, the vertical plasma speed is directly proportional to the amplitude of TID activity. The existence of a peak in TID activity during the summer season is a significant geophysical result, providing a clearer image on the climatology of mid-latitude TIDs. The relative amplitude of the summer and winter peaks can be evaluated, with three summer and two winter periods available. There is an increase in amplitude from the summer of 2013 to the winter of 2013 – 2014, but also an increase in amplitude from the winter of 2014 – 2015 to the summer of 2015. At this stage, this issue cannot be further investigated due to the lack of additional data, but this will hopefully be addressed as more data becomes available.

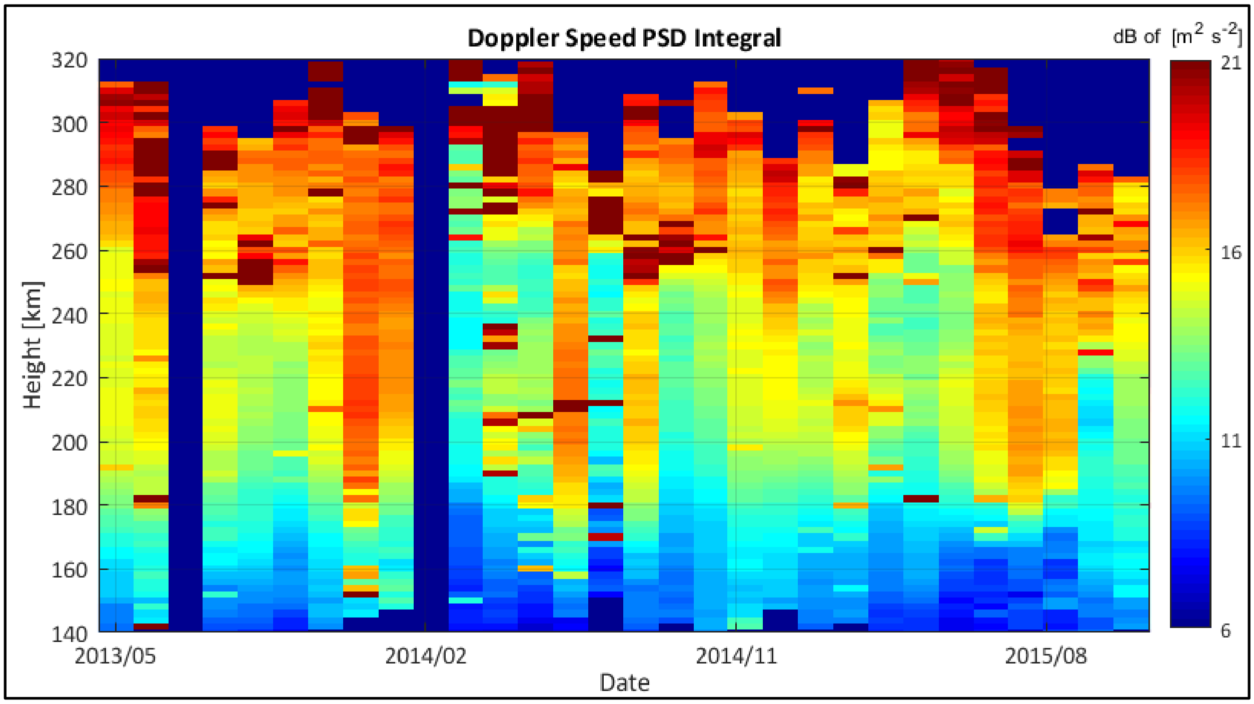

Figure 4.17. Seasonal variability of the Doppler Speed PSD at Wallops Island, between May 2013 and December 2015.

4.4. Ionospheric response to tidal waves

A specific class of TIDs are manifestations of atmospheric thermal waves (tides) with frequencies that are harmonics of 24 hours. The relative impact of tides is generally greater during periods of reduced solar activity, but it is always present. The main source of tidal oscillations is known to be the absorption of solar radiation by tropospheric H_2O

and stratospheric O_3 (*Groves*, 1981a, *Groves*, 1981b). These waves propagate upward and increase in amplitude as the background density decreases. Their spectra are modified by non-linear interactions *(Angelats I Coll and Forbes*, 2002; *Huang et al.*, 2012, *Titelbaum and Vial*, 1991) and by in-situ excitation of non-migrating tidal modes in the thermosphere (*Jones et al.*, 2013).

The tides influence background characteristics of the thermosphere-ionosphere system by dumping their momentum into the mean flow as they dissipate and by affecting the wind dynamo in the *E*–region. The overall importance of migrating and non-migrating tidal modes has been amply demonstrated by modelling studies (*Fang et al.* 2013, *Oberheide et al.* 2002, *Oberheide et al.* 2009, *Oberheide et al.* 2011, *Chen et al*. 2013, *Forbes et al.* 2001, *Hagan and Forbes*, 2002, *Yamazaki and Richmond*, 2013, *Lu et al.* 2012, *Jones et al.* 2013, *Jones et al.* 2014, *Akmaev et al.* 2008), and, to a lesser extent, by satellite and ground-based data. However, research has been hindered by the so-called "thermospheric gap" in the data (*Oberheide et al.* 2011), referring to the altitude range between 120 and 400 km, for which global tidal measurements are currently sparse. As a result, recent studies using various types of measurements have focused on either the lower thermosphere (below 120 km), the upper thermosphere (above 400 km), or have used datasets covering short time intervals or limited altitude ranges. The height profile of tidal harmonics has been studied using Incoherent Scatter Radar measurements (*Huang et al.* 2012, *Gong and Zhou* 2011, *Hocke* 1996). The long term impact due to tides on the large scale structure of the ionosphere has been investigated using NmF_2 data from digisonde stations (*Forbes et al.* 2000) and the global impact of tidal modes has been investigated using satellite observations (*McLandress et al.* 1996).

However, current satellite missions do not provide data above 120 km (*Forbes et al.* 2006, *Warner and Oberheide*, 2014). One notable exception are results obtained with COSMIC data (*Mukhtarov and Panceva*, 2011), which suggested the presence of several altitude ranges of enhanced ionospheric response to atmospheric tides, below 250 km and above 300 km. Finally, *Hausler et al. 2014* showed limitations to the existing methodologies for tidal studies reliant on satellite measurements, suggesting a need for ground based observations. The development described here may be considered a response to this demand by proposing the use of Dynasonde methods for the study of thermospheric tidal waves.

For this section, the average height profiles of tidal amplitude and phase are determined for the diurnal, semidiurnal and terdiurnal tidal harmonics over Wallops Island, VA and San Juan, PR. This is done for two time intervals: May 6, 11:18 – June 6, 10:50 and October 9, 00:00 – November 8 23:58, both in 2013. These were chosen such that observations at both locations would be available for 31 uninterrupted days. Seasonal, latitude and altitude variations of the first three tidal harmonics are captured. The zonal (west-east) tilt is our preferred parameter since it is normalized by the magnitude of the electron density gradient (and therefore less dependent on diurnal variations of ionization) and due to the fact that Earth's west-to-east rotation determines the principal direction of propagation of the tidal waves. However, the electron density and zonal component of the electron density gradient are also used.

The ionospheric perturbation induced by a superposition of tidal modes is expected to have the following form (*Forbes,* 1995):

$$N_{e_m}(z,t) = \sum_s N_{e_{m,s}}(z)\cos[m\Omega\big(t - t_m(z)\big) + sl] \qquad (4.8)$$

where *m* is a subharmonic of one day, *s* is the zonal wave number, $N_{e_{m,s}}$ is the amplitude of a single mode, *l* is the longitude (expressed in rad), $\Omega = \frac{2\pi}{24 \text{ hours}}$ is the Earth's rotation frequency, *t* is the local time in hours, and t_m is the local time corresponding to the maximum of subharmonic *m*. It is obvious that if a neutral atmosphere oscillation induces an ionospheric response with the time dependence described by equation (4.8), the electron density gradient, and implicitly also the associated tilt, must exhibit similar oscillatory behavior:

$$\nabla_x N_e(z,t) = -\frac{1}{R_E * \cos(\Phi)} \sum_s s\, N_{e_{m,s}}(z) \sin[m\Omega(t - t_m(z)) + sl] \qquad (4.9)$$

where R_E is the radius of the Earth and Φ is the latitude. It is possible that a local variation in electron density may be mistakenly attributed to a tidal mode. This is less likely to be the case for the tilt measurement as this is indicative of the spatial structure over a large area within the stations' field of view. There is a simple relationship between the horizontal and vertical components of the gradient and the tilt values:

$$\nabla_x N_e(z,t) = \frac{n_x \nabla_z N_e}{\sqrt{1 - n_x^2 - n_y^2}} \qquad (4.10)$$

We used data from the Wallops Island and San Juan Dynasondes. The zonal tilt and the electron density profiles are direct products of Dynasonde analysis while the zonal component of the gradient was derived using equation (4.10). All three quantities are expected to be susceptible to the tidal phenomena, as may be concluded from equations (4.8) – (4.10). The time periods used are 31 days in May-June 2013 and 31 days in October-November 2013. Analyses for the two locations were entirely independent. Each spectral harmonic in the spectra is the result of superposition of several tidal modes, propagating both eastward and westward, and, in the case of the diurnal variation, superimposed with the tidal effects is the normal diurnal ionospheric variation due to changes in ionization from daytime to nighttime.

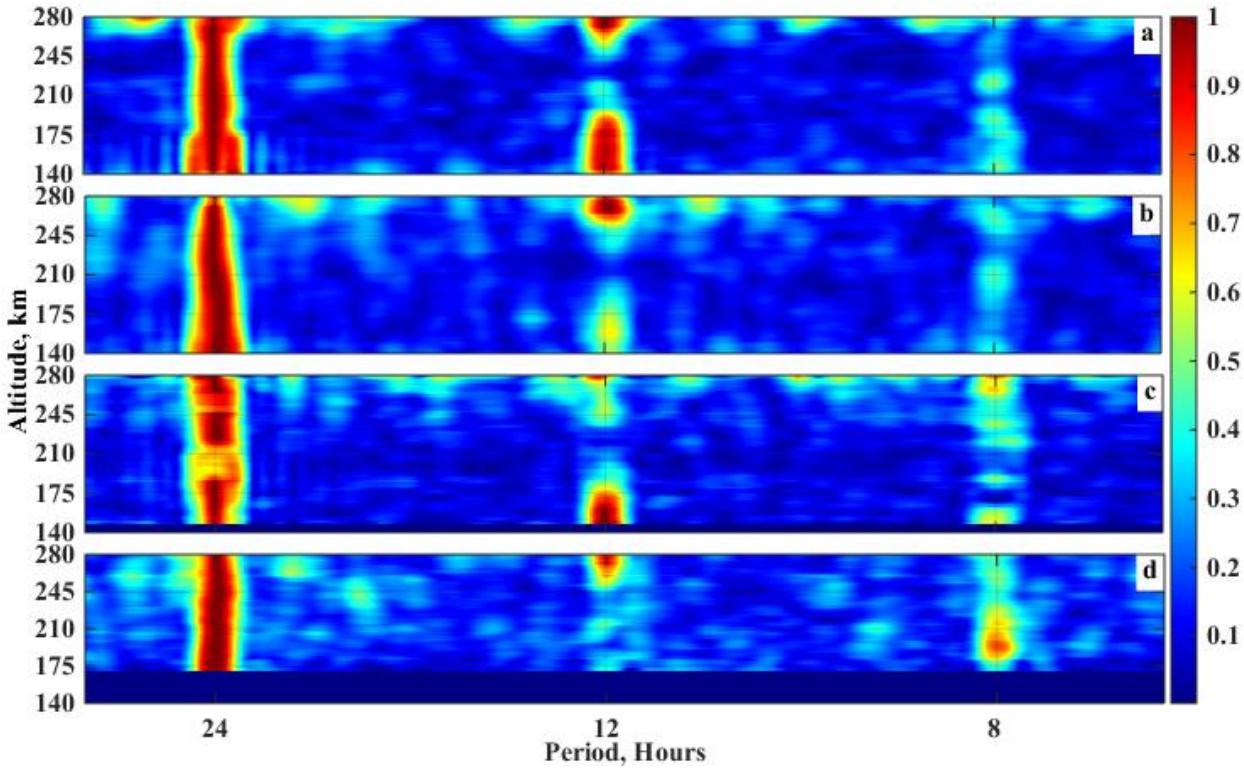

Figure 4.18. Normalized periodograms of the West-East ionospheric tilt obtained by the Dynasonde-based technique for Wallops Island, VA, October-November(a) and May-June (b) 2013 and San Juan, PR, October-November (c) and May-June (d) 2013. One can clearly see the diurnal, semidiurnal and terdiurnal harmonics in a very broad altitude range. Reproduced from Negrea et al. (2016a).

As discussed in Section 4.1, basic spectral analysis tools such as the FFT are unsuitable for use with the Dynasonde data. The spectral analysis tool that we need has to provide objectively comparable results for different time periods, different altitudes and different locations. The Lomb-Scargle periodogram technique (*Scargle*, 1982, *Scargle*, 1989) satisfies all the requirements. The Lomb-Scargle implementation we use is based on that developed by *Hocke and Kampfer*, 2009; it allows simultaneous determination of both magnitude and phase of Fourier equivalent spectra. The technique was modified slightly to work for an arbitrary set of frequencies. When determining the amplitude, the algorithm was applied to data segments obtained with a sliding Welch (*Welch,* 1967) window of 20 days and a 12 hour step; the results were averaged over all 23 steps. The phase was determined in a single step, using the entire 31 day time interval, due to the fact that the Welch method has traditionally only been used to calculate spectral amplitudes and due to the known high variability of the phase of tidal modes (*Murphy,* 2002).

The gap configuration specific to Dynasonde data introduces an added difficulty. For most constant altitudes, the size of the data gap can be as large as 12 hours for a 24 hour interval. This still allows for an accurate fit for the semidiurnal and terdiurnal harmonics. However, *Zhou et al.* (1997) and *Gong et al.* (2013) showed possible errors in the case of the diurnal harmonic, even with the use of the Lomb-Scargle method. While a comprehensive solution to this problem is beyond the scope of this work, a partial solution is used. *Zhou et al.* (1997) suggests that a tidal harmonic is questionable if it has a small amplitude and random phase variation. In order to avoid such dubious results, at each altitude, a tidal harmonic is considered relevant if its amplitude is 3 times the standard deviation above the mean amplitude. Figure 4.18 uses color scale to show the Lomb-Scargle results for the zonal tilt as a function of the period and altitude. For this illustration, each periodogram (for every altitude) was independently calculated and normalized by its maximum value. One can clearly see the ability of the Dynasonde-based technique to reveal major tidal harmonics in a very broad altitude range.

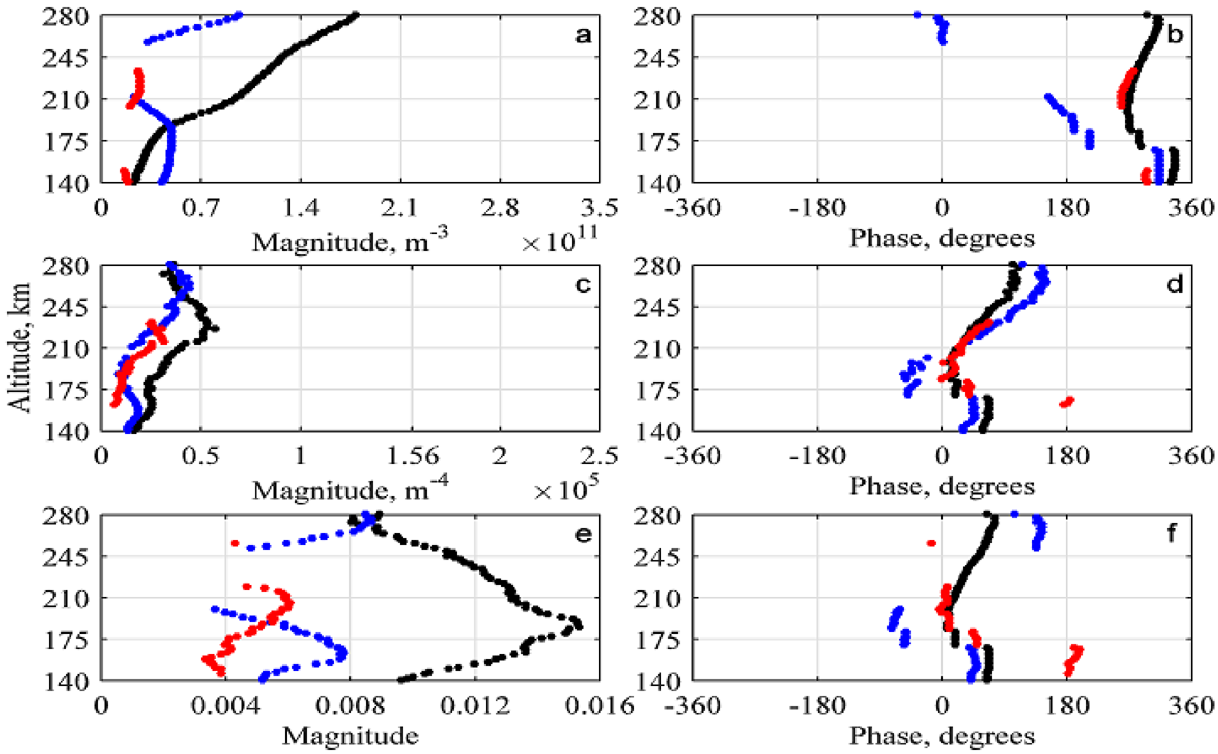

Figure 4.19. Amplitude (a,c,e) and phase (b,d,f) height profiles for the diurnal (black), semidiurnal (blue) and terdiurnal (red) harmonics in the electron density variations (a,b), in the West-East gradient (c,d), and in the West-East tilt (e,f) at Wallops Island, VA, for May-June 2013.

Equation (4.8) was initially introduced to describe tidal oscillations directly caused by absorption of solar radiation (*Chapman and Lindzen*, 1970). Some other processes are known to cause oscillations with the same periods, sometimes being referred to as "pseudo-tides", as opposed to the solar thermal tides (*Vadas et al.* 2014, *Walterscheid et al.*1986). In this paper, we broadly refer to all Fourier coefficients corresponding to harmonics of 24 hours as "tidal" amplitudes. The diurnal tidal harmonic (m=1) is superimposed over the variability of photo-ionization, usually resulting in the overestimation of the diurnal tidal harmonic when a non-discriminative approach is used. Note however that while the distortion of the diurnal harmonic describing electron density variations is expected to be significant, the effect of photo-ionization on the tilts and gradients is much smaller.

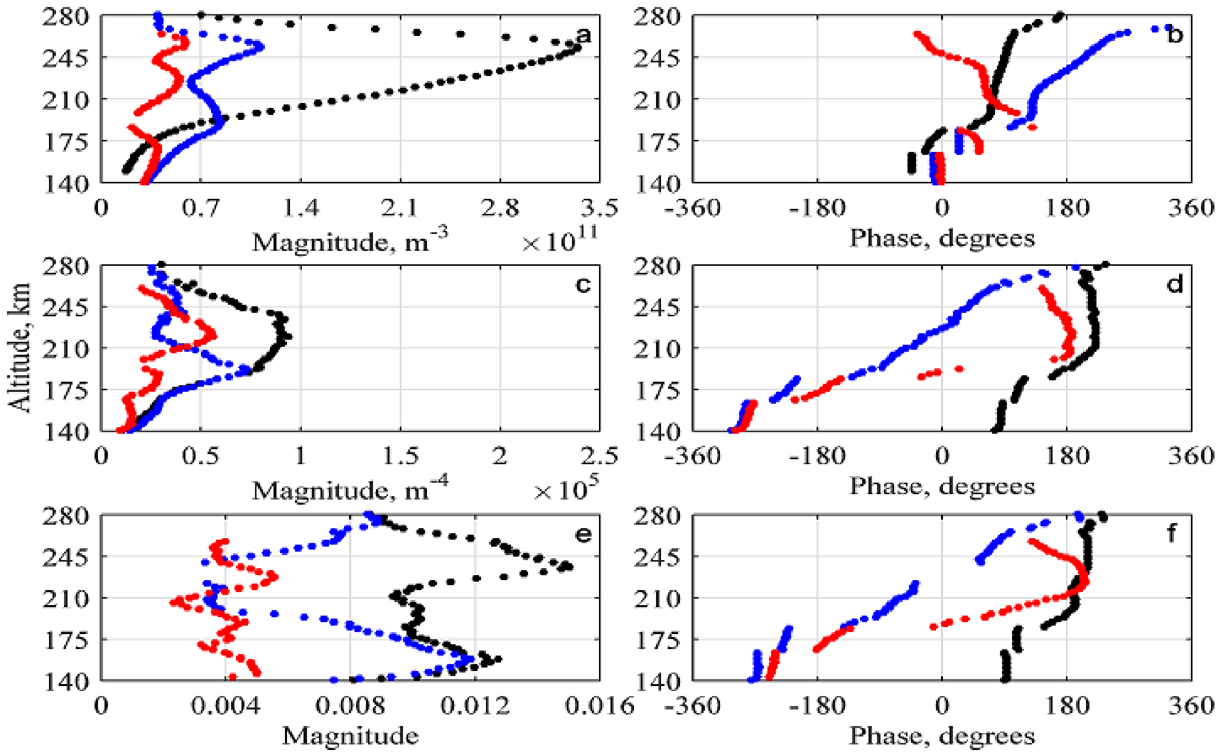

Figure 4.20. Same as in Figure 4.19, but for October-November 2013.

The set of Figures (4.19) – (4.22) illustrates altitude dependencies of the amplitude and phase of the three major tidal harmonics as revealed by our analysis for the two locations and the two periods. We provide numerical results for all three physical quantities that were previously introduced as possible indicators of the tidal oscillations: electron density, tilts and horizontal gradients.

The structure of the height profiles corresponding to each of the three harmonics may be explained by simultaneous manifestation of several tidal modes with the same frequency. Each mode is likely to have one or more maxima and minima, their height distributions may vary depending on the zonal wavenumber. One possibility is that a single mode may have a dominant contribution to the amplitude of its corresponding harmonic. In such cases, the summation on the right hand side in Equations (4.8) and (4.9) reduces to a single term and the phase shift between the electron density and its gradient is expected to be either $\frac{\pi}{2}$ or $-\frac{\pi}{2}$, for a westward or eastward propagating mode, respectively. Examples of this behavior may be found in Figure 4.19 for the diurnal and semidiurnal harmonics below 175 km, Figure 4.19 for the terdiurnal harmonic between 210 and 240 km and in Figure 4.20 for the diurnal harmonic above 180 km and the semidiurnal harmonic above 260 km. For a superposition of waves, Equations (4.8) and (4.9) suggest this can no longer be the case, particularly if modes propagating in both directions are present. The altitude profiles of the phase show significant jumps, such as in Figure 4.19.f for the terdiurnal harmonic between 175 and 185 km and in Figure 4.20.b for the terdiurnal harmonic at 195 km. A smooth variation of the phase with altitude indicates the presence of wave modes covering the entire altitude range being considered, such as can be observed in Figure 4.21 for the terdiurnal harmonic. By contrast, the phase jumps indicate significant differences between the wave modes present above and below the jump. Possible explanations are interference of several modes with different height profiles and/or a manifestation of different tidal excitation mechanisms (*Jones et al.*, 2013; *Walterscheid et al.*1986).

Phase variation with height is indicative of vertical propagation of the respective tidal harmonic. A typical feature of tidal and gravity waves is that the vertical phase speed must have an opposite sign to that of the vertical component of the group velocity. As such, the phase increase and decrease with height is indicative of downward and upward propagation, respectively. The phase results for the electron density, electron density gradient and West-East tilt are not necessarily in agreement, and this is explained by the differences between Equations (4.8) and (4.10). The propagation direction for the diurnal harmonic should not be determined exclusively based on the phase results obtained for electron density due to the potential bias introduced by the diurnal variation in photo-ionization. At Wallops Island, Figure 4.19 (b, d, f) shows downward propagation of the diurnal harmonic between 270 km and 210 km, and possibly also downward propagation for the semidiurnal harmonic within the same height interval. For the period of October-November, Figure 4.20 (b,d,f) shows downward propagation for the diurnal harmonic between 180 and 280 km, while the terdiurnal harmonic is propagating upward above 240 km and downward below 215 km. At San Juan, during the time interval in May-June 2013, our results (Figure 4.21 b,d,f) showed only small phase variations for the diurnal and terdiurnal harmonics. Finally, Figure 4.22 (b,d,f) indicates upward propagation for the semidiurnal harmonic between 180 and 210 km and downward propagation for the terdiurnal harmonic above 210 km.

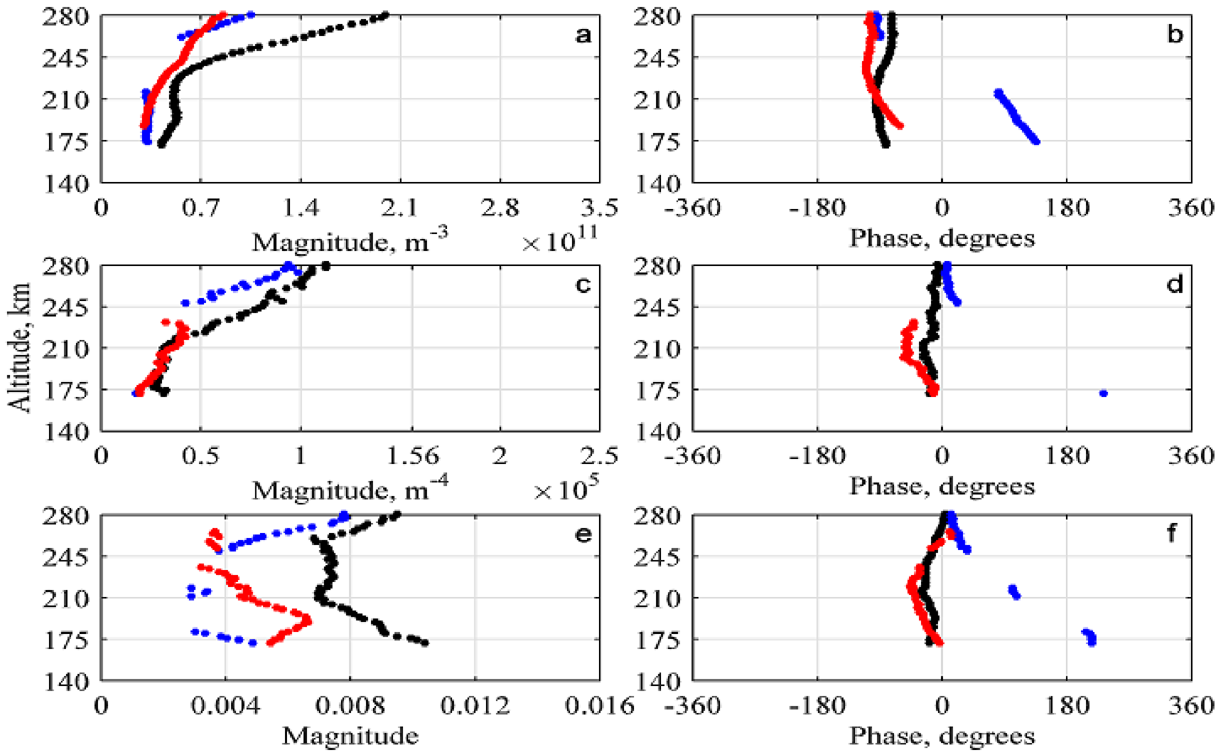

Figure 4.21. Same as in Figure 4.20, but at San Juan, PR, and for May-June 2013.

Tidal signatures show significant altitude and seasonal variability at both locations. The semidiurnal harmonic at Wallops Island exhibits two altitude ranges of enhanced amplitude: below 200 km and above 245 km. This is valid for both datasets and such a feature has been previously reported (*Mukhtarov and Panceva*, 2011). The particular datasets used here indicate that the separation between the two regions may be as small as 50 km. The terdiurnal harmonic at Wallops Island in October-November exhibits at least 3 maxima. By combining information in panels a,c and e in Figure 4.20, four such distinct maxima can be identified. The amplitude of the semidiurnal and terdiurnal harmonics in the electron density at Wallops Island varies between $.5 \cdot 10^{11} – 1 \cdot 10^{11}$ and $.2 \cdot 10^{11}$ - $.6 \cdot 10^{11}$ m^{-3}, respectively. At San Juan, the semidiurnal and terdiurnal harmonics exhibit amplitudes of $.2 \cdot 10^{11}$ - $2.1 \cdot 10^{11}$ and $2 \cdot 10^{11}$ - $.8 \cdot 10^{11}$ m^{-3}, respectively. The range for the amplitudes of both the semidiurnal and terdiurnal harmonics are similar to those previously reported by (*Mukhtarov and Panceva*, 2011).

This study demonstrates a possibility to infer ionospheric features caused by tidal modes using Dynasonde data. The techniques used in this section are consistent with those applied in this work for the study of AGWs, within the general framework of spectral analysis. Global measurements of atmospheric tides are currently not available and local measurements have been scarce and until now only covering short time intervals. The methodology used in this study can be extended for other Dynasonde-capable instruments. An important feature of the HF radars, lacking for other ground-based instruments, is their ability to operate continuously with low operational costs. Long term studies are thus possible covering a broad geographical latitude interval. This provides a way to “fill” the gap for tidal measurements in the thermosphere. The tilt measurement is particularly useful in detecting tidal and wave features in general, as it is sensitive to wave-like perturbations and explicitly normalized.

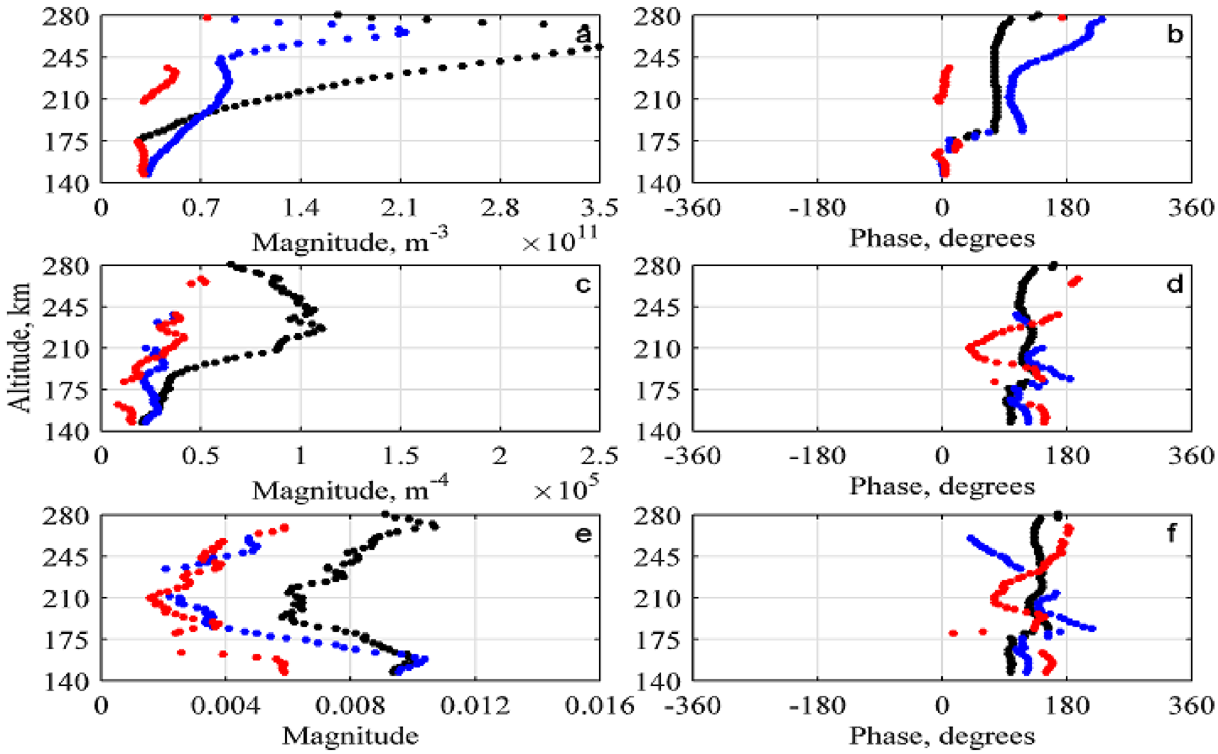

Figure 4.22. Same as in Figure 4.19, but for October-November 2013.

CHAPTER 5

THE PROPAGATION PARAMETERS OF TIDS AND AGWS

5.1. Introduction

A single harmonic of an acoustic gravity wave may be approximated locally (and within a very narrow altitude interval) by a plane wave model, which is characterized by a small set of parameters: frequency, horizontal and vertical wavelength, phase, propagation direction and amplitude:

$$p = p_0(\omega)\exp[i(\boldsymbol{k}\cdot\boldsymbol{r} - \omega t)] \qquad , \tag{5.1}$$

where p describes variations of a physical parameter of the medium (e.g., temperature, density, etc.), p_0 is the amplitude of these variations, $\boldsymbol{k}$ is the wavevector, $\boldsymbol{r}$ is the position vector, $\omega = \omega_0 + \boldsymbol{k}\cdot\boldsymbol{u}$ is the ground based angular frequency, $\omega_0 = \frac{2\pi}{\Delta T}$ is the intrinsic frequency, ΔT is the wave period, t is the time, and $\boldsymbol{u}$ is the background neutral wind velocity. All other relevant parameters (group velocity, phase speed, energy and momentum, etc.) can be obtained from the prescribed set. Unfortunately, determining the full set is a challenging task, established techniques being able to provide some subset of parameters with either limited (i) altitude or (ii) temporal coverage.

Ishida et al. (2008) used measurements from the Kodiak, King Salmon and Hokkaido (all in the Northern Hemisphere) SuperDARN stations to obtain the frequency, horizontal wavelength and derived horizontal group velocity and propagation direction

Statistics can be computed and as the SuperDARN network is expanded, a larger geographical region will be covered. Existing results seem to indicate a higher occurrence rate of TIDs at higher latitudes. *Grocott et al.* (2013) obtained similar results with the Southern Hemisphere Falkland Islands SuperDARN installation. The method can offer valuable information, but is limited by its inability to determine k_z and the height dependence of the results.

Shiokawa et al. (2003) used all-sky imagers at two locations in Japan to determine the period, horizontal wavelength, and velocity of TIDs. The technique allows for statistics to be computed, determining the seasonal variability of TIDs. However, measurements can be made only at night and only in the absence of cloud cover, introducing a serious limitation. In addition to this, the airglow intensity is integrated across an altitude interval as large as 100 km. The vertical wavevector cannot be determined and any height variation is also lost.

Hernandez-Pajarez et al. (2006) used GPS TEC data to obtain the "apparent" horizontal wavelength, period, propagation direction, and derived horizontal velocity. The integral nature of the TEC measurements does not allow for any height variability to be determined, although results are likely to be most representative for the F2 Layer. Also, the vertical wavevector component cannot be directly measured. The precision of the results primarily depends on the density of GPS receivers and the method can potentially be used to obtain globally valid results, or with wide geographical coverage.

Of established remote sensing methods, ISR is the only one capable of providing the full set of wave parameters for gravity waves in the thermosphere-ionosphere. *Nicolls and Heinselmann* (2007) used measurements of the Poker Flat Incoherent Scatter Radar and results of the Mass Spectrometer and Incoherent Scatter Radar (MSIS) model results to test the consistency of their results with the dissipative gravity wave dispersion relation derived by *Vadas and Fritts* (2005). This is, to my knowledge, the only effort of this kind that has been published. Ten beams were used to obtain 3D information and all three wavevector parameters. A single dominant wavemode was selected at any given altitude, over an 85 km height interval. The k_z values obtained directly from the data were compared to values predicted by the dispersion relation using the measured frequency and horizontal wavelength. The conclusion of the authors that the TIDs they observed are caused by gravity waves is probably correct. However, their results show differences of tens to hundreds of km between the measured and calculated values of λ_z.

The relation between $\vec{k}$ and ω, or the relation between a wave's spatial and spectral characteristics and the background atmospheric conditions, is referred to as the dispersion relation. *Fritts and Alexander* (2003) describe a simple version of it, assuming an isothermal, single species atmosphere and neglecting molecular viscosity, thermal diffusivity, ion drag and other phenomena that may be significant above 150-200 km. *Vadas and Fritts* (2005) improved on this by including the viscous damping and thermal diffusivity effects. The result is a better account of wave attenuation through a more accurate dispersion relation. Finally, *Godin* (2014) used more realistic assumptions on the background atmospheric conditions to obtain a better estimate of the imaginary part of $\vec{k}$ and the attenuation it implies.

The scarcity of comprehensive data on thermospheric AGWs, coupled with the general lack of collocated measurements of the background horizontal winds, have made it difficult to accurately test the agreement between measurement derived wave parameters and the theoretical dispersion relation. The issue becomes a vitally important one in the case of ionospheric measurements, since AGWs are not the only possible cause for TIDs. Interesting enough, this issue is rarely discussed in the existing literature.

This section demonstrates the use of Dynasonde data for the study of the propagation parameters of thermospheric gravity waves. For this first study, we used measurements obtained with the Vertical Incidence Pulsed Ionospheric Radar (VIPIR) instrument at Wallops Island, VA, covering the whole month of October 2013. The Dynasonde analysis provides height profiles of electron density, zonal (west-east) and meridional (south-north) tilts and vertical component of line-of-sight Doppler speed of plasma contours at all bottom ionosphere heights. The tilt measurements allow for horizontal components of the plasma density gradient to be obtained, from which the horizontal wavelength of TIDs can be extracted, while the vertical wavelength can be obtained directly from the height profile. Spectral analysis of the data is able to provide amplitudes of wave harmonics. In addition to this, the station can operate on a continuous basis, allowing very long time series to be obtained.

The purpose of this chapter is to (i) demonstrate the potential of Dynasonde-capable instruments to fully diagnose the AGW spectra and its altitude variability, (ii) study all spectral characteristics of the Dynasonde data, (iii) prove that the TIDs we observe accurately follow predictions of AGW theory, and (iv) determine the statistical distribution of AGW parameters for our sample dataset from Wallops Island for October 2013. This will bring an important contribution since the method allows for the full set of AGW parameters to be determined at all bottom *F*-layer heights and Dynasonde capable instruments can operate continuously.

5.2. Temporal and Spectral Characteristics of the Dynasonde Data

The starting point are the electron density and tilt height profiles obtained at a 2-minute cadence and interpolated to a fixed height grid with a 2 km resolution. In order to illustrate the dominant AGW activity, a 10 hour sample dataset obtained on 24 October 2013 is shown in Figure 5.1. All three quantities show perturbations indicative of AGW activity with tilted wave fronts and downward phase propagation. In Figure 5.1a, the background component of the electron density distribution, with its strong dependence on the altitude, is dominant. The same perturbations are more pronounced in the case of the two tilt measurements (Figures 5.1b and 5.1c).

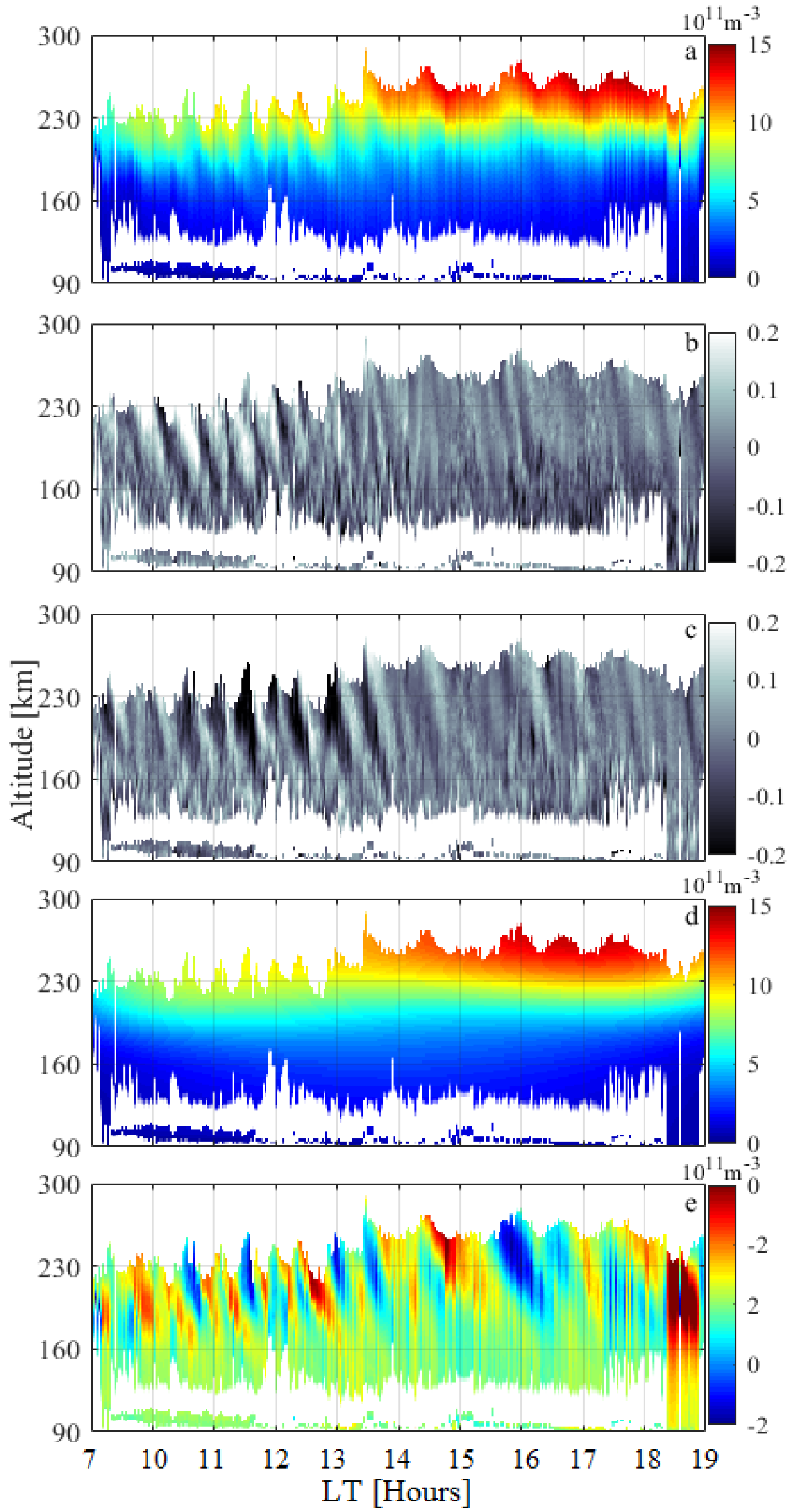

Figure 5.1. Data for Wallops Island, VA on 24 October 2013: (a) electron density, (b) zonal (west-east) tilt, (c) meridional (south-north) tilt, (d) background electron density and (e) electron density perturbation due to TIDs. Reproduced from Negrea et al. (2016b).

Since utilization of the ionospheric tilts is currently unique to the Dynasonde method, it is necessary to further discuss their properties and, in particular, why they act as a sensitive tracer for TIDs. For the purposes of data processing, one can assume that the spatio-temporal distribution of ionospheric plasma density, N_e may be represented in the vicinity of the station location as a sum of the background component $\overline{N_e}$, controlled primarily by exposure of the Earth's atmosphere to the solar flux, and the disturbed component N_e' caused by the wave activity:

$$N_e(\boldsymbol{r},t) = \overline{N_e}(\boldsymbol{r} - \hat{\boldsymbol{x}}c_E t) + N_e'(\boldsymbol{r},t), \tag{5.2}$$

where $c_E = \frac{2\pi R_E \cos(L)}{T}$ is the Earth's rotation speed at the station's latitude L, R_E is the Earth's radius, and T is the Earth's rotation period. The horizontal components of the electron density gradient caused by TIDs (which utility for AGW studies was demonstrated by *Oliver et. al*., [1994, 1995]) can be recovered from zonal and meridional tilts and the vertical component of the electron density gradient:

$$\nabla_x N_e = \frac{n_x \frac{\partial}{\partial z} N_e}{\sqrt{1-n_x^2-n_y^2}} - \frac{1}{c_E}\frac{\partial}{\partial t}\overline{N_e} \ , \tag{5.3}$$

$$\nabla_y N_e = \frac{n_y \frac{\partial}{\partial z} N_e}{\sqrt{1-n_x^2-n_y^2}} \qquad . \tag{5.4}$$

The second term in equation (5.3) accounts for effects of the zonal gradients in the background electron density distribution. This correction term is significant mainly near the solar terminator. Time series of the plasma frequency profiles $N_e(z)$ and of the two tilt components, as shown in Figure 5.1a-c, are products of autonomous Dynasonde data analysis. To distinguish between the background electron density distribution $\overline{N_e}$ and the electron density perturbations N_e', an automated detrending procedure has been implemented. Since no low-order polynomial can accurately represent the diurnal variation of $\overline{N_e}$, a two-step approach was used. A dataset of arbitrary length is divided into several subintervals, grouped into three categories: daytime, nighttime and intermediary. The division into subintervals and the differentiation between different types of subintervals is based on the properties of the data itself. During daytime and nighttime, the plasma density at a fixed altitude varies significantly less than for the 1-2 hour periods around sunrise and sunset. Also, the average plasma density is considerably higher during daytime. This behavior can be quantified using an empirical approach. For example, if the following quantities are calculated:

$$\sigma_t^2 = \frac{1}{t\prime}\sum_{i=t-\frac{\Delta t}{2}}^{t+\frac{\Delta t}{2}}(Ne_i - \overline{Ne}_t)^2 \tag{5.5}$$

$$\delta_t = \frac{10^{13}}{\Delta t\,\overline{Ne}_j}\sum_{i=t-\frac{\Delta t}{2}}^{t+\frac{\Delta t}{2}}\left(\frac{\partial}{\partial t}Ne\right)_i \tag{5.6}$$

$$\overline{Ne}_t = \frac{1}{\Delta t}\sum_{i=t-\frac{\Delta t}{2}}^{t+\frac{\Delta t}{2}}Ne_i \tag{5.7}$$

where $t \in \left(\frac{\Delta t}{2}; \Delta T - \frac{\Delta t}{2}\right)$, ΔT is the total length of the dataset and Δt is the length of the subinterval used to determine σ and δ, then the electron density at a certain altitude can be separated into subintervals, with a data point classified as either daytime or nighttime data if $\sigma_t^2 \leq 10^{11}$ and $|\delta_t| \leq 2 \cdot 10^{11}$. An example of the results of this procedure is schematically shown in Figure 5.2.

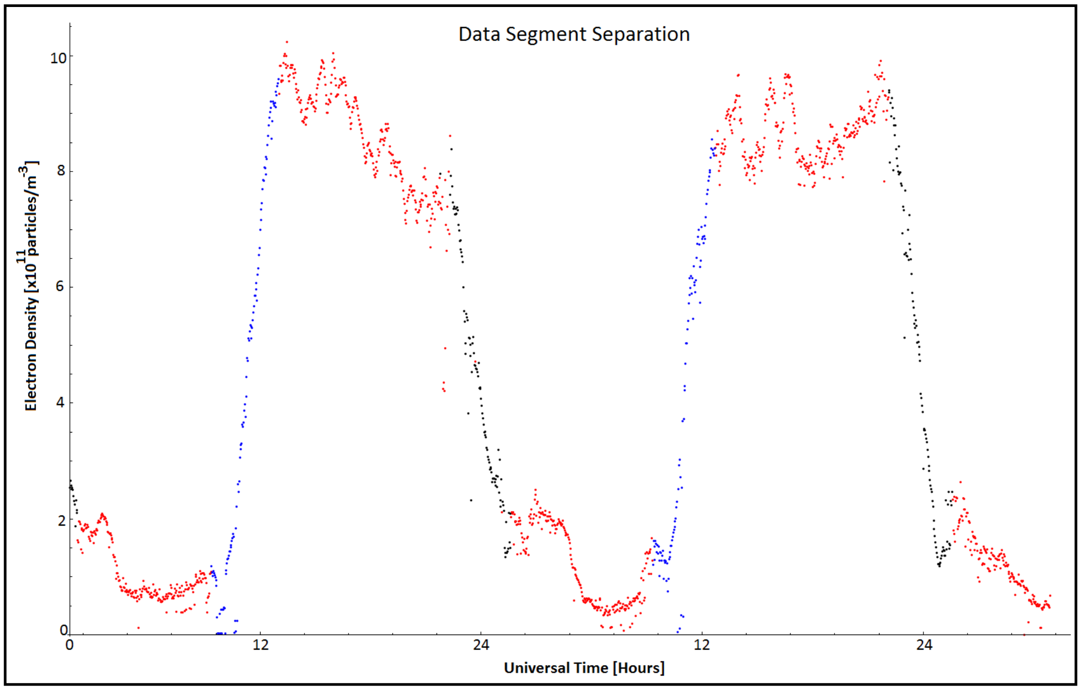

Figure 5.2. Graphical illustration of the separation of a dataset of electron density at a constant height of 200 km into several segments, with the purpose of detrending each segment separately.

As the second step of this detrending procedure, $\overline{N_e}$ is approximated by a fourth order polynomial at each constant altitude. The polynomial coefficients are determined through least square fitting for each subinterval, and the resulting time series of the background electron density is presented in Figure 1d. The extracted disturbed component is displayed in Figure 5.1e. The slant wave front structures are similar to those in the tilt time series (Figure 5.1b and 5.1c). The partial derivatives $\frac{\partial}{\partial z} N_e$ and $\frac{\partial}{\partial t} \overline{N_e}$ present in equations. (5.3) and (5.4) are obtained by a finite difference technique from the data series shown in Figures 5.1a and 5.1d.

Our processing technique is based on NeXtYZ output representing vertical profiles of various physical parameters describing the ionosphere. Altitude resolution of these profiles is high (2 km) and the data from every 2-km interval are processed independently.

This justifies a use of a plane wave model for local representation of a single TID harmonic, similar to the one introduced by equation (5.1) for local representation of an AGW harmonic:

$$N_e' = N_e'(\omega)\exp[i(\boldsymbol{k}\cdot\boldsymbol{r} - \omega t)] \; , \tag{5.8}$$

where $N_e'(\omega)$ is the magnitude of that specific harmonic, $\boldsymbol{k}$ and ω are its wavevector and angular frequency, $\boldsymbol{r}$ is the position vector, and t is the time. Function $N_e'(\omega)$ may have several local maxima corresponding to several wave packages with different carrier frequencies ω_j passing over the station at the same time. It follows from Equation (5.8) that there is a linear relationship between the spectral amplitudes of the perturbation of the electron density gradient and the perturbation of the electron density itself:

$$\boldsymbol{\nabla} N_e' = i\boldsymbol{k}N_e' \quad . \tag{5.9}$$

We have shown earlier how the time series of the electron density perturbations and the time series of the horizontal gradients related to the wave activity can be obtained from the Dynasonde data. equation (7) provides a tool for obtaining two horizontal components of the wave vector, k_x and k_y. An underlying assumption here is that there is only one wavevector $\boldsymbol{k}$ corresponding to any specific frequency ω. The technique does not allow resolving wave packages propagating at the same carrier frequency and at the same time in different directions. This is a fundamental limitation for one-point measurements and it can be overcome only if observations are performed at several locations.

In a linear approximation with relation to the wave-related perturbations, real parts of the spectral amplitudes of the tilts can be expressed using Equations (3.10) and (5.9) as:

$$n_{x,y} = \frac{k_{x,y}}{|\nabla \overline{N_e}|} N_e' \,. \tag{5.10}$$

The normalization by the magnitude of the electron density gradient,$|\nabla \overline{N_e}|$, explains the reduced sensitivity of the tilts to altitude variations in the background electron density. This feature was noted with regard to the data presented in Figures 5.1a-c.

To determine the spectral features due to AGW activity in the data, an implementation of the Lomb-Scargle method is used [*Lomb,* 1976; *Scargle,* 1982, 1986; *Press et al.,* 1989]. Both magnitude and phase of the spectral components are of interest, and they are calculated using the approach suggested by *Hocke and Kampfer* [2009]. A sliding window technique determines the time variation of the spectra, with a window length of 2 hours and a step of 2 min. The validity of individual spectra is established using the approach described in Section 4.2.

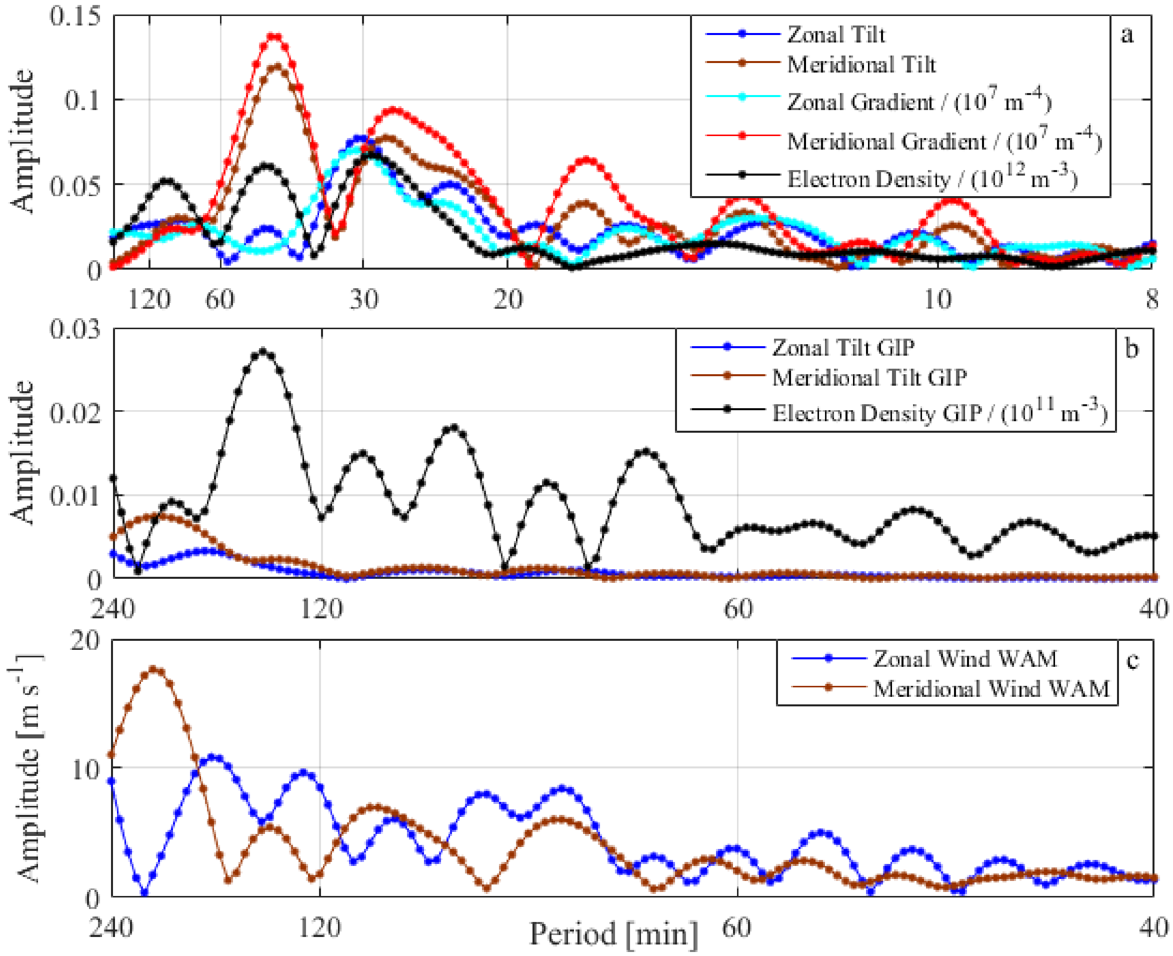

Figure 5.3. (a) Sample spectra at 200 km, for a time interval of 2 hours centered at 10:16 LT on 24 October 2013. Frequency shifts can be observed between electron density and tilt spectral features, and between zonal and meridional tilts. (b) Sample spectra of GIP electron density and synthetic tilts. (c) Sample spectra of the WAM neutral wind horizontal components. Reproduced from Negrea et al. (2016b).

It is usually the case that a superposition of several wave packages characterized by different carrier frequencies is observed. Because of this reason, spectra of variations of various ionospheric parameters have several spectral peaks of magnitudes N'_{ej} at frequencies ω_j, where index *j* enumerates the wave packages, at any particular time. Figure 5.3a shows typical examples of the spectra of electron density (N'_e), zonal ($\nabla_x N_e$) and meridional ($\nabla_y N_e$) gradient components, zonal (n_x) and meridional (n_y) tilts with about ten peaks clearly identifiable. The spectra have been obtained with the same 2-hour window, so they characterize the same wave field seen in different physical parameters. Nevertheless, there are both qualitative and quantitative differences between them. Such differences are quite expected because of two main reasons. First, gradients and tilts are vector quantities and sensitivity of their individual components to a wave package depends on its direction of propagation, while electron density variations are scalar. Second, "polarization relations" between pairs of physical quantities usually contain factors depending on the frequency (for example, in the equations (5.9) and (5.10) these are components of the wave vector $\boldsymbol{k}$) and, therefore, equations determining positions of their extrema should have different roots. The latter is the most plausible explanation for subtle frequency shifts of the order of 10^{-5} Hz between the most prominent spectral peaks in the electron density and the two gradient components, as well as between $\nabla_x N_e$ and $\nabla_y N_e$, clearly visible in Figure 5.3a. While there are precedents for measuring plasma density gradients [*Oliver et al.,* 1994], to our knowledge this is the first report of the peculiarities of fine structures in their spectra.

When analyzing results of spectral measurements one should also bear in mind a possibility of distortions caused by (i) measurement errors or errors introduced by analysis techniques, (ii) effects introduced by the thermosphere-ionosphere coupling, and (iii) nonstationarity of the wave process within the 2 hour window because of the tendency for the AGWs to propagate in packages. To explore influence of these factors, ionospheric model simulations were performed driven by representative and realistic neutral atmosphere waves. The Whole Atmosphere Model (WAM; *Akmaev et al.*, 2008; *Fuller-Rowell et al.*, 2008) is a general circulation model for the neutral atmosphere. The model has 150 layers from the ground to a top pressure level close to 600 km, and with layer thickness of a quarter scale height in the stratosphere and thermosphere. The model includes realistic dynamic forcing from the tropospheric and stratospheric waves so naturally generates a whole spectrum of resolved acoustic gravity waves, tides, and planetary waves. The horizontal resolution of 180 km and 3 minute time step allows for a wave spectrum with horizontal wavelengths exceeding about 500 km and periods longer than about 20 minutes. Molecular dissipative processes, such as viscosity, heat conduction, and diffusion, tend to damp the waves in the upper thermosphere and naturally limit the vertical wavelength. Horizontal molecular transport of momentum, heat, and constituents along pressure surfaces are also included in the simulations. Additional physical processes incorporated in the extended model domain include UV and EUV radiative heating, infrared radiative cooling with the breakdown of local thermodynamic equilibrium, ion drag, and Joule heating. As well as analyzing the neutral atmosphere, the WAM global wave fields at 3-minute temporal resolution were used to drive the global ionosphere plasmasphere model (GIP). GIP is a further development of the ionosphere-plasmasphere component of a coupled thermosphere ionosphere plasmasphere model [*Millward et al.*, 1996]. It utilizes a Magnetic Apex coordinate system [*Richmond*, 1995]

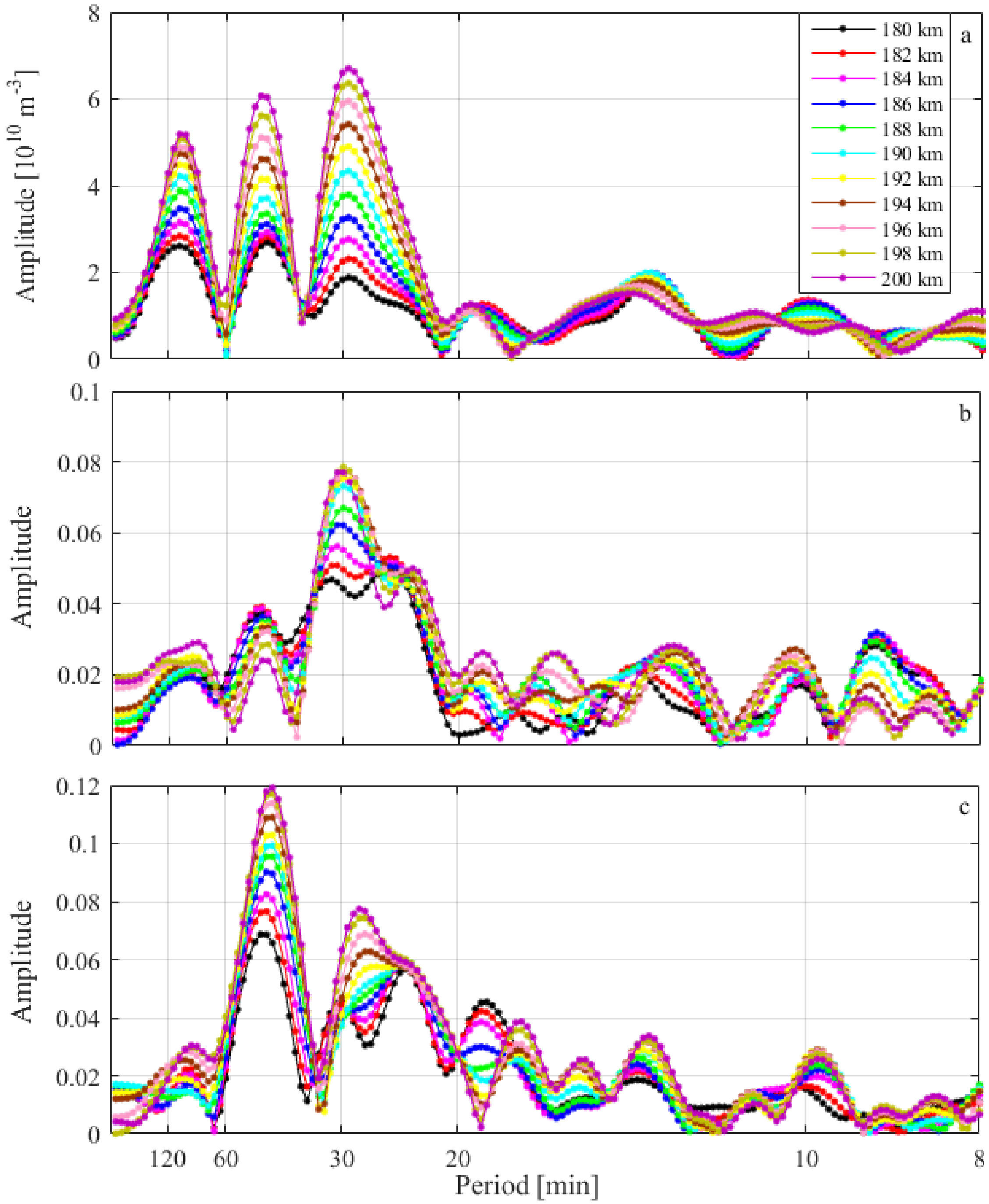

Figure 5.4. Height variation of the spectra obtained for Dynasonde data obtained at Wallops Island on 10:16 LT, 24 October 2013. (a) detrended electron density, showing the TID amplitude, (b) zonal tilt and (c) meridional tilt. Reproduced from Negrea et al. (2016b).

in which a global three-dimensional grid of magnetic field lines is created by tracing through the full International Geomagnetic Reference Field. The horizontal resolution is about 1°×4.5° in latitude-longitude. The dynamo electric field is calculated self-consistently by the electrodynamic solver of Richmond [1995] using the field-line integrated conductivities from GIP, and neutral winds, composition, and density from WAM. The electric fields, neutral winds and composition were then used in GIP in the plasma density solution along the flux tubes, as well as the zonal and meridional plasma transport calculations. Both WAM and GIP were run under constant and quiet geomagnetic and moderate solar activity conditions (F10.7=120), so that any ionospheric variability (e.g., TIDs), including changes in the longitudinal structure from one day to the next, is entirely forced by the wave field propagating from below. Within the resolution limitation of WAM and GIP, the characteristic neutral waves and resultant TIDs should be reasonable consistent with the wave fields observed by the Dynasonde.

The GIP electron density at the grid points corresponding to the immediate vicinity of Wallops Island are used to calculate synthetic tilts in accordance with equation (3.10). Figure 5.3b shows spectra of electron density and zonal and meridional tilts derived from the GIP results. Similarly to Figure 2a, frequency shifts can be observed between spectra features in electron density and the tilts, as well as between the two tilt components. Simulation results strongly suggest that the frequency shifts among these parameters could be physically meaningful and are not an artifact due to data processing or measurement errors.

An analysis of the WAM neutral wind spectra (Figure 5.3c) diminishes point (ii) above as there are clear frequency shifts between the zonal and meridional wind components, similar to those observed between the zonal and meridional tilts. Since the GIP simulation used WAM wind fields as an input, it is a reasonable assumption that the frequency shifts observed in GIP results (Figure 5.3b) are linked to the frequency shifts in the WAM results (Figure 5.3c), and not by any anisotropies introduced by the geomagnetic field via the thermosphere-ionosphere coupling.

Nonstationarity of the wave process (propagation in packages) or of the atmosphere itself within the 2-hour window cannot be excluded as factors influencing the spectrum shape. Since the spectra are functions of the ground frequency, the variation of the $\boldsymbol{k} \cdot \boldsymbol{u}$ product can be sufficiently large to produce observable effects. Since ray paths are generally curved, the change in the propagation direction, coupled with changes in the neutral wind of 1-10 m/s can account for Doppler-like frequency shifts.

Figure 5.4 shows an example of the altitude variation of the electron density (a) and tilt spectral magnitude (b and c) between 180 and 200 km. The TID amplitude (Figure 5.4a) shows a monotonic amplitude increase with height for periods higher than 18 min. The increase is not exponential and the amplitude difference between 180 and 200 km is smaller for higher frequencies, possibly due to increased attenuation and/or wave ducting. The tilt magnitudes have a much more complex variation with height, as they depend not just on the underlying AGW amplitude but also its wavelength and propagation direction. At frequencies where the TID amplitude is large, the difference in magnitude between the zonal and meridional tilt spectra is indicative of the wave's propagation direction in the horizontal plane.

5.3. Wave parameters

To fully characterize the TIDs observed at a certain location, in addition to the amplitude shown in Figure 5.4, all three components of the wavevector (zonal, meridional and vertical) are required, at all frequencies, ideally over a wide altitude range. Equation (5.9) shows how the horizontal wavevector components can be determined from the spectra of the electron density and the electron density gradient. An estimate of the vertical wavevector component can be obtained experimentally from the height variation of the phase:

$$k_{zj} = \frac{\partial \Phi_j}{\partial z} \quad , \tag{5.11}$$

where Φ_j is the phase of the wave package j determined with a special implementation of the Lomb-Scargle algorithm [*Hocke and Kampfer*, 2009] applied independently to data series from all available 2-km altitude intervals. The use of equation (5.11) means neglecting the vertical gradient of the Berry phase compared to k_z, what is usually a reasonable approximation [*Godin*, 2015b]. It is also implied that the wave is in its propagation zone, that it is not an evanescent one.

A natural question at this point is weather to use the phase of N_e' , $\nabla_x N_e$ or $\nabla_y N_e$. It is expected that values for k_z obtained using either electron density or the electron density gradient components should be similar. Equation (5.9) requires that there should only be a $\pm\frac{\pi}{2}$ phase difference between N_e' and both $\nabla_x N_e$ and $\nabla_y N_e$. Figure 5.5 shows the phase height profile for the wave package with central frequency 0.55 mHz (30 min period) for the three quantities and the time window centered at 10:16 LT. The phase of the electron density is also displayed with a $\pm\frac{\pi}{2}$ phase shift for comparison. The behavior is very close to what is expected theoretically. Figure 5.5 also shows that the choice of parameter to use in calculating k_z may not be obvious since the behavior of all three curves can be similar. However, N_e' will be preferred from now on, as it is obtained using a single data analysis product, the electron density, while the electron density gradient depends on both components of the tilt and the electron density.

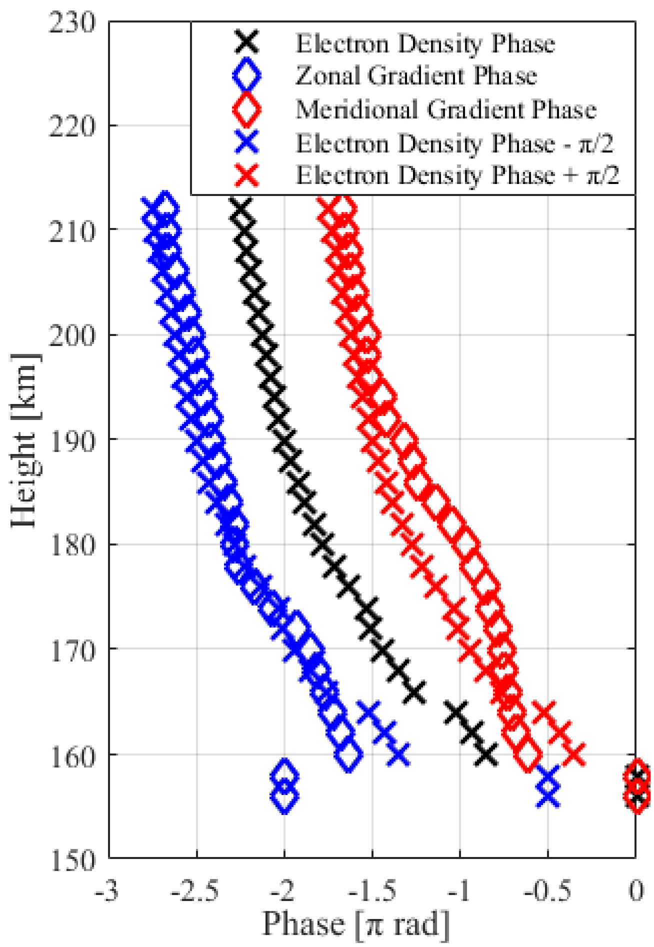

Figure 5.5. Height profile of the phase of the detrended electron density and the two horizontal components of the electron density gradient at a frequency of 0.55 mHz (30 min). The electron density phase is also shown with a $+\frac{\pi}{2}$ and $-\frac{\pi}{2}$ offset, highlighting the agreement between our data and the behavior of the phase theoretically predicted by equation (5.9). Reproduced from Negrea et al. (2016b).

Dynasonde analysis provides parameters of ionized component, which means that deriving parameters of neutral component requires additional steps and implies that results obtained without such extension describe TIDs that may not be always caused by acoustic gravity waves. For a wave with known frequency and wavevector components, it is theoretically possible to verify the agreement between measurements and the theoretical AGW dispersion relation

$$k_z = \sqrt{\left(k_x^2 + k_y^2\right)\left(\frac{N_0^2}{\omega_0^2} - 1\right) + \frac{\omega_0^2}{C_0^2} + \frac{1}{4H^2}} \tag{5.12}$$

where $N_0^2 = g\left(\frac{1}{H} - \frac{g}{C_0^2}\right)$, c_0 is the sound speed, H is the scale height, g is the gravitational acceleration, $\omega_0 = \omega - \boldsymbol{k} \cdot \boldsymbol{u} = \omega - k_x u_x - k_y u_y$, and u_x and u_y are the zonal and meridional components of the background neutral wind [*Godin*, 2015b]. In practice, thermospheric AGWs can have a considerable imaginary component of k_z, both because there are large spatial regions where they may exist as evanescent waves and because of the viscous attenuation [*Godin,* 2014]. If a wave is in the shadow zone (this happens when the expression under radical sign in Equation (5.12) is negative), it is still observable, but Equation (5.11) is not valid: vertical gradient of the phase determines a different physical quantity. In our current analysis, we will assume that the observed wave packages are in propagation mode.

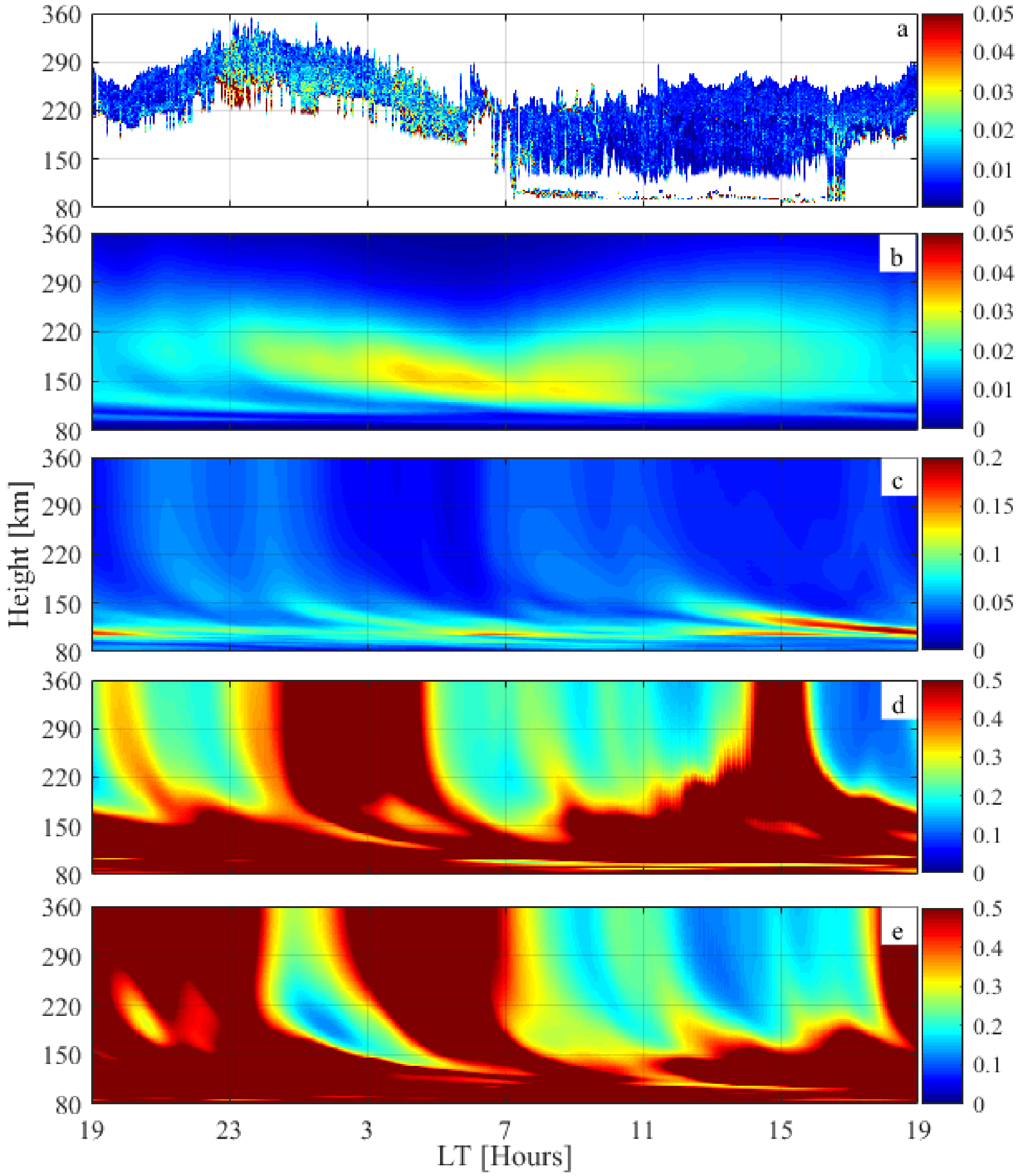

Figure 5.6. (a) Relative error of the Dynasonde electron density and the estimated uncertainty of the WAM (b) mean molecular mass, (c) neutral temperature, (d) zonal and (e) meridional neutral wind. Reproduced from Negrea et al. (2016b).

Theoretical estimate of k_z requires an accurate knowledge of the background atmospheric parameters. However, data on the neutral density, temperature and winds are rarely available at thermospheric heights. One alternative is the use of results from numerical models, which can be accurate in a climatological sense. The uncertainty associated with model results can be difficult to estimate in the absence of comprehensive validation studies (*Negrea et al.*, 2012), but errors between 10 – 20% are common (*Fedrizzi et al.*, 2012). In order to compare the propagation parameters we obtain with the theoretical dispersion relation, a month long WAM simulation was performed, for conditions corresponding to the month of October 2013, calculating neutral temperature, density, chemical composition and both the zonal and meridional wind components. The background value for each parameter is assumed to be equal to the median of the whole 31-day interval, determined independently for each altitude and local time. The associated uncertainty is estimated by the corresponding standard deviation. Figure 5.6a shows the relative error for the Dynasonde-derived electron density for a 24-hour long interval on 24 October 2013. The values are generally much smaller than 1%, while a minority of data points have relative errors of at most 5%. Figures 5.6b-e show the estimated relative uncertainty for the mean molecular mass, neutral temperature, zonal wind and meridional wind derived from WAM, all of which are higher than the uncertainty in the data. It is necessary to take into account the uncertainty associated with k_z, σ_{k_z}, due to the variability in the mean molecular mass, $\sigma_{\bar{M}}$, neutral temperature, σ_T, zonal wind, σ_{u_x} and meridional wind σ_{u_y}.

The model-derived vertical wavevector component obtained using Equation (5.12) depends on the following parameters:

Scale height

$$H = \frac{k_B}{g}\frac{T}{\bar{M}} \tag{5.13}$$

sound speed

$$C_0^2 = \gamma k_B \frac{T}{\bar{M}} \tag{5.14}$$

buoyancy frequency

$$N_0^2 = g\left(\frac{1}{H} - \frac{g}{C_0^2}\right) \tag{5.15}$$

intrinsic wave frequency

$$\omega_0 = \omega - \vec{k} \cdot \vec{u} = \omega - k_x u_x - k_y u_y \tag{5.16}$$

where g is the gravitational acceleration, T is the neutral gas temperature, γ is the adiabatic index, k_B is the Boltzmann's constant, u_x and u_y are the zonal and meridional wind components, $\bar{M}$ is the mean molecular mass, ω is the ground-based frequency.

We assume that the set of parameters $[\bar{M}, T, u_x, u_y]$ is characterized by diagonal covariance matrix. The uncertainty associated with the model-derived vertical wavevector component is then:

$$\sigma_{k_z}{}^2 = \left(\frac{\partial k_z}{\partial \bar{M}}\right)^2 \sigma_{\bar{M}}{}^2 + \left(\frac{\partial k_z}{\partial T}\right)^2 \sigma_T{}^2 + \left(\frac{\partial k_z}{\partial u_x}\right)^2 \sigma_{u_x}{}^2 + \left(\frac{\partial k_z}{\partial u_y}\right)^2 \sigma_{u_y}{}^2 \tag{5.17}$$

Using equation (5.12), it is straightforward to calculate the derivatives in equation (5.17):

$$\frac{\partial k_z}{\partial \bar{M}} = \frac{1}{2\bar{M}k_z}\left[\frac{1}{2H^2} + \frac{N_0^2}{\omega_0^2}\left(k_x^2 + k_y^2\right) + \frac{\omega_0^2}{C_0^2}\right] \tag{5.18}$$

$$\frac{\partial k_z}{\partial T} = \frac{-1}{2k_z}\left[\frac{1}{2H^2} - \frac{N_0^2}{\omega_0^2}\left(k_x^2 + k_y^2\right) - \frac{\omega_0^2}{C_0^2}\right] \tag{5.19}$$

$$\frac{\partial k_z}{\partial u_x} = \frac{-k_x}{2k_z}\frac{1}{C_0^2\omega_0^3}\left[-g^2(\gamma - 1)\left(k_x^2 + k_y^2\right) + \omega_0^4\right] \tag{5.20}$$

$$\frac{\partial k_z}{\partial u_y} = \frac{-k_y}{2k_z}\frac{1}{C_0^2\omega_0^3}\left[-g^2(\gamma - 1)\left(k_x^2 + k_y^2\right) + \omega_0^4\right] \tag{5.21}$$

Frequency (mHz)	**0.153**	**0.348**	**0.55**
Period (min)	**109**	**48**	**30**
λ_h **(km)**	**1025**	**335**	**368**
λ_z**(km)**	**155**	**112**	**209**
θ **(deg , direction)**	**102 (East)**	**185 (South)**	**134 (South - East)**
v_h**(m/s)**	**277**	**93**	**199**

Table 5.1. "Detailed propagation characteristics of the three dominant wave harmonics highlighted in Figures 5.7 and 5.8: frequency, period, horizontal (λ_h) and vertical (λ_z) wavelength, azimuth (propagation direction, θ) and horizontal phase speed (v_h)." Reproduced from Negrea et al. (2016b).

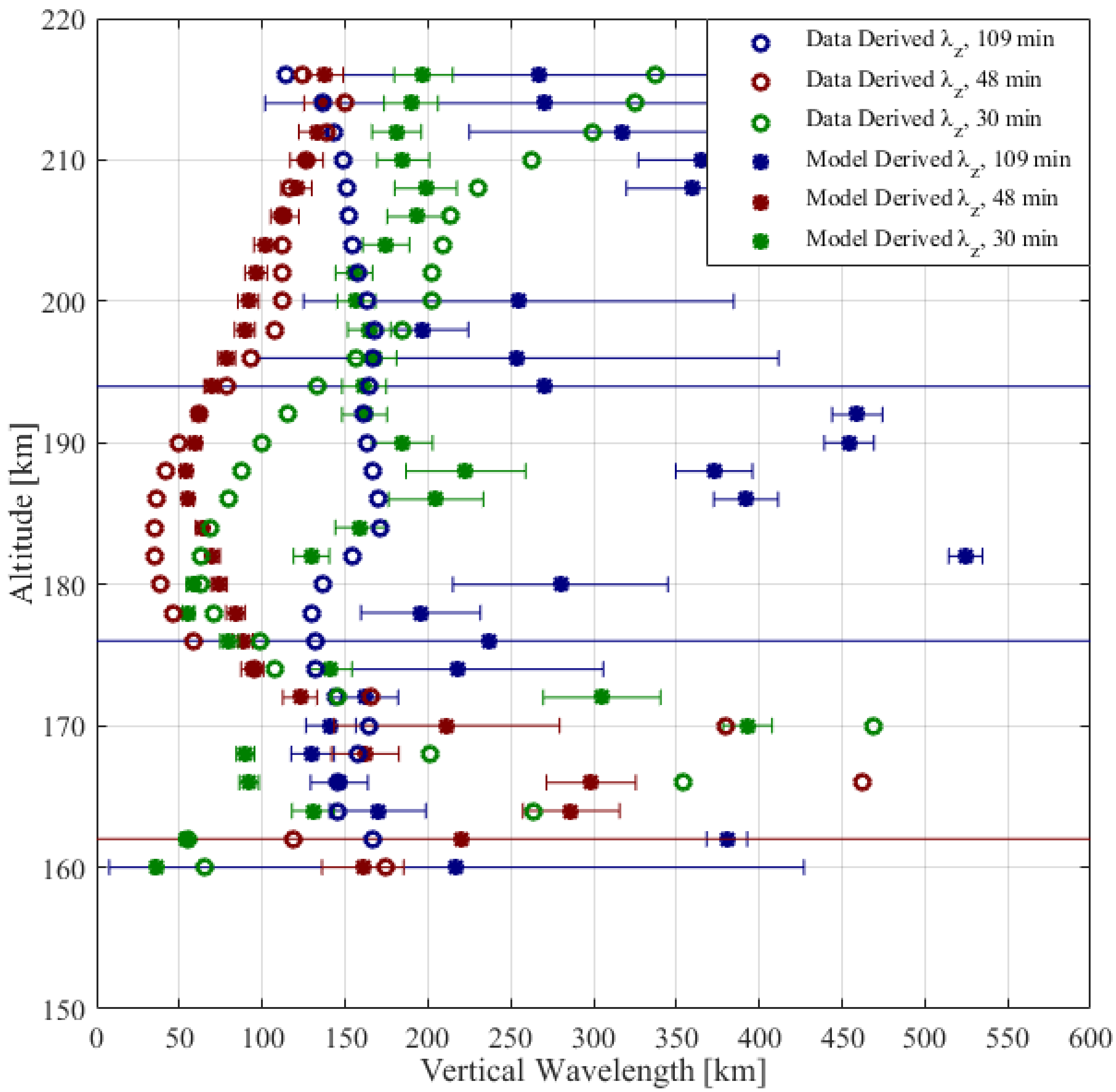

Figure 5.7. Comparison between the vertical wavelength obtained directly from the Dynasonde data with equation (5.11) and the model derived value obtained with equation (5.12), for the spectral peaks at 0.15, 0.33 and 0.55 mHz (109, 48 and 30 min, respectively) for the altitude range 150-220 km and the 2 hour time interval centered around 10:16 LT 24 October 2013. Reproduced from Negrea et al. (2016b).

For the three frequencies associated with dominant spectral peaks in Figure 5.4a (0.15, 0.33 and 0.55 mHz, or 109, 48 and 30 min, respectively), we determine k_x and k_y using Equation (5.9) and k_z using Equation (5.11). The characteristics of all three TIDs are listed in Table 5.1. Theoretical values for k_z are calculated using equation (5.12) with the uncertainties given by equations (5.17) – (5.21). A first comparison of the vertical wavelength ($\lambda_z = \left|\frac{2\pi}{k_z}\right|$) with respect to height is shown in Figure 5.7, covering the altitude interval 150–220 km. The agreement is good at 0.33 mHz (50 min) and reasonable at 0.55 mHz (30 min). Such a test of the agreement between data and the AGW dispersion relation helps to conclude that a TID is caused by an acoustic gravity wave. This test is successful for at least a part of the observed TID spectrum on 24 October 2013 over Wallops Island. Since the level of agreement seems to depend on frequency, a second comparison is performed with respect to frequency at 200 km altitude at 10:16 LT. Figure 5.8 shows qualitative agreement between the two sets of values for $\lambda_z$between 0.32 (52 min) and 0.8 mHz (21 min). Between 0.32 and 0.53 mHz there is a complete agreement within the calculated uncertainties. Between 0.53 (52 min period) and 0.8 mHz (21 min period) the experimental and theoretical values show the same trend, with some discrepancy in the case of extreme values. These may be due to the limitations in both Equation (5.12) and in the model. For frequencies below 0.32 mHz and above 0.8 mHz, the test does not provide a definitive answer about the nature of the waves observed. This may be related to limitations of the Equation (5.11) noted above. This is also reflected in the very large error bars associated with some of these values. Even partial, success of the test is remarkable. It suggests that the differences between the experimental and the theoretical values, where these are observed, are most likely due to deviations of the real atmospheric parameters from the median model values. Results of this kind may evolve into a potential measurement technique.

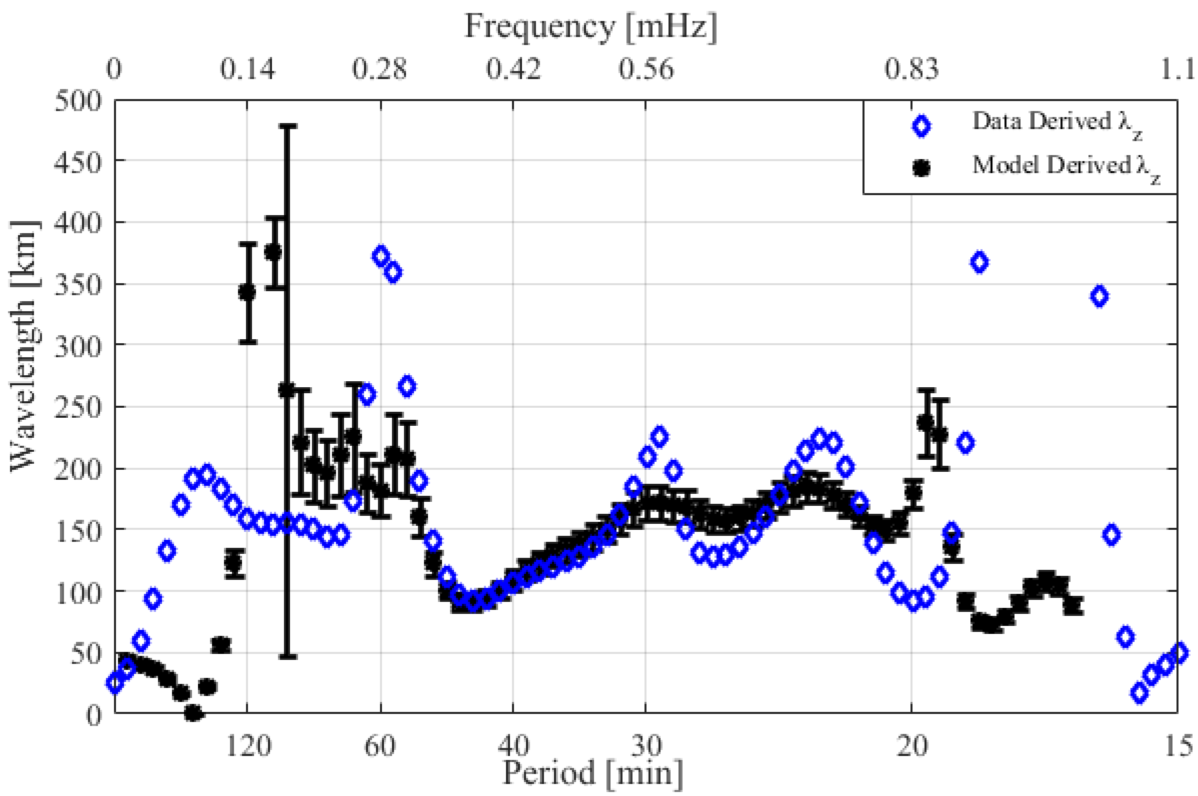

Figure 5.8. Same as Figure 5.7, but for the fixed altitude of 200 km and the frequency interval below 1 mHz. Reproduced from Negrea et al. (2016b).

The Dynasonde technique allows for the determination of all three wavevector components characterizing TIDs. This is accomplished using one of the normal operating modes of the station, without the need for a dedicated campaign. Due to this fact, large datasets can be obtained, allowing for the study of the variability in TID activity, on scales from several hours to months, or more. This is not a feature unique to Dynasonde instruments. However, the combination of both extensive temporal coverage and broad altitude range is currently unique. Electron density and tilt height profiles usually cover more than 100 km. The limitations of the technique are the inability to observe the “valley” between the ionospheric *E* and *F* layers, as well as the inability of ground based HF radars to obtain data covering the topside ionosphere.

A sample dataset covering the entire month of October 2013 is analyzed in this section. A sliding 2-hour window is used at each altitude with a step of 2 min. The same Lomb-Scargle implementation as before is used to analyze spectral characteristics of the detrended electron density and the two horizontal components of the electron density gradient. $k_{x,y}$ are calculated using Eequation (5.9) and k_z is calculated using Equation (5.11). First filter is applied by discarding any results for which there is a discrepancy of more than 4% between the integral of the Power Spectral Density and the time domain variance of either the zonal or the meridional tilts. This assures that results obtained at different altitudes will be comparable regardless of the specifics of the data sampling (*Negrea and Zabotin,* 2016). Second filtering algorithm first determines the median spectral amplitude for all local times, altitudes and frequencies and then discards all values less than that.

An approach often used in the existing literature is to define a TID using a single prominent spectral peak characterized by a discrete, not necessarily fixed, frequency, active over a certain time interval. We believe this is problematic as TIDs usually produce multiple spectral features with varying bandwidths and duration. We are not interested in the statistical distribution of AGW or TID "events", but rather the statistical characteristics of the TID activity as a whole. To accomplish this, all remaining valid data points are taken into account. Due to the natural ionospheric variability, results characterizing the daytime ionosphere are mostly obtained for the altitude range 140-260 km. By contrast, results characterizing the nighttime ionosphere are obtained mostly for the altitude range 230-320 km. To avoid a confusion between the diurnal variability and the altitude variation of the statistical distribution of TID parameters, we analyze the daytime and nighttime results separately, where for each day, "daytime" is defined as the time interval between local sunrise and sunset and "nighttime" as the time interval between local sunset and sunrise.

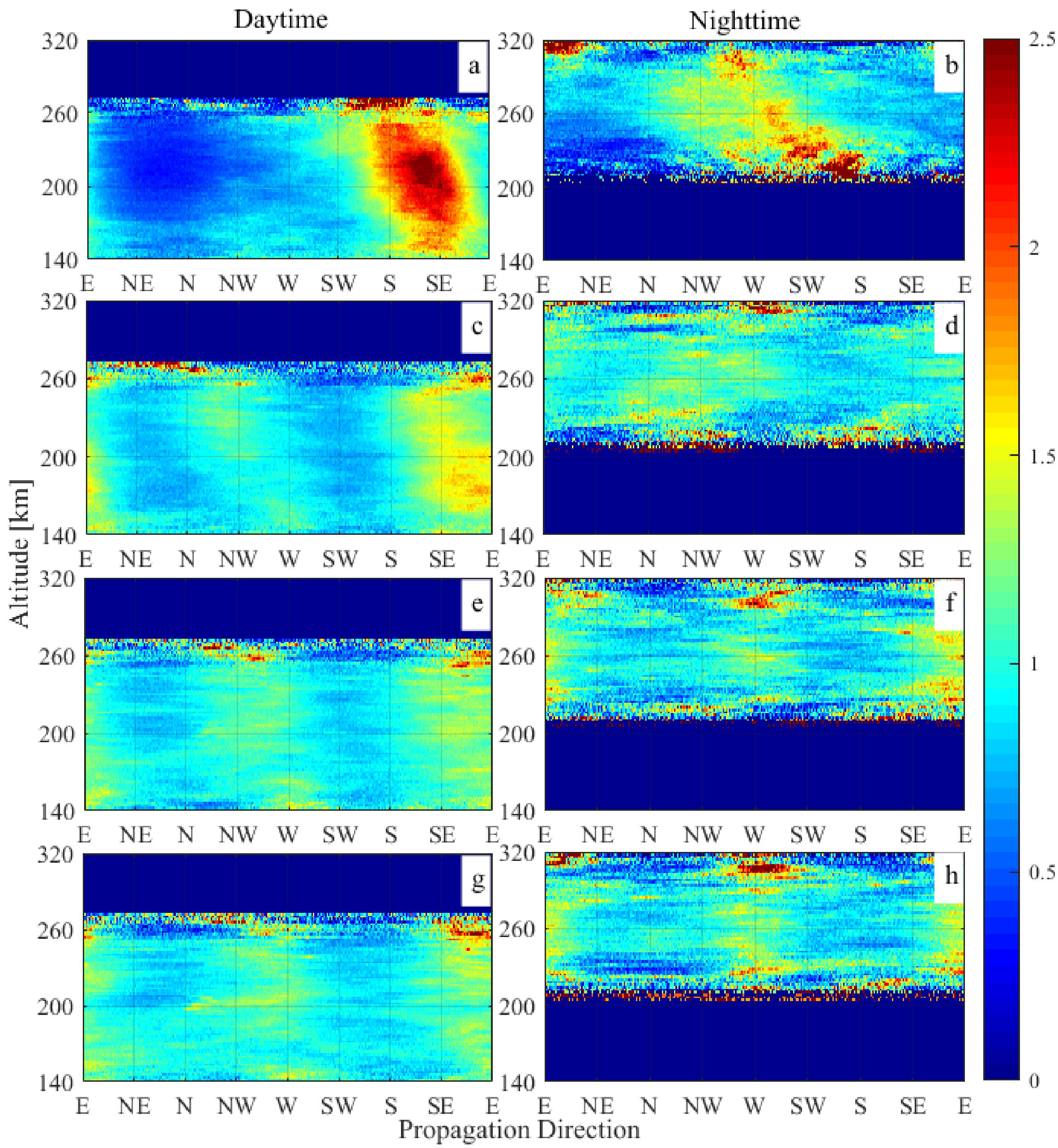

Figure 5.9. The statistical distribution of the horizontal propagation direction of observed TIDs as a function of altitude for the frequency bandwidth (a) below 1 mHz, (b) 1-2 mHz, (c) 2-3 mHz and (d) 3-4 mHz. The results at each altitude are normalized by the number of data points corresponding to omnidirectional propagation. The discontinuity at 250 km is explained by the discrepancy between the daytime and nighttime ionosphere. Reproduced from Negrea et al. (2016b).

First, the azimuth associated with TID propagation is analyzed:

$$\theta = \operatorname{atan}\frac{k_y}{k_x} \tag{5.22}$$

In Figure 5.9, the distribution at each altitude is normalized by the number of data points expected within one bin in the case of omnidirectional propagation. The results show a strong dependence on frequency band (Figure 5.9a-h). At frequencies below 1 mHz (periods larger than 17 min), a pronounced anisotropy is observed during daytime (Figure 5.9a), with the dominant wave population propagating south, south-east. Based on the results shown in Figures 5.7 and 5.8, it is reasonable to assume that acoustic gravity waves are the likely cause for these TIDs. There is a significant difference between the daytime (Figure 5.9a) and nighttime (Figure 5.9b) results. The predominant propagation direction switches towards the western direction, with an additional, associated decrease in the degree of anisotropy. It is difficult to determine from the data alone if 1) this transition is gradual and 2) if it is due to the change in local time or due to the change in altitude. At frequencies above 1 mHz (Figures 5.9c-h), we observe a slight anisotropy, with two small TID populations propagating east and west, respectively, both during daytime (Figures 5.9c, e and g) and nighttime (Figures 5.9d, f and h). More analysis is necessary to establish if these are indeed caused by gravity waves or not. In addition to the fact that the observed anisotropy is small, the total number of data points decreases both with frequency and altitude (Figure 5.10).

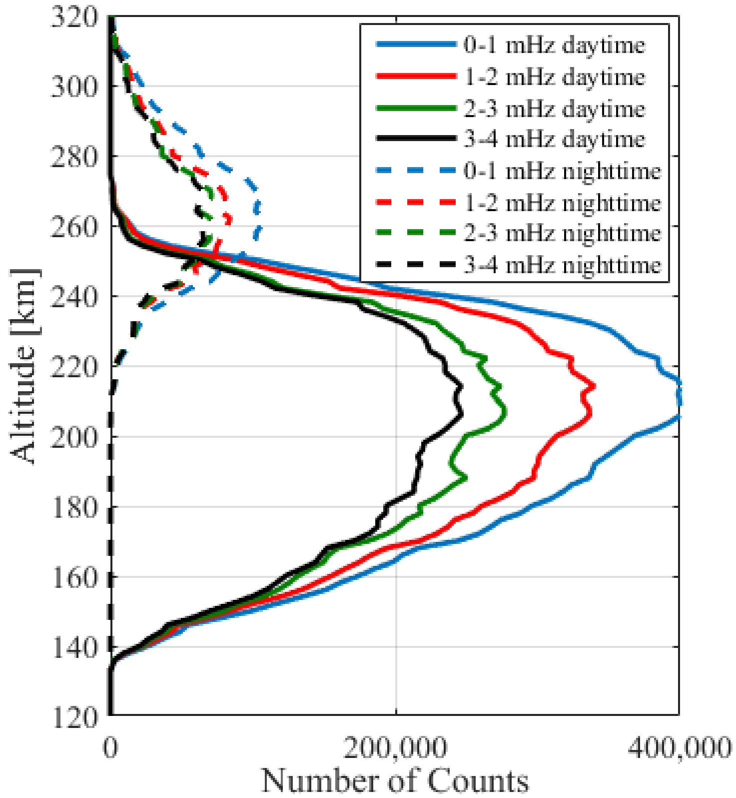

Figure 5.10. Total number of counts as a function of altitude and time of day for the four bandwidths (0-1 mHz, 1-2 mHz, 2-3 mHz and 3-4 mHz) considered in Figure 5.9, with the solid line curves for daytime data and the dashed line curves for nighttime. Reproduced from Negrea et al. (2016b).

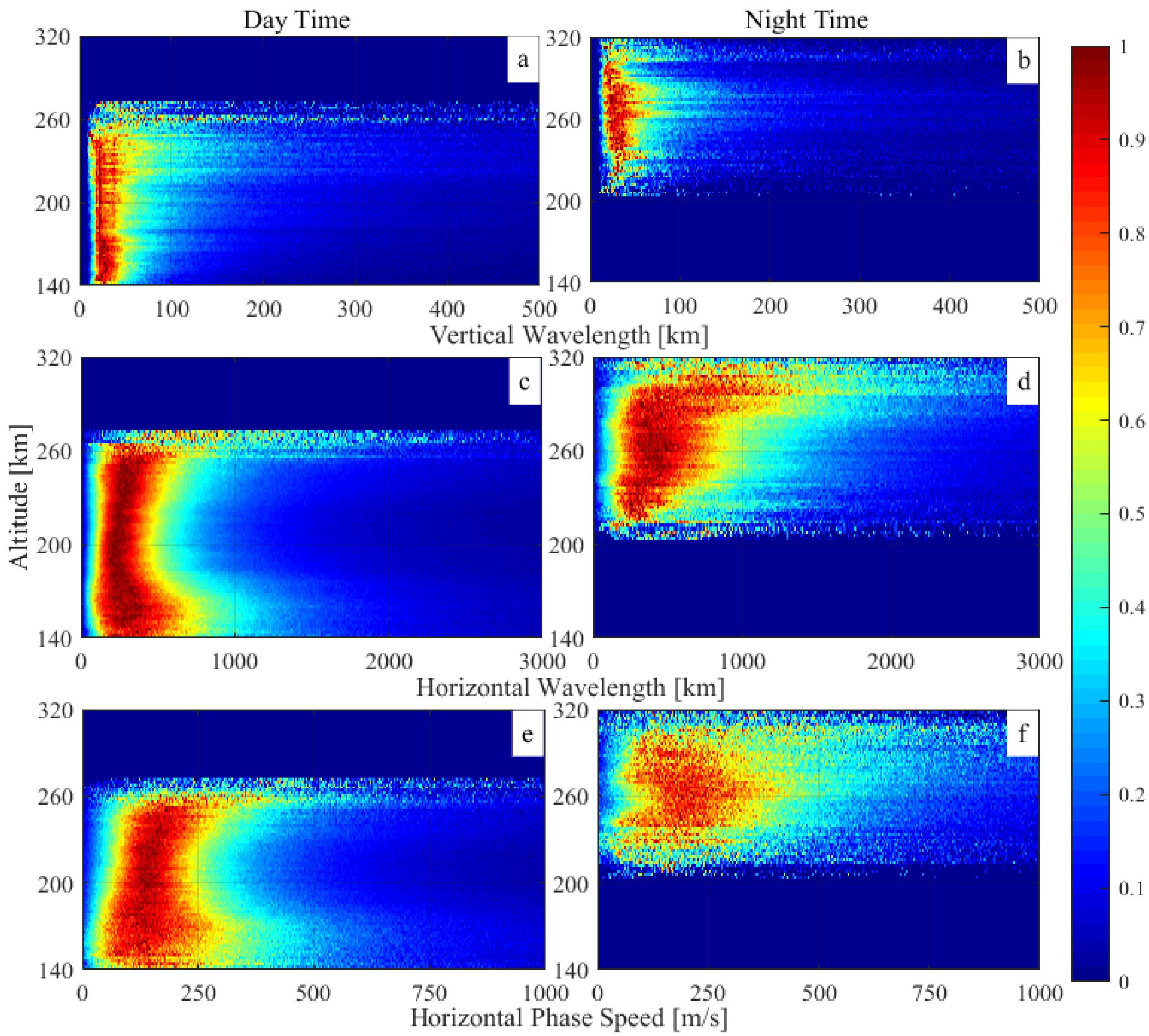

Figure 5.11. Statistical distribution of the TID (a) vertical wavelength, (b) horizontal wavelength and (c) horizontal phase speed. The results at each altitude are normalized by the maximum value at that altitude. Reproduced from Negrea et al. (2016b).

In addition to the propagation direction, the horizontal ($\lambda_h = \frac{2\pi}{\sqrt{k_x^2+k_y^2}}$) and vertical ($\lambda_z = \left|\frac{2\pi}{k_z}\right|$) wavelengths and the horizontal phase speed ($v_h = \frac{\omega}{\sqrt{k_x^2+k_y^2}}$) are of interest. For the current study their distribution is determined taking into account only TIDs with frequencies below 1 mHz, separately for daytime and nighttime measurements. For each altitude and parameter, the result is normalized by the maximum value for the respective time interval. The total number of counts depends strongly on altitude and local time, as seen in Figure 5.10. Most of the valid results in this case are between 150 and 250 km altitude during daytime, and between 240 and 270 km during nighttime, with the ratio of the daytime and nighttime maximum number of counts being approximately four to one. Figures 5.11c,e show daytime distributions dominated by a strong peak that widens and dissipates below 150 and above 250 km. The nighttime results (Figures 5.11d, f) show a considerably wider peak between 240 and 280 km. By contrast, the peak of the distribution of the vertical wavelength is wider in the altitude range 150–250 km during daytime (Figure 5.11a) and between 240 and 280 km during nighttime (Figure 5.11b), with most values about 30 km. The peak of the horizontal wavelength distribution is between 250 and 350 km during daytime and between 400 and 500 km during nighttime. Finally, the maximum of the phase speed distribution occurs between 100–180 m/s for daytime TIDs and between 180 and 220 m/s for nighttime TIDs.

It is interesting to note that the TIDs listed in Table 5.1 do not seem to be a part of the main TID population. This indicates that the AGWs with the highest amplitude for that specific time interval were not the source of the most numerous population of TIDs. The discussion in Section 4 was focused on those spectral features clearly caused by Gravity-Waves, which we verify by rigorously testing the agreement with the gravity wave dispersion relation (Equation 5.12). In Figures 5.9 - 5.11, we present the statistical distribution of TID propagation parameters, in accordance with the filtering and selection criteria detailed above.

The obtained statistical distribution of the horizontal wavelength is in general agreement with previous results obtained using other techniques (SuperDARN, GPS, airglow imagers), with the added advantage of describing the dependence with altitude of the statistical distribution. Also, the statistical distribution of the vertical wavelength is studied. When comparing the results presented here with other existing studies, it is necessary to take into account that such studies usually describe the statistics of TID events, where and event can be manifest for varying periods of time. Also, the bandwidth covered by specific TIDs is not taken into account. By contrast, Figures 5.9 and 5.11 describe the statistical distribution of TID activity. However, of these two differences in determining the statistical distributions, the bandwidth of individual TIDs was found not to change the results. Taking into account only the propagation parameters associated with spectral peaks does not change the overall shape of the statistical distribution shown in Figures 5.9 and 5.11, but only the total number of counts in Figure 5.10.

To summarize, the full set of propagation parameters is determined: the horizontal components of the wavevector using the electron density and the horizontal components of the electron density gradient and the vertical component of the wavevector using the variation of the wave phase with altitude. The agreement between these results and the theoretical gravity wave dispersion relation is tested. In the altitude range 160-220 km, and for the frequency interval 0.32 – 0.8 mHz, the agreement is remarkable, taking into account the uncertainty associated with the parameters of the background thermosphere. Finally, the statistical distribution of the propagation parameters is analyzed. A dominant population of TIDs is identified, with frequencies below 1 mHz and a northwest to southeast propagation direction. For this frequency band, we analyze the altitude variation of the statistical distribution of the vertical wavelength, the horizontal wavelength and horizontal phase speed. The height profiles of the electron density and ionospheric tilts allow for the full set of AGW parameters to be determined for the bottom-side ionosphere. By verifying the agreement of our results with the theoretical dispersion relation, we can identify the parts of the TID spectrum definitely caused by gravity waves.

CHAPTER 6

GRAVITY WAVE MOMENTUM FLUX

6.2. Introduction

The immediate impact of AGWs on the thermosphere-ionosphere consists of perturbations in the neutral atmosphere parameters as well as associated TIDs. These perturbations, as discussed in previous chapters, are extremely important and can be observed directly in the ionospheric data provided by either Dynasonde instruments or other remote-sensing techniques. In addition to this, the energy and momentum these waves carry can have a considerable impact on the state of the background system. As atmospheric conditions cause wave dissipation, the momentum carried is dumped into the background flow. The overall effect due to this extra momentum-source is already known to be significant in the middle atmosphere (stratosphere and mesosphere, 20-80 km altitude). This acts as an additional forcing with a complex temporal, geographical and altitude variability. Since a significant spectrum of waves exists in the thermosphere, similar considerations are likely to apply regarding the impact of AGWs at thermospheric altitudes.

Early work on thermospheric gravity waves showed that different attenuation mechanisms dominate above 150 km. *Pitteway and Hines*, (1963) discussed the likely role of viscous damping. *Francis* (1973) considered several attenuation mechanism, showing the importance of temperature variations compared to ion drag (ion-neutral collisions). More recently, *Vadas and Fritts* (2005) derived a dispersion relation that considers wave damping. *Liu et al.* (2013) performed a study involving two-dimensional numerical simulations. The dissipation of small amplitude, small vertical wavelength (below 50 km) waves was confirmed to follow predictions by *Vadas and Fritts* (2005) for a realistic atmosphere. Finally, *Godin* (2014) showed how an asymptotic approach that does not assume plane-wave solutions leads to different values for the attenuation of acoustic-gravity waves.

The impact on the background system due to attenuating waves is described using the vertical flux of the horizontal pseudomomentum (*Fritts and Alexander,* 2003):

$$\boldsymbol{F} = \left(F_x, F_y\right) = \bar{\rho}\left(\overline{u_x' \, u_z'}, \overline{u_y' \, u_z'}\right) \tag{6.1}$$

where F_x and F_y are the zonal and meridional components of the horinzontal components of $\boldsymbol{F}$, u_x', u_y' and u_z' are the zonal, meridional and vertical neutral wind perturbation due to a specific gravity wave and $\bar{\rho}$ is the background neutral mass density. The overhead bar in the products $\overline{u_x' \, u_z'}$ and $\overline{u_y' \, u_z'}$ denote time averaging over a period comparable to the wave period. Note that u_x', u_y', u_z' and $\boldsymbol{F}$ are time, altitude and frequency dependent. The variation of $\boldsymbol{F}$ can be used to determine the acceleration induced by dissipating AWGs on the background system:

$$(X, Y) = -\frac{1}{\bar{\rho}}\frac{d}{dz}\boldsymbol{F} = -\frac{1}{\bar{\rho}}\frac{d}{dz}\left[\bar{\rho}\left(\overline{u_x' \, u_z'}, \overline{u_y' \, u_z'}\right)\right] \tag{6.2}$$

where (X, Y) effectively corresponds to an extra acceleration of the background system.

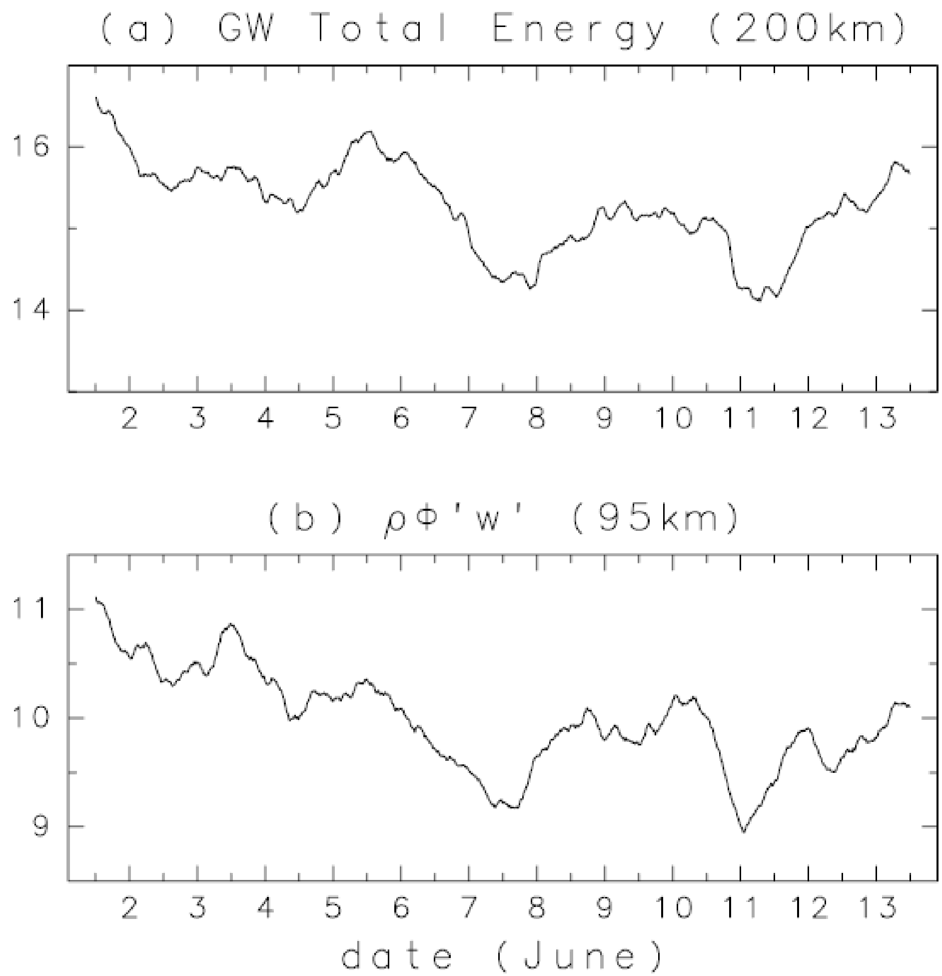

Figure 6.1. "(a) Time distribution of zonal mean total energy for the short-period gravity waves at 200 km height averaged from 5ºN to 5ºS. Units are 10^{-7} kg m^{-1} s^{-2}. (b) Time distribution of zonal mean vertical flux of energy for the short-period gravity waves at 95 km height averaged from 5ºN to 5ºS. Units are 10^{-5} kg m^{-1} s^{-1}." Reproduced from Miyoshi and Fujiwara (2008).

The global impact on the thermosphere-ionosphere due to AGW dissipation has only been roughly estimated. General Circulation Models (GCMs) can realistically account for waves with wavelengths (both vertical and horizontal) significantly larger than the spacing between the model grid points. Using a GCM with an equivalent horizontal grid spacing of 1.4º latitude and 1.4º longitude, and a 0.4 scale height vertical resolution, *Miyoshi and Fujiwara* (2008) obtained an estimate of the impact of large-scale GWs over a wide range of mesospheric and thermospheric altitudes (Figure 6.1). The authors also conclude that higher resolutions would be necessary to resolve waves with periods less than 1 hour. Currently, no GCM can self-consistently model the entire wave spectrum in the thermosphere. Based on results discussed in Chapters 4 and 5 (e.g., Figures 4.12, 5.4 and 5.11), as well as previous studies (e.g., *Hernandes-Pajares et al.*, 2006; *Frissell et al.*, 2016), the dominant part of the AGW spectrum is characterized by periods between 1-2 hours and 20 minutes, and horizontal spatial scales of a few hundred km. An alternative approach is to use gravity wave parameterization to account for the effect of wave dissipation.

A parameterization scheme typically assumes a set of wave sources at lower altitudes, and ray traces the original wave spectrum through the model atmosphere. Attenuation due to various factors is calculated (molecular diffusion, thermal conductivity, ion drag, etc), with the resulting deposited momentum acting as an additional forcing on the model. This approach allows for the climatological effects of AGWs to be taken into account in GCMs, without requiring that the model have the resolution necessary to self-consistently simulate the generation and propagation of AGWs. *Yigit et al.* (2009) implemented a gravity-wave parameterization scheme that accounts for sub-grid gravity waves in the thermosphere for the Coupled Middle Atmosphere Thermosphere-2 (CMAT2) model. The effects reported are possibly overestimated, but provide an indication of the importance of gravity waves for thermospheric structure and circulation. *Vadas et al.* (2014) conducted a numerical modeling study on the momentum flux due to gravity waves sourced by deep convection. The global impact is determined using a TIME-GCM simulation (Figure 6.2). While significant wave sources were neglected (mountain waves, high latitude waves sourced in the auroral zones, etc), the reported effect is significant, particularly through changes to the tidal waves. Accelerations of the order of 10^{-4} – 10^{-1} m s^{-2} are reported, with changes to the neutral wind as high as 50 m s^{-1}.

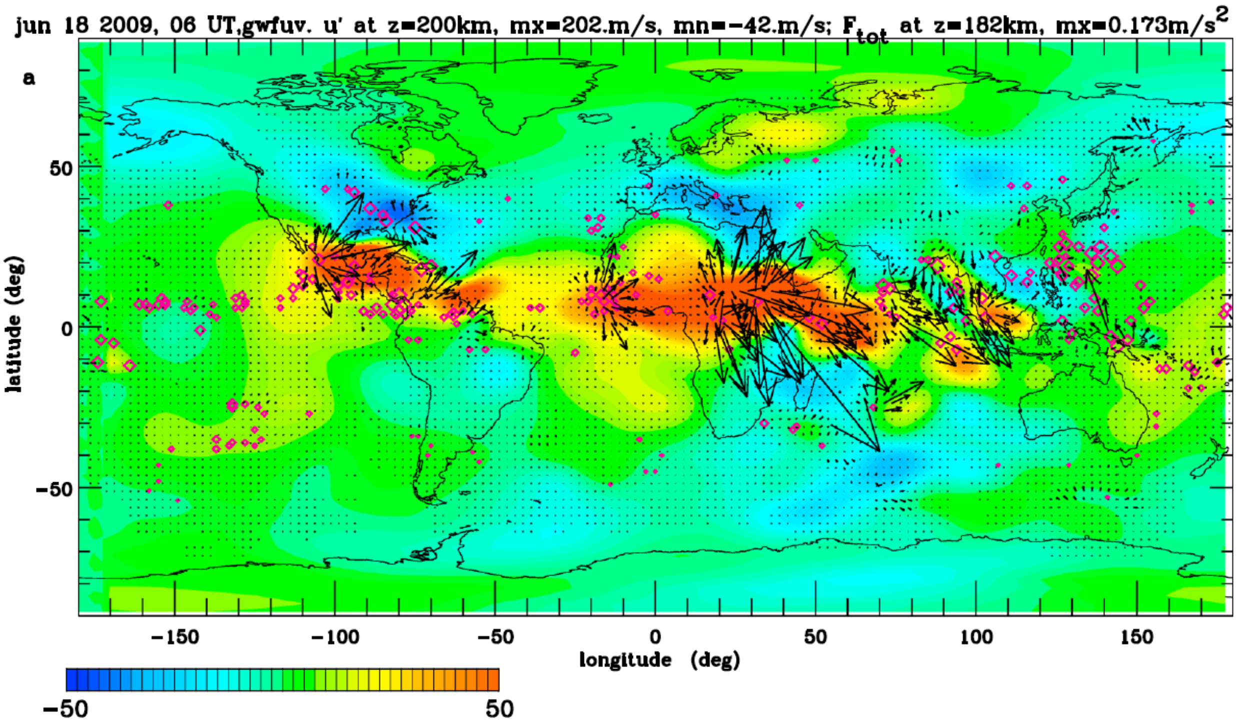

Figure 6.2. Perturbation to the neutral wind due to the gravity wave drag, as determined by Vadas et al. (2014). The color scale shows neutral wind perturbations corresponding to 200 km altitude, at 06:00 UT on 18 June 2009. The arrows correspond to horizontal accelaration, with a maximum value of 0.173 m/s2. Reproduced from Vadas et al. (2014).

It is likely that the thermospheric AGW activity is caused by a multitude of sources of varying relative importance. Waves sourced by deep convection are likely to be dominant at low latitudes. The work presented in Chapters 4 and 5 (Figures 4.13 and 5.9) point to a high-latitude source (or possibly several high-latitude sources) for the dominant daytime wave population that we observe at mid-latitudes. This chapter aims to determine a first estimate of the AGW momentum flux over Wallops Island, and the associated forcing on the background thermosphere-ionosphere. This forcing, referred to as the Gravity Wave Drag (GWD, Equation 6.2) has not been obtained from measurements in the altitude range 140 - 320 km. Yet, such results would be crucially important in constraining future parameterization schemes. This work can be considered a first step towards providing results of this type.

In contrast with the lack of thermospheric measurements of the GWD, much more information is available for lower altitudes. *Guharay and Sekar* (2011) determined the momentum flux over Gadanki, India using Rayleigh LIDAR observation, covering the stratosphere and mesosphere in the 35 – 70 km altitude range. Global datasets are also available: *Alexander and Rosenlof* (2003) used measurements from the Upper Atmosphere Research Satellite (UARS). A dataset covering 5.6 years of temperature measurements were analyzed, highlighting semiannual, annual and biannual periodicities of the momentum flux (Figure 6.3). *Ern et al.* (2004) used Cryogenic Infrared Spectrometers & Telescopes for the Atmosphere (CRISTA) satellite data to determine global estimates of momentum flux in the stratosphere. The resulting maps were compared to predictions of a gravity wave parameterization scheme. Significant differences were reported, both qualitative and quantitative.

Existing work on the AGW momentum flux and associated GWD does indicate what some of the features of our final results should be. In the total absence of wave attenuation, the momentum flux, (F_x, F_y), would remain constant along the propagation path. Under the assumption that the majority of AGWs are propagating upward in altitude, wave attenuation should result in a momentum flux decreasing with height. This is not necessarily true for small frequency ranges or over small time intervals (for individual AGW events). As discussed in the previous chapters, a large population of TIDs observed over Wallops Island is likely to have high-latitude sources. Since these waves did not originate in the lower atmosphere in the vicinity of the station, their propagation path may not extend to lower altitudes within the station's field of view. The result may be that some of these waves do not produce perturbations in the lower F_1-Layer, but they do in the upper F_1 and F_2 Layers. However, results averaged over longer time periods are expected to show a decrease of the momentum flux over a broad altitude range.

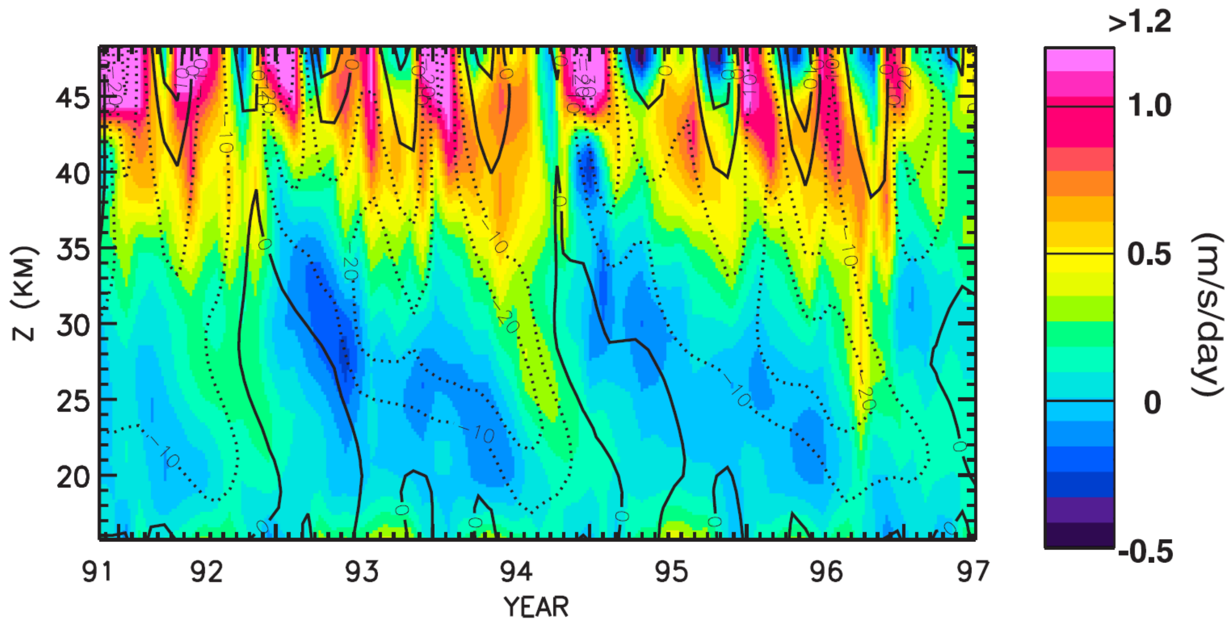

Figure 6.3. Variability of the forcing due to gravity waves (Alexander and Rosenlof, 2003). The result corresponds to equatorial latitudes, averaging measurements taken between 15 ºN and 15 ºS.

The momentum flux in the lower atmosphere is known to be highly variable, and existing results by *Vadas et al.* (2014) suggest that an even higher degree of variability may be observed in the thermosphere. This is not surprising, as the atmospheric variability is known to be higher in the thermosphere. It is difficult to predict what values to expect for the momentum flux at a certain altitude, as well as the exact dependence of the momentum flux with altitude. It is however, reasonable to expect that the momentum flux in the thermosphere would be smaller than the values reported in the stratosphere or mesosphere. Indeed, since *Ern et al.* (2004) reported values of the order of 0.1 – 50 mPa for the momentum flux at 25 km altitude, and *Geller et al.* (2013) reported values of the order 10^{-3} – 0.75 mPa at 50 km, thermospheric values of the same quantity are likely to be a many orders of magnitude smaller. Finally, the accelerations obtained by *Vadas et al*. (2014) at 200 km altitude (represented by the arrows in Figure 6.2) have a maximum of 0.173 m s^{-2} at low latitudes. Note that while most of the values for the acceleration were considerably smaller (particularly at latitudes higher than 30º), the net change in the TIME-GCM winds was as high as 50 m s^{-1}.

6.2. Analysis Methodology

Figure 6.4 shows Doppler speed data obtained at Wallops Island for 24 October 2013. Evidence of AGWs is observed throughout most of the day in the data, similarly to the corresponding electron density and tilts (Figure 5.1). Determining the Doppler speed from the raw Dynasonde measurements is discussed in detail in sections 3.2 and 4.3. The end result is essentially equal to the vertical component of the plasma velocity. The observed periodic oscillations in the plasma drift are caused by the underlying oscillations in the neutral atmosphere. It is possible to backtrack this process and recover the amplitude of the original neutral wind oscillations (u'_x, u'_y and u'_z) from the observed vertical plasma drift oscillations (u'_{iz}). For this, a discussion is necessary on the ion-neutral coupling and the relation between the components of the neutral wind perturbation vector.

By only considering waves with periods less than several hours, the effect of the Earth's rotation can be neglected. Non-linear effects are also disregarded at this point. The background atmosphere neutral winds and temperature are assumed to be varying only smoothly (Figure 6.5) with time, and the representative spatial scales of their horizontal and vertical variation is assumed to be large compared to the horizontal and vertical wavelengths of the AGWs considered. No restriction is imposed on the background pressure and neutral density.

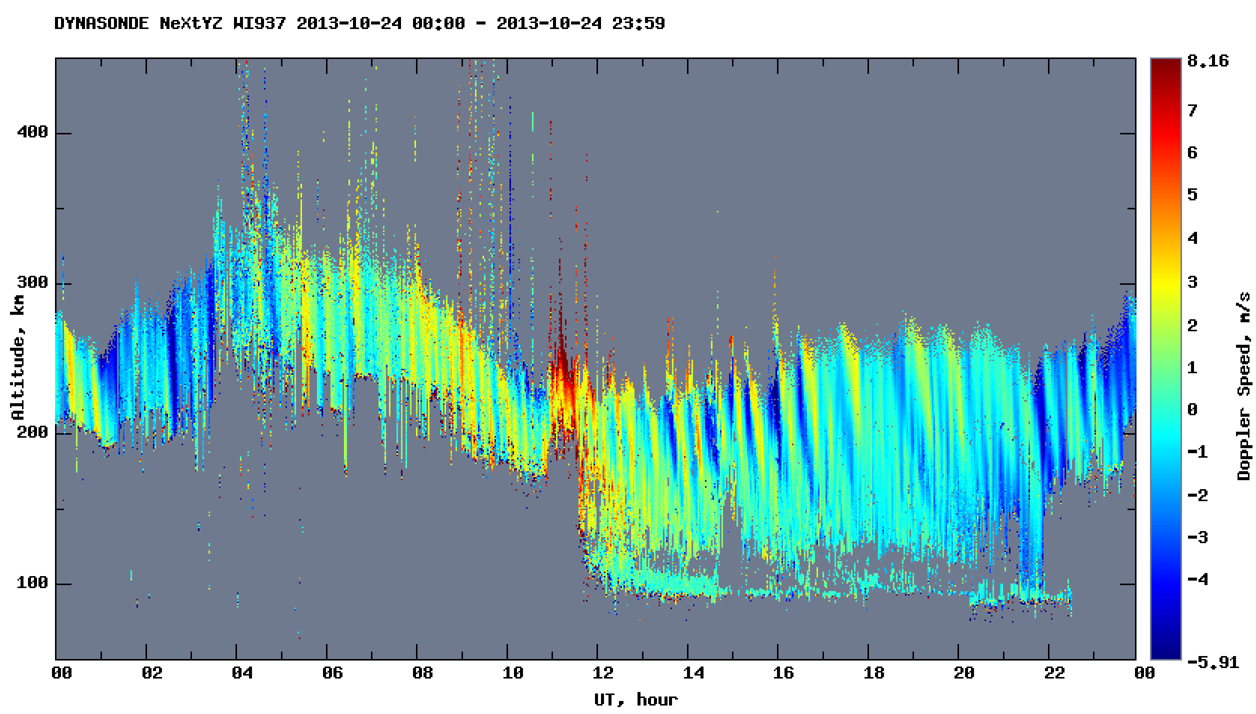

Figure 6.4. The vertical components of the line-of-sight Doppler speed at Wallops Island, 24 October 2014. The format is the standard display provided by the Dynasonde software. Similar results can be obtained at http://surf.colorado.edu.

Under these assumptions, the amplitudes of the wave-induced perturbations in different atmospheric parameters can be assumed to be proportional to each other through so-called polarization relations (*Fritts and Alexander*, 2003). These can be obtained using an asymptotic form (*Godin, 2014*) of the linearized equations of motion are:

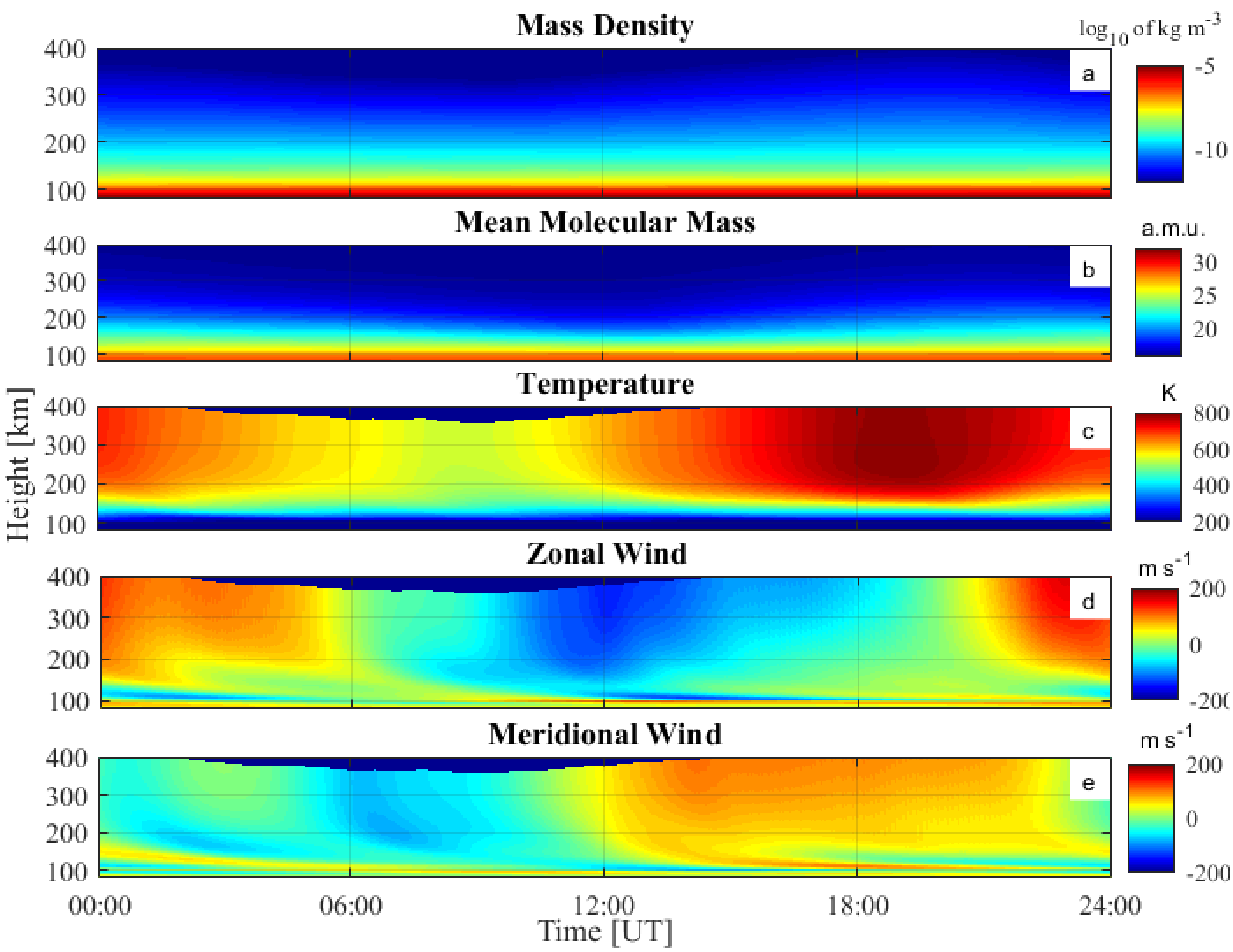

Figure 6.5. Diurnal variation of the model-atmosphere parameters: (a) neutral mass density, (b) mean molecular mass in atomic mass units, (c) neutral temperature, (d) zonal and (e) meridional neutral wind. Derived from results of the Whole Atmosphere Model.

$$\omega_0\rho\, \boldsymbol{u}_h{}' = \boldsymbol{k}_h p', \qquad \omega_0\rho\, u_z{}' = \left(k_z + \frac{i}{2H}\right) p' - ig\rho' \tag{6.3}$$

$$\omega_0 \rho' = \rho \left[\boldsymbol{k}_h \cdot \boldsymbol{u_h}' + \left(k_z + \frac{i}{2H} \right) u_z' \right] \tag{6.4}$$

$$-i\omega_0 (p' - c_z^2 \rho') = \rho\, u_z \left(g - \frac{c_s^2}{H} \right) \tag{6.5}$$

Equations (6.3) - (6.5) follow from the Euler equation, continuity equation, and the equation of state, respectively, where the following quantities are used:

- $\omega_0 = \omega - \boldsymbol{k_h} \cdot \boldsymbol{u_h}$ is the intrinsic wave frequency,
- ω is the ground-based (observed) frequency,
- $\boldsymbol{k}_h$ and k_z are the horizontal and vertical components of the AGW wavevector,
- $\boldsymbol{u_h}$ is the horizontal background neutral wind vector,
- $\boldsymbol{u}' = (u_x', u_y', u_z')$ is the perturbation neutral wind vector, with $\boldsymbol{u_h}' = (u_x', u_y', 0)$ its horizontal component,
- ρ is the background mass density,
- p' and ρ' are the pressure and mass density perturbation,
- $c_s^2 = \sqrt{\frac{\gamma k_B T}{M}}$ is the sound speed,
- $H = \frac{c_s^2}{\gamma g}$ is the scale height,
- M is the mean molecular mass,
- T is the background neutral temperature,
- k_B is the Boltzmann constant
- γ is the ratio of specific heats at constant pressure and constant volume
- g is the gravitational acceleration.

The condition of existence of non-trivial solutions to Equations (6.3) – (6.5) is the AGW dispersion relation (Equation 5.12). In addition to this, polarization relations are obtained in the form $\boldsymbol{u}' = \boldsymbol{C_u}\frac{\rho'}{\rho}$**,** with:

$$\boldsymbol{C_u} = (C_x, C_y, C_z) = \left(\frac{k_x c_s^2}{\omega_0}, \frac{k_y c_s^2}{\omega_0}, \frac{-i\omega_0 c_s^2\left(\frac{gk_\perp^2}{\omega_0^2}+ik_z-\frac{1}{2H}\right)}{\omega_0^2-\frac{gk_\perp^2}{\omega_0^2}+\frac{c_s^2}{H}\left(\frac{gk_\perp^2}{\omega_0^2}+ik_z-\frac{1}{2H}\right)} \right) \tag{6.6}$$

The neutral wind perturbations cause perturbations in the plasma velocity. The general dependence of the plasma velocity vector on the neutral wind vector dictates that in response to an arbitrarily oriented wind vector, $\boldsymbol{u}$, the plasma velocity will have a component along the magnetic field line, a component along the original direction of $\boldsymbol{u}$, and a component perpendicular to both (*McLeod*, 1965):

$$\boldsymbol{u}_i = [\omega_i^2 + \nu_{in}^2]^{-1}\left[\nu_{in}\omega_i \boldsymbol{u} \times \widehat{\boldsymbol{B}} + \omega_i^2\left(\boldsymbol{u} \cdot \widehat{\boldsymbol{B}}\right)\widehat{\boldsymbol{B}} + \nu_{in}^2 \boldsymbol{u}\right] \tag{6.7}$$

where $\boldsymbol{u}_i = (u_{ix}, u_{iy}, u_{iz})$ is the plasma velocity vector, $\widehat{\boldsymbol{B}}$ is a unit vector in the direction of the magnetic field vector, and ω_i and ν_{in} are the ion gyrofrequency, which is constant for a given ion species and the ion-neutral collision frequency which depends primarily on the neutral number density. At altitudes above 140 km, the density is low enough, making the collision frequency negligible when compared to the ion gyrofrequency $\nu_{in}^2 \ll \omega_i^2$, and the plasma velocity can be approximated as having the same direction as the magnetic field lines, meaning that only the $\omega_i^2\left(\boldsymbol{u} \cdot \widehat{\boldsymbol{B}}\right)\widehat{\boldsymbol{B}}$ term in Equation (6.7) needs to be considered. Under this approximation, the vertical component of the plasma velocity perturbation (u_{iz}') will depend solely on the meridional and vertical wind perturbations:

$$u_{iz}' = -sinI\ cosI\ u_y' + sinI^2\ u_z' \tag{6.8}$$

When using equation (6.8), a dipole field will be assumed for $\hat{\boldsymbol{B}}$, with a magnetic dip angle I related to the geographical latitude (θ) by (*Hickey et al.*, 2009):

$$\sin I = -2\sin\theta\ \sqrt{1+3\,sin^2\theta} \qquad \text{and} \qquad \cos I = -\cos\theta\ \sqrt{1+3\,sin^2\theta} \tag{6.9}$$

Using Equations (6.6) and (6.8), the amplitude of the vertical component of the neutral wind perturbation can be obtained from the measured amplitude of the vertical plasma velocity perturbation:

$$u_z{}' = u_{iz}{}'\left[SinI\ CosI\ \frac{k_y c_s^2}{\omega_0\ C_z} + \ SinI^2\right]^{-1} \tag{6.10}$$

From equation (6.6), the amplitudes of the meridional and zonal components of the neutral wind perturbation are:

$$u_y{}' = C_y\ \frac{u_z{}'}{C_z} \tag{6.11}$$

$$u_x{}' = C_x\ \frac{u_z{}'}{C_z} = \frac{k_x}{k_y}\ u_y{}' \tag{6.12}$$

6.3. Gravity Wave Momentum Flux and Gravity Wave Drag

The spectral analysis methodology described in Section 4.2 is applied to the Doppler speed data shown in Figure 6.4. The sample result in Figure 6.6 shows the same major spectral features as the results for the electron density and ionospheric tilt in Figure 5.4. Here, the response of the Doppler speed to a wave with frequency ω and wavevector $\boldsymbol{k}$ is approximated locally by a plane-wave model:

$$u_{iz}{}' = u_{0iz}{}'(\omega, z)\exp[i(\boldsymbol{\varphi} - \omega t)] \qquad \text{where } \nabla\varphi = \text{k} \tag{6.13}$$

Note that Figure 6.6 shows the spectral amplitude, $u_{0iz}{}'$ and its dependence on frequency and altitude.

The wavevector components are determined using the same methodology described in Chapter 5. Similar filtering criteria are applied to focus on the dominant wave activity: a mean amplitude and standard deviation of the Doppler speed spectrum is calculated for each frequency, altitude and local time, and data points with amplitudes less than one standard deviation above the mean amplitude are excluded. The characteristics of the background atmosphere are obtained using a month-long WAM simulation for conditions similar to those during the month of October 2013. To extract a climatologically-accurate set of model results, for each local time and altitude a mean value is determined using the 31 results corresponding to individual days. The resulting mean neutral mass density, mean molecular mass, neutral temperature, and zonal and meridional neutral winds are shown in Figure 6.5. Note that this is the same climatologically accurate neutral atmosphere used in Chapter 5 to successfully test the agreement between Dynasonde-derived TID propagation parameters and the theoretical AGW dispersion relation.

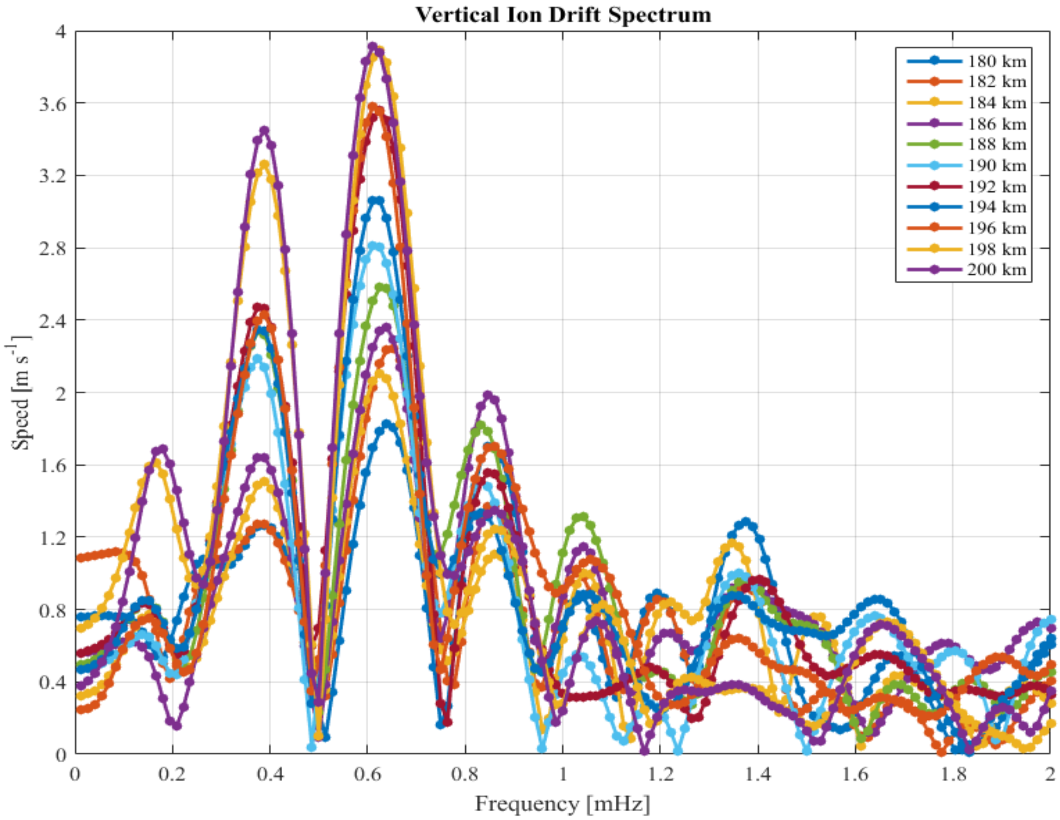

Figure 6.6. Height variation of the Doppler speed data obtained at Wallops Island on 10:16 LT, 24 October 2013.

Equations (6.10) – (6.12) are then used to determine the neutral wind perturbation spectrum. A sample result for the meridional wind component is shown in Figure (6.7).

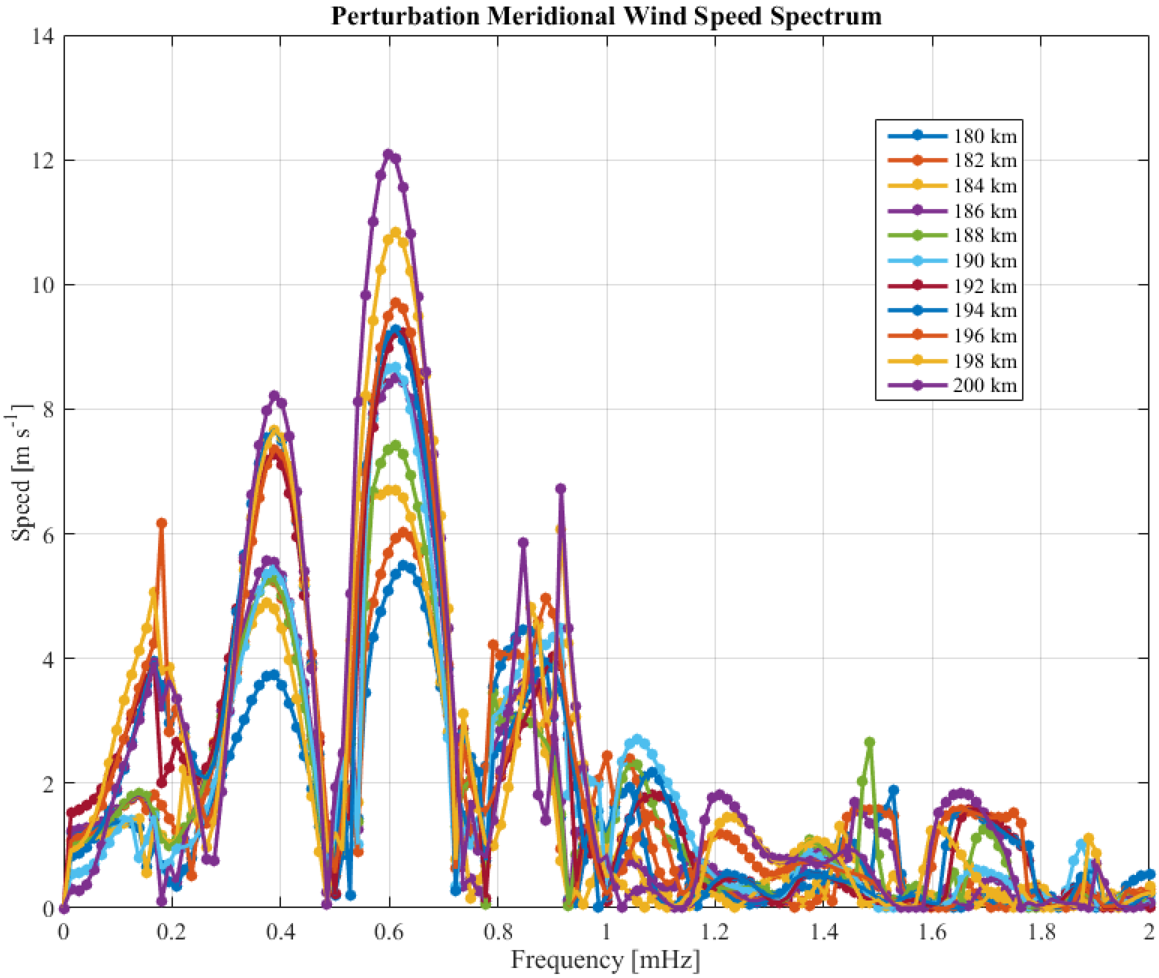

Figure 6.7. Height variation of the meridional wind speed spectrum obtained at Wallops Island on 10:16 LT, 24 October 2013, using the Doppler speed spectrum and Equations (6.10) and (6.11)

The momentum flux can now be determined using Equation (6.1). The result will be frequency dependent, and the first step is to determine the contribution due to a single wave package. Figure 6.8 shows the zonal and meridional momentum flux over a 12-hour interval on 24 October 2013 at Wallops Island, integrated over a small 0.2 mHz frequency range around 0.6 mHz, corresponding to a period of approximately 30 minutes. The result is shown in Figure 6.8. The amplitude of the meridional component (F_y) was generally higher than that of the zonal component (F_x). This is in agreement with the propagation direction obtained for this wave in Chapter 5 and listed in Table 5.1. Both components of the momentum flux are highly variable, both with time and altitude. The height dependence is often in disagreement with the assumption of purely vertical propagation (mainly between 13:00 and 15:30, when the momentum flux tends to increase with altitude), further suggesting a more distant, high latitude source, as opposed to a local, lower atmosphere one.

The total momentum flux for the same time interval is obtained by integrating over the entire frequency range 0.13 - 4.14 mHz. The magnitude and direction of this momentum flux vector are shown in Figure 6.9, for the same dataset at Wallops Island on 24 October 2013. During the altitude ranges and periods when the momentum flux magnitude was high (approximately 10^{-7} Pa, mainly from 13:00 UT to 17:30 UT), a clear direction of the vector can be observed (South / South-East). For most of the remainder of the interval, the momentum flux vector was oriented westward, with a magnitude up to 2 orders of magnitude smaller, but much more variable. Due to the high variability of these results, a considerably longer dataset is necessary to obtain an estimate of the mean GWD flux and its variation with height.

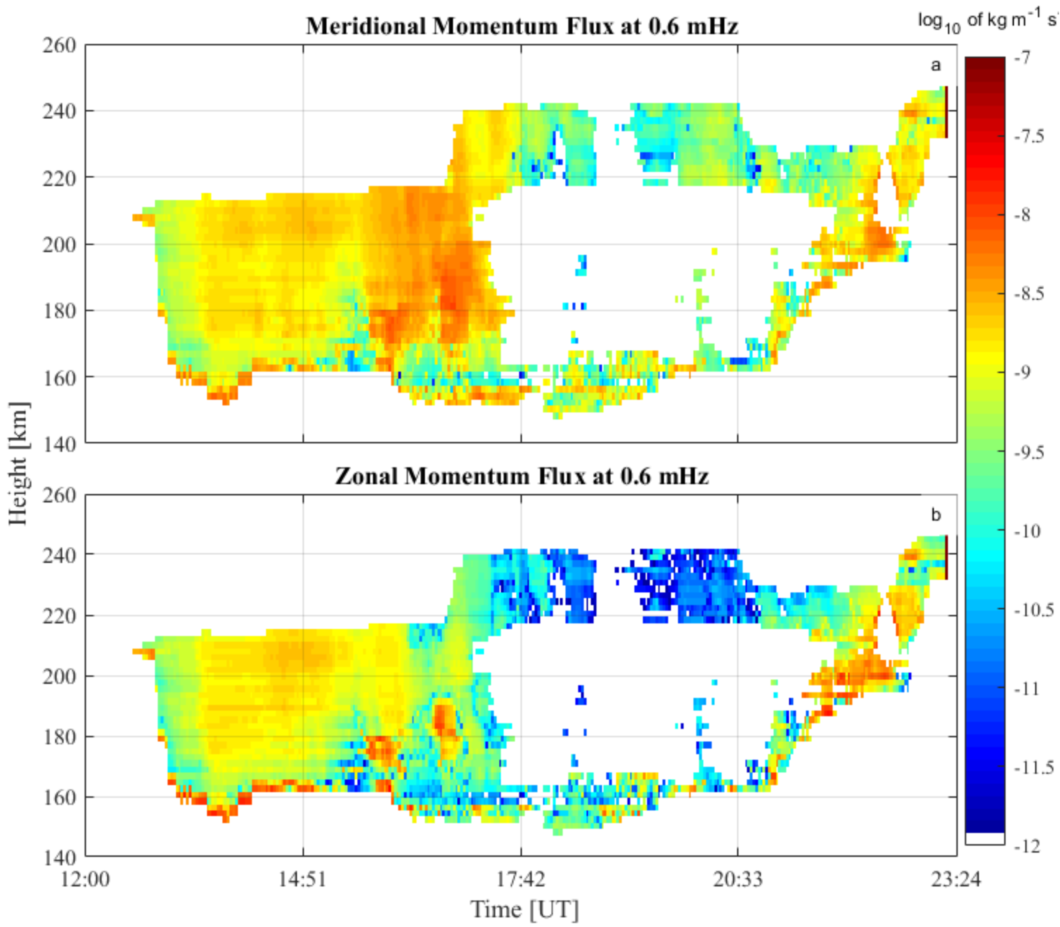

Figure 6.8. Temporal and altitude dependence of the (a) meridional and (b) zonal components of the momentum flux, for a wave with an approximate period of 30 minutes at Wallops Island on 24 October 2013.

A 10-day-long dataset obtained at Wallops Island between 15 and 24 October 2013 was used to obtain a statistically accurate mean height profile for the total momentum flux. To avoid ambiguities regarding the height dependence of the results, the daytime and nighttime data are analyzed separately. At each altitude, the magnitude and direction of the total momentum flux are determined. Due to the high temporal variability observed in Figures 6.8 and 6.9, it is necessary to also determine the standard deviation around the mean value. Finally, the gravity wave drag is determined using Equation (6.2). The results are shown in Figure 6.10, covering the altitude range 140 – 220 km during daytime and 215 – 320 km during nighttime. The total number of data points used to determine these height profiles is very different for the two time periods. The filtering criteria applied result in a height dependence of the number of counts similar to that in Figure 5.10. The lower number of counts during nighttime is reflected in the increased variation with height of the red curves in Figure 6.10a and b.

The trend in Figure 6.10a is one of decreasing magnitude with height, indicating the upward propagation of gradually dissipating AGWs. The sudden transition (by more than an order of magnitude) between the daytime and nighttime value of the momentum flux around 220 km in likely due to the change in local time. The reader is advised not to consider the nighttime height profile a continuation of the daytime height profile. The direction of the momentum flux vector is considerably different for daytime (South / South-East) and nighttime (East) (Figure 6.10b). This is a consequence of the different preferred propagation direction for daytime and nighttime (Figure 5.9). The standard deviation associated with this mean height profile of the momentum flux (Figure 6.10c) is comparable or higher to the mean at all altitudes. Finally, the height profile of GWD has typical values of the acceleration in the range 10^{-4} - 10^{-2} ms^{-2} during daytime and 10^{-3} - 10^{-1} ms^{-2} during nighttime.

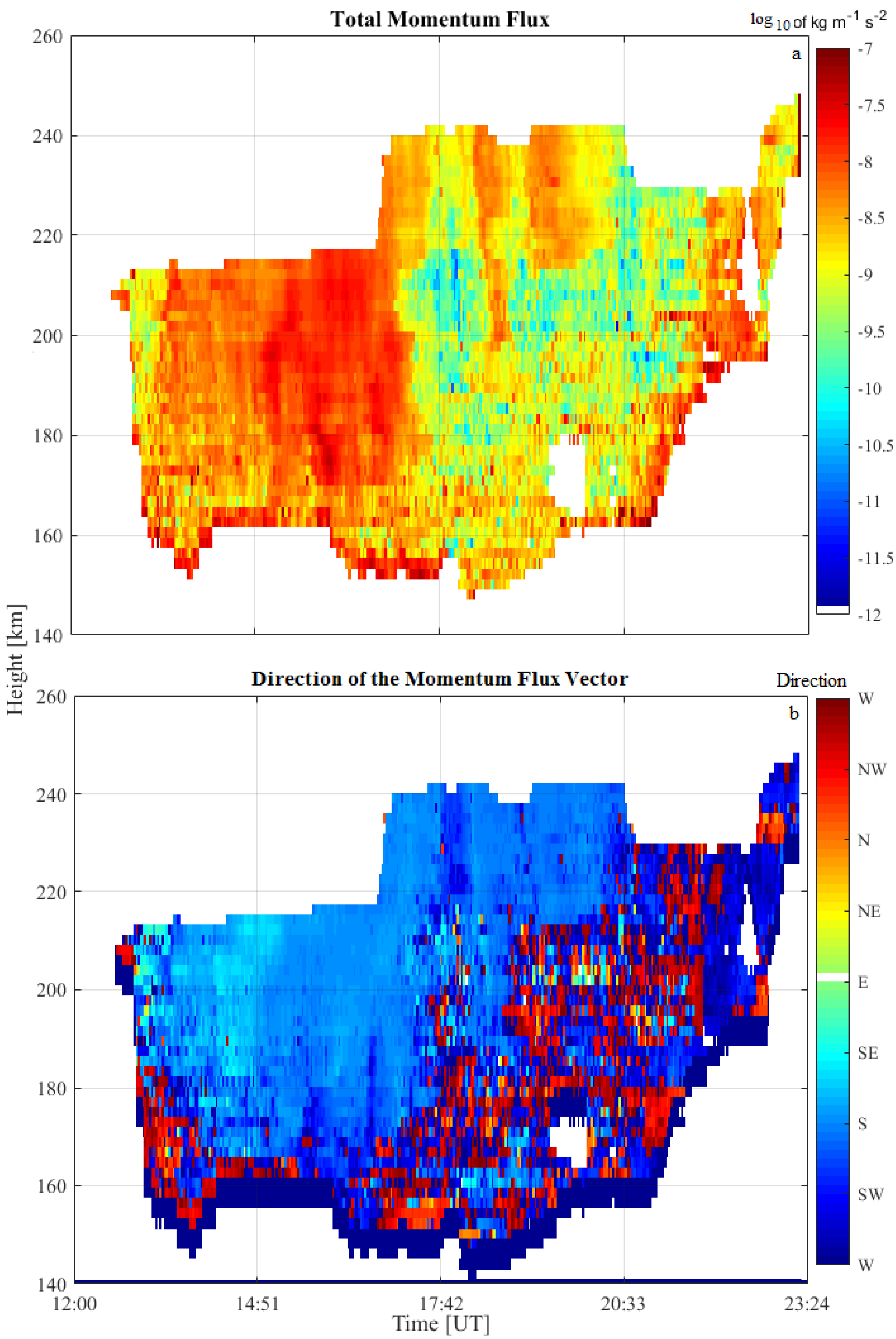

Figure 6.9. The magnitude (a) and direction (b) of the total momentum flux vector. Integrated over the entire frequency range 0.13 - 4.14 mHz.

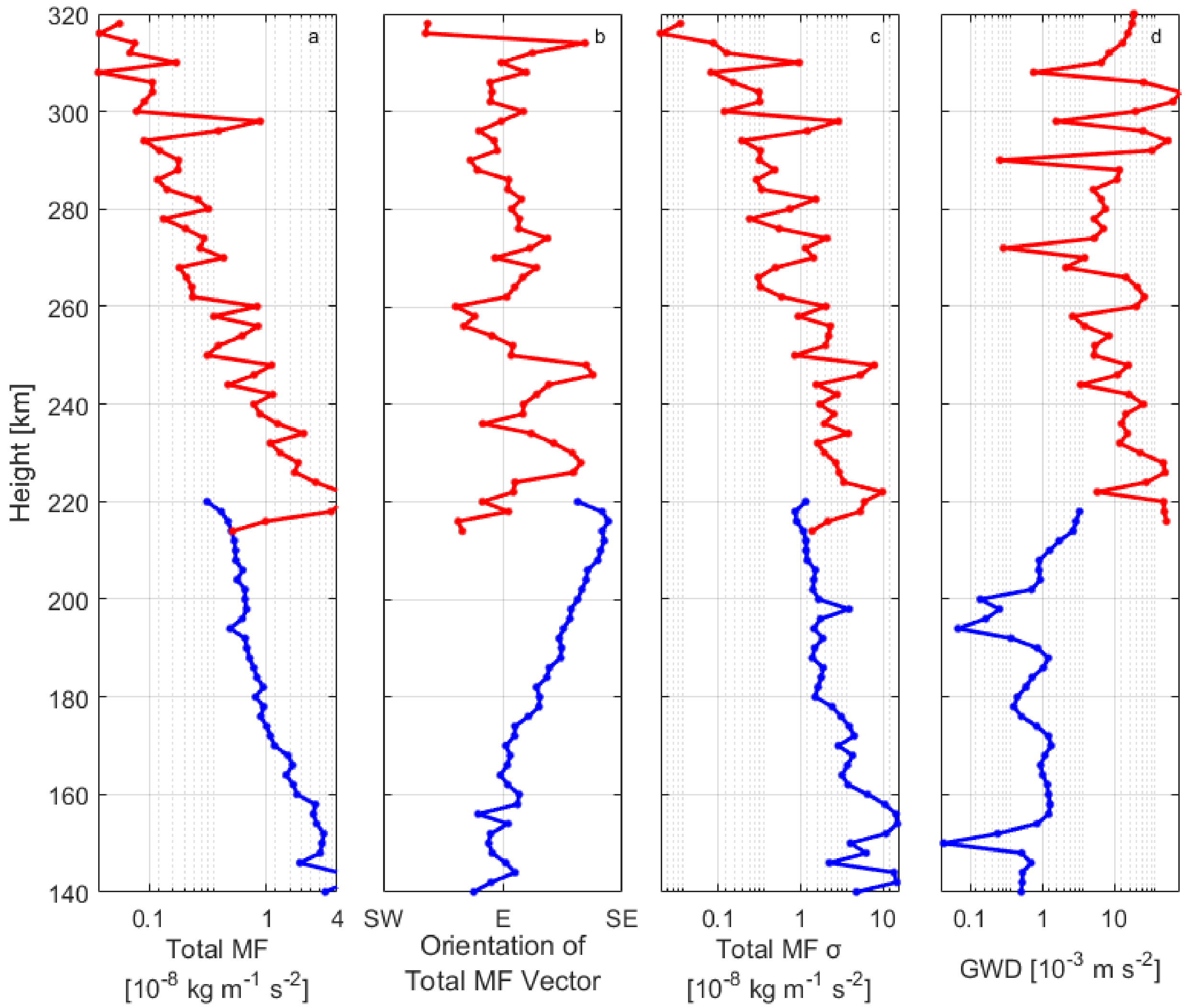

Figure 6.10. Mean height profiles of the total momentum flux (a), direction (b) standard deviation, (c) and gravity wave drag (d). For each quantity, a separate height profile is calculated for daytime (blue) and nighttime (red) data.

A discussion is necessary on the magnitude of the daytime GWD. As shown in Figure 6.8, the contribution to the total momentum flux due to AGWs at some frequencies does not follow the same height dependence as seen in Figure 6.10a. Evidence suggests that these southward propagating waves have high-latitude sources, rather than local sources in the lower atmosphere. Since these waves are subject to the same causes of damping as the rest of the AGW spectrum, it is expected that they in fact contribute to the GWD. Equation 6.1 describes only the vertical flux of horizontal momentum. It can, however, be generalized to include all components of the momentum flux tensor:

$$F = \begin{pmatrix} F_{xx} & F_{yx} & F_{zx} \\ F_{xy} & F_{yy} & F_{zy} \\ F_{xz} & F_{yz} & F_{zz} \end{pmatrix} = \bar{\rho} \begin{pmatrix} \overline{u_x'^2} & \overline{u_y' \, u_x'} & \overline{u_z' \, u_x'} \\ \overline{u_x' \, u_y'} & \overline{u_y'^2} & \overline{u_z' \, u_y'} \\ \overline{u_x' \, u_z'} & \overline{u_y' \, u_z'} & \overline{u_z'^2} \end{pmatrix} \tag{6.14}$$

Accurately accounting for the impact of southward propagating waves would require determining the F_{xy} and F_{yy} components of F from equation (6.14) at a minimum of two locations along the propagation path of these waves. In this case, an additional instrument would be required either approximately north or south of Wallops Island. Such an experimental setup currently does not exist. At this time, the conclusion is that the GWD in Figure 6.10d is underestimated by an unknown amount.

This result does impose a lower limit on the impact of AGW dissipation on the background flow for the considered time interval of 14 – 24 October 2013 at Wallops Island. For example, in Figure 6.9 the orientation of the momentum flux vector remains approximately constant for a period of over 4 hours. Assuming a value of the GWD of $2 \cdot 10^{-2}$ ms^{-2}, the net effect of this acceleration would be an approximate change of the neutral wind by 40 m/s. A more accurate estimate of the change to the neutral wind would also require data from instruments broadly spread geographically, providing a global map of the GWD that could be used as an additional forcing for a GCM such as WAM or CTIPe.

This Chapter builds upon the spectral analysis methods developed in Chapters 4 and on the method for determining the wavevector components developed in Chapter 5 to obtain estimates of the momentum flux and its characteristics at Wallops Island for a

10-day period between 15 and 24 October 2013. This result could be used to constrain gravity wave parameterization schemes by comparing these values of the momentum flux (and its frequency dependence) to the results of parameterization schemes in the thermosphere-ionosphere. The height dependence of the momentum flux is used to determine the acceleration acting on the mean thermospheric flow due to gravity wave dissipation. This acceleration is estimated to cause changes in the neutral wind as large as least several tens of m/s for the dataset used.

CHAPTER 7

CONCLUSIONS AND FUTURE WORK

7.1. Conclusions

This is one of the first studies of the wave activity in the thermosphere-ionosphere that uses Dynasonde-capable instruments as its primary data source. The results of this work demonstrate the possibility of using such measurements to investigate key features of the atmospheric wave field, both for large-scale tidal waves and smaller scale acoustic gravity waves.

In Chapter 4, the limitations of existing spectral analysis techniques are discussed within the context of the non-uniform sampling due to the natural ionospheric variability. In the case of the AGW spectrum, a new approach is developed for the study of the main wave spectrum. Based on the Lomb-Scargle and Welch methods and using filtering criterion derived from first principles, this new approach may have a much broader applicability in the field of spectral analysis. Here, the method was used to investigate the seasonal variability of the Power Spectral Density of AGWs and associated travelling ionospheric disturbances. By analyzing the ionospheric tilts and Doppler speed data from Wallops Island, VA and Tromso, Norway, the presence of two peaks in wave activity is highlighted. First, a winter peak, previously observed using other remote sensing techniques, and a second peak during summer, previously unreported in the literature. Finally, the main features of the first three tidal harmonics are investigated using electron density and tilt data from Wallops Island and San Juan, PR for two datasets in May-June and October-November 2013.

Chapter 5 successfully accomplishes the task of providing a complete characterization of the propagation parameters of TIDs. For the first time, the agreement between the TID propagation parameters and the AGW dispersion relation is successfully verified in a quantitative way. The statistical distribution of the propagation parameters is investigated, including its altitude dependence, for a month-long dataset from Wallops Island. A preferred southward propagation direction is highlighted for daytime TIDs with frequencies below 1 mHz (periods larger than 16.6 minutes). Finally, building on the results in Chapters 4 and 5, and using many of their results as a basis, Chapter 6 investigates the momentum flux due to AGWs at Wallops Island. Its temporal and altitude variability is investigated, and the presence of waves sourced at high-latitudes is shown to have significant implications that differentiate the thermospheric wave activity from that in the middle and lower atmosphere. Using a 10-day dataset, estimates are obtained of the average height profile of the momentum flux magnitude, direction and variability, and from this, the minimum forcing on the background thermosphere-ionosphere due to gravity wave dissipation is obtained.

7.2. Future Work

The results obtained as part of this thesis open many interesting avenues for future research. The general nature of the methods developed here will allow for their applicability on Dynasonde data from other locations, as such data becomes available. Results from a network of Dynasonde instruments distributed over a broad range of geographical locations would allow for the characterization of the TID activity on a global scale. In the near future, data that is appropriate for the analysis methodologies described in this work will hopefully become available from San Juan, PR, Boulder, CO and Kiruna, Sweden.

The spectral analysis methodology described in Chapter 4, section 4.1 is based on general principles, and its applicability should be tested using other types of data, ionospheric or otherwise. It is reasonable to assume that its capacity to compensate for the effects of non-uniform sampling will depend on the spectral characteristics of the quantity being studied, rather than on the specific data acquisition method.

The seasonal variability of the PSD integral of the ionospheric tilts and Doppler speed shows features that are of considerable importance, such as the presence of two peaks in TID activity during a year. However, the time span of only 3 years does not allow for establishing the relative amplitude of these two peaks. As more data is accumulated at Wallops Island, the analysis performed in Chapter 4, section 4.3 will be expanded to include a longer time period. Additionally, as appropriate measurements are taken at San Juan, and hopefully, Kiruna and Boulder, the dependence of the TID PSD on geographical location will be more accurately investigated.

The agreement between the AGW dispersion relation and the TID propagation parameters was demonstrated here for a limited dataset. Building on this result, the discrepancies observed for certain frequencies must be investigated. The likely causes for these are the impact of wave attenuation on the propagation parameters and the limits of the WKB approximation. A better understanding of these factors should allow for an automated approach to selecting the parts of the TID spectrum that are unequivocally caused by AGWs. A related possibility is the role of the neutral background winds on the dispersion relation. *Vadas and Nicolls* (2008) determined the neutral background wind using ISR measurements and the gravity wave theory. A similar approach could be applied using Dynasonde data.

The statistical distribution of the TID propagation parameters was obtained for a month-long dataset from Wallops Island. Further investigations of this kind would be of interest, to determine the seasonal variability of these statistical distributions. Also, using data from other Dynasonde stations would allow for the geographical dependence to be studied. If an objective method could be implemented for establishing weather an observed TID is caused by a AGW, then the statistical distribution of the propagation parameters could be limited only to TIDs that are unambiguously caused by underlying AGWs.

Finally, the momentum flux and associated gravity wave drag can be used by modelers to account for the impact of sub-grid gravity waves. This would require many more results as those discussed in Chapter 6, geographically spread to cover all latitude ranges. Indeed, even an approximate result for the geographical distribution of the ionospheric GWD could improve results of existing and future general circulation models.

CHAPTER 8

BIBLIOGRAPHY

Afraimovich, E. L., Palamartchouk, K. S., Perevalova, N. P. (1998), GPS radio interferometry of travelling ionospheric disturbances, Journal of Atmospheric and Solar-Terrestrial Physics, vol. 60, no. 12, pp. 1205-1223, DOI: 10.1016/S1364-6826(98)00074-1

Afraimovich, E. L., Kosogorov, E. A., Leonovich, L. A., Palamartchouk, K. S., Perevalova, N. P., Pirog, O. M. (1999), Determining parameters of large-scale traveling ionospheric disturbances of auroral origin using GPS-arrays, Journal of Atmospheric and Solar-terrestrial Physics - J ATMOS SOL-TERR PHYS , vol. 62, pp. 553-565, DOI: 10.1016/S1364-6826(00)00011-0

Akmaev, R. A., T. J. Fuller-Rowell, F. Wu, J. M. Forbes, X. Zhang, A. F. Anghel, M. D. Iredell, S. Moorthi, and H.-M. Juang (2008), Tidal variability in the lower thermosphere: Comparison of Whole Atmosphere Model (WAM) simulations with observations from TIMED, Geophys. Res. Lett., 35, L03810, doi:10.1029/2007GL032584.

Akmaev, R. A. (2011), Whole atmosphere modeling: Connecting terrestrial and space weather, Rev. Geophys., 49, RG4004, doi:10.1029/2011RG000364.

Alexander, M. J., and K. H. Rosenlof, Gravity-wave forcing in the stratosphere: Observational constraints from the Upper Atmosphere Research Satellite and implications for parameterization in global models, J. Geophys. Res., 108(D19), 4597, doi:10.1029/2003JD003373, 2003.

Angelats i Coll, M., and J. M. Forbes (2002), Nonlinear interactions in the upper atmosphere: The s = 1 and s = 3 nonmigrating semidiurnal tides, J. Geophys. Res., 107(A8), 1157, doi:10.1029/2001JA900179.

Baluev, R. V. (2008), Assessing statistical significance of periodogram peaks, Mon. Not. Astron. Soc., 385(3), 1279–1285, doi:10.1111/j.1365-2966.2008.12689.x

Gillian Boccara, Albert Hertzog, Robert A. Vincent, and François Vial, 2008: Estimation of Gravity Wave Momentum Flux and Phase Speeds from Quasi-Lagrangian Stratospheric Balloon Flights. Part I: Theory and Simulations. J. Atmos. Sci., 65, 3042–3055.doi: http://dx.doi.org/10.1175/2008JAS2709.1

Tiltmann Bosinger, James LaBelle, Hertmann J. Opgenoorth, Jean-Pierre Pommereau, Kazuo Shiokawa, Stan Solomon and Rudolf A. Treumann (editors), Dynamic coupling between Earth's atmosphertic and plasma environments, 2012, Springer

Bristow, W. A., R. A. Greenwald, and J. C. Samson (1994), Identification of high latitude acoustic gravity wave sources using the Goose Bay HF radar, J. Geophys. Res., 99, 319–331.

Bristow, W. A., R. A. Greenwald, and J. P. Villain (1996), On the seasonal dependence of medium-scale atmospheric gravity waves in the upper atmosphere at high latitudes, J. Geophys. Res., 101(A7), 11585– 11595, doi:10.1029/96JA01010.

Butzer, P. L., Stens, R. L. (1992), Sampling Theory for not Necessarily Band-Limited Functions: A Historical Overview, SIAM Review, 34, 1, 40-53.

Chapman, S., and R. S. Lindzen (1970), Atmospheric Tides: Thermal and Gravitational, 200 pp, Gordon and Breach, New York.

Chen F.F., Introduction to plasma physics and controlled fussion, Volume 1: Plasma Physics, Second Edition, 1983, Springer

Chen, C. H., C. H. Lin, L. C. Chang, J. D. Huba, J. T. Lin, A. Saito, and J. Y. Liu (2013), Thermospheric tidal effects on the ionospheric midlatitude summer nighttime anomaly using SAMI3 and TIEGCM, J. Geophys. Res. Space Physics, 118, 3836–3845, doi:10.1002/jgra.50340.

Crowley, G., T. B. Jones, and J. R. Dudeney (1987), Comparison of short period TID morphologies in Antarctica during geomagnetically quiet and active intervals, J. Atmos. Terr. Phys., 49, 1155–1162.

Crowley, G., and F. S. Rodrigues (2012), Characteristics of traveling ionospheric disturbances observed by the TIDDBIT sounder, Radio Sci., 47, RS0L22, doi:10.1029/2011RS004959.

Davies K., Ionospheric Radio Waves, 1969, Blaisdell Publishing Company

de Larquier, S., J. M. Ruohoniemi, J. B. H. Baker, N. Ravindran Varrier, and M. Lester (2011), First observations of the midlatitude evening anomaly using Super Dual Auroral Radar Network (SuperDARN) radars, J. Geophys. Res., 116, A10321, doi:10.1029/2011JA016787.

Djuth, F. T., L. D. Zhang, D. J. Livneh, I. Seker, S. M. Smith, M. P. Sulzer, J. D. Mathews, and R. L. Walterscheid (2010), Arecibo’s thermospheric gravity waves and the case for an ocean source, J. Geophys. Res., 115, A08305, doi:10.1029/2009JA014799.

Eng, F., Gustafsson, F. (2008), Downsampling Non-Uniformly Sampled Data, EURASIP J. on Adv. In Signal Processing.

Ern, M., P. Preusse, M. J. Alexander, and C. D. Warner (2004), Absolute values of gravity wave momentum flux derived from satellite data, J. Geophys. Res., 109, D20103, doi:10.1029/2004JD004752.

Fang, T.-W., R. Akmaev, T. Fuller-Rowell, F. Wu, N. Maruyama, and G. Millward (2013), Longitudinal and day-to-day variability in the ionosphere from lower atmosphere tidal forcing, Geophys. Res. Lett., 40, 2523–2528, doi:10.1002/grl.50550.

Fedrizzi, M., T. J. Fuller-Rowell, and M. V. Codrescu (2012), Global Joule heating index derived from thermospheric density physics-based modeling and observations, Space Weather, 10, S03001,doi:10.1029/2011SW000724

Fessler, J. A., Sutton, B. P. (2003), Nonuniform Fast Fourier Transforms Using Min-Max Interpolation, IEEE Transactions on Signal Processing, 51, 2, 560-574.

Forbes, J.M. (1995), Tidal and Planetary Waves, Geophys. Monogr. Ser., vol. 87, edited by R.M. Johnson, and T.L. Killeen, pp. 67–88, AGU, Washington, D.C., ISBN: 0-87590-044-5.

Forbes, J., 1991: Middle atmosphere tides and coupling between atmospheric regions. Journal of Geomagnetism and Geoelectricity, 43, 597-609, DOI: 10.5636/jgg.43.Supplement2_597

Forbes J M, Palo S E, Zhang X. 2000. Variability of the ionosphere. J Atmos Terr Phys, 62: 685–693

Forbes, J. M., X. Zhang, and M. E. Hagan (2001), Simulations of diurnal tides due to tropospheric heating from the NCEP/NCAR Reanalysis Project, Geophys. Res. Lett., 28, 3851– 3854.

Forbes, J. M., J. Russell, S. Miyahara, X. Zhang, S. Palo, M. Mlynczak, C. J. Mertens, and M. E. Hagan (2006), Troposphere-thermosphere tidal coupling as measured by the SABER instrument on TIMED during July– September 2002, J. Geophys. Res., 111, A10S06, doi:10.1029/2005JA011492.

Francis, S. H. (1973), Acoustic-gravity modes and large-scale traveling ionospheric disturbances of a realistic dissipative atmosphere, J. Geophys. Res., 78, 2278– 2301

Frissell, N. A., J. B. H. Baker, J. M. Ruohoniemi, A. J. Gerrard, E. S.Miller, J. P.Marini, M. L. West, and W. A. Bristow (2014), Climatology of medium-scale traveling ionospheric disturbances observed by the midlatitude Blackstone SuperDARN radar, J. Geophys. Res. Space Physics, 119, 7679–7697, doi:10.1002/2014JA019870.

Frissell, N. A., J. B. H. Baker, J. M. Ruohoniemi, R. A. Greenwald, A. J. Gerrard, E. S. Miller, and M. L. West (2016), Sources and characteristics of medium-scale traveling ionospheric disturbances observed by high-frequency radars in the North American sector, J. Geophys. Res. Space Physics, 121, 3722–3739, doi:10.1002/2015JA022168.

Fritts, D. C., and M. J. Alexander (2003), Gravity wave dynamics and effects in the middle atmosphere, Rev. Geophys., 41(1), 1003, doi:10.1029/2001RG000106.

Fritts, D. C., Janches, D., Hocking, W. K., Mitchell, N. J., & Taylor, M. J. (2012). Assessment of gravity wave momentum flux measurement capabilities by meteor radars having different transmitter power and antenna configurations. Journal of Geophysical Research.D.Atmospheres, 117 doi:http://dx.doi.org/10.1029/2011JD017174

Fuller-Rowell, T. J., R. A. Akmaev, F. Wu, A. Anghel, N. Maruyama, D. N. Anderson, M. V. Codrescu, M. Iredell, S. Moorthi, H.-M. Juang, Y.-T. Hou, and G. Millward (2008), Impact of terrestrial weather on the upper atmosphere, Geophys. Res. Lett., 35(9), L09808, doi:10.1029/2007GL032911.

Fuller-Rowell, T. (2014), Physical Characteristics and Modeling of Earth's Thermosphere, in Modeling the Ionosphere-Thermosphere, Geophys. Monogr. Ser., vol. 201, edited by J. Huba, R. Schunk, and G. Khazanov, pp. 13–27, AGU, Washington, D.C., doi:10.1002/9781118704417.

Geller, M.A., M.J. Alexander, P.T. Love, J. Bacmeister, M. Ern, A. Hertzog, E. Manzini, P. Preusse, K. Sato, A. Scaife, and T. Zhou, 2013: A comparison between gravity wave momentum fluxes in observations and climate models. J. Climate, 26, 6383-6405, doi:10.1175/JCLI-D-12-00545.1.

Georges, T. M. (1968), HF Doppler studies of TIDs, J. Atmos. Terr. Phys., 30(5), 735–746, doi:10.1016/S0021-9169(68)80029-7.

Godin, O. A. (2014), Dissipation of acoustic-gravity waves: An asymptotic approach, J. Acoust. Soc. Am., 136, EL411–EL417, doi: 10.1121/1.4902426.

Godin, O. A. (2015a), Finite-amplitude acoustic-gravity waves: Exact solutions, J. Fluid Mech. 767, 52–64, doi: 10.1017/jfm.2015.40.

Godin, O. A. (2015b), Wentzel–Kramers–Brillouin approximation for atmospheric waves, J. Fluid Mech. 777, 260–290, doi: 10.1017/jfm.2015.367.

Godin, O. A., N. A. Zabotin, and T. W. Bullett (2015), Acoustic-gravity waves in the atmosphere generated by infragravity waves in the ocean, Earth, Planets and Space, 67, Art. 47, doi: 10.1186/s40623-015-0212-4.

Gong, Y., and Q. Zhou (2011), Incoherent scatter radar study of the terdiurnal tide in the E- and F-region heights at Arecibo, Geophys. Res. Lett., 38, L15101, doi:10.1029/2011GL048318.

Gong, Y., Q. Zhou, and S. Zhang (2013), Atmospheric Tides in the low-latitude E and F regions and their responses to a sudden stratospheric warming in January 2010, J. Geophys. Res. Space Physics, 118, 7913–7927, doi:10.1002/2013JA019248.

Grocott, A., K. Hosokawa, T. Ishida, M. Lester, S. E. Milan, M. P. Freeman, N. Sato, and A. S. Yukimatu (2013), Characteristics of medium-scale traveling ionospheric disturbances observed near the Antarctic Peninsula by HF radar, J. Geophys. Res. Space Physics, 118, 5830–5841, doi:10.1002/jgra.50515.

Groves, G. V., Hough components of ozone heating, Y. Atmos. Terr. Phys., 44, 111-121, 1982a.

Groves, G. V., Hough components of water vapour heating, J. Atmos. Terr. Phys., •,•,, 281-290, 1982b.

Grubb R. N., Livingston R., Bullett T.W., 2008, A new general purpose high performance HF Radar, URSI General Assembly Commission G Submission and Presentation

A. Guharay , R.Sekar (2011), Seasonal characteristics of gravity waves in the middle atmosphere over Gadanki using Rayleigh lidar observations, Journal of Atmospheric and Solar-Terrestrial Physics73(2011)1762–1770

Gurnett D.A., Bhattacharjee A., Introduction to plasma physics With Space and Laboratory Applications, 2009, Cambridge University Press

Hagan, M. E., and J. M. Forbes, Migrating and nonmigrating diurnal tides in the middle and upper atmosphere excited by tropospheric latent heat release, J. Geophys. Res., 107(D24), 4754, doi:10.1029/2001JD001236, 2002.

Häusler, K., M. E. Hagan, J. M. Forbes, X. Zhang, E. Doornbos, S. Bruinsma, and G. Lu (2015), Intraannual variability of tides in the thermosphere from model simulations and in situ satellite observations, J. Geophys. Res. Space Physics, 120, 751–765, doi:10.1002/2014JA020579

Hunsucker R.D., Radio Techniques for Probing the Terrestrial Ionosphere, 1991, Springer-Verlag

Hernandez-Pajares, M., J. M. Juan, and J. Sanz (2006), Medium-scale traveling ionospheric disturbances affecting GPS measurements: Spatial and temporal analysis, J. Geophys. Res., 111, A07S11, doi:10.1029/2005JA011474.

Hernaandez-Pajares, M., J. M. Juan, J. Sanz, and A. Aragon- Angel (2012), Propagation of medium scale traveling ionospheric disturbances at different latitudes and solar cycle conditions, Radio Science, 47 (6), doi:10.1029/2011RS004951, rS0K05.

Hertzog, A., Boccara, G., Vincent, R. A., Vial, F., & Cocquerez, P. (2008). Estimation of gravity wave momentum flux and phase speeds from quasi-lagrangian stratospheric balloon flights. part II: Results from the vorcore campaign in antarctica. Journal of the Atmospheric Sciences, 65(10), 3056-3070. doi:http://dx.doi.org/10.1175/2008JAS2710.1

Hertzog, A., Alexander, M. J., & Plougonven, R. (2012). On the intermittency of gravity wave momentum flux in the stratosphere.Journal of the Atmospheric Sciences, 69(11), 3433-3448. doi:http://dx.doi.org/10.1175/JAS-D-12-09.1

Hickey, M. P., G. Schubert, and R. L. Walterscheid (2009), Propagation of tsunami-driven gravity waves into the thermosphere and ionosphere, J. Geophys. Res., 114, A08304, doi:10.1029/2009JA014105.

Hines, C. O., Internal atmospheric gravity waves at ionospheric heights, Can. J. Phys., 38, 1441, 1960.

Hines, C. O. and Reddy, C. A. On the Propagation of Atmospheric Gravity Waves through Regions of Wind Shear. J. Geophis. Res. 72, 1015-1034, 1967.

Hocke, K., and N. Kämpfer (2009), Gap filling and noise reduction of unevenly sampled data by means of the Lomb-Scargle periodogram, Atmos. Chem. Phys., 9, 4197–4206, doi:10.5194/acp-9-4197-2009.

Huang, C., S. Zhang, Q. Zhou, F. Yi, and K. Huang (2012), Atmospheric waves and their interactions in the thermospheric neutral wind as observed by the Arecibo incoherent scatter radar, J. Geophys. Res., 117, D19105, doi:10.1029/2012JD018241.

Ishida, T., K. Hosokawa, T. Shibata, S. Suzuki, N. Nishitani, and T. Ogawa (2008), SuperDARN observations of daytime MSTIDs in the auroral and mid-latitudes: Possibility of long-distance propagation, Geophys. Res. Lett., 35, L13102, doi:10.1029/2008GL034623.

Jones Jr., M., J. M. Forbes, M. E. Hagan, and A. Maute (2013), Non-migrating tides in the ionosphere-thermosphere: In situ versus tropospheric sources, J. Geophys. Res., 118, 2438{2451, doi:10.1002/jgra.50257.

Jones, M., Jr., J.M. Forbes, M. E. Hagan, and A. Maute (2014), Impacts of vertically propagating tides on the mean state of the ionosphere-thermosphere system, J. Geophys. Res. Space Physics, 119, 2197–2213, doi:10.1002/2013JA019744.

Kelley M., The Earth's Ionosphere Plasma Physics and Electrodynamics, Second Edition, 2009, Academic Press

Kotake, N., Y. Otsuka, T. Tsugawa, T. Ogawa, and A. Saito (2006), Climatological study of GPS total electron content variations caused by medium-scale traveling ionospheric disturbances, J. Geophys. Res., 111, A04306, doi:10.1029/2005JA011418

Liu, X., J. Xu, J. Yue, and S. L. Vadas (2013), Numerical modeling study of the momentum deposition of small amplitude gravity waves in the thermosphere, Ann. Geophys., 31, 1–14, doi:10.5194/angeo-31-1-2013

Lomb, N. R. (1976), Least-squares frequency analysis of unequally spaced data, Astrophys. Space Sci., 39, 447–462, doi:10.1007/BF00648343.

Lu, X., H.-L. Liu, A. Z. Liu, J. Yue, J. M. McInerney, and Z. Li (2012), Momentum budget of the migrating diurnal tide in the Whole Atmosphere Community Climate Model at vernal equinox, J. Geophys. Res., 117, D07112, doi:10.1029/2011JD017089.

Ma, S. Y., K. Schlegel, and J. S. Xu (1998), Case studies of the propagation characteristics of auroral TIDS with EISCAT CP2 data using maximum entropy cross-spectral analysis, Ann. Geophys, 16, 161–167.

McLandress, C., G. G. Shepherd, and B. H. Solheim, Satellite observations of thermospheric tides: Results from the wind imaging interferometer on UARS, J. Geophys. Res., 101, 4093-4114, 1996.

McLeod, M. A. (1965), Sporadic E theory. I. Collision-geomagnetic equilibrium, J. Atmos. Sci., 23, 96– 109.

Millward, G. H., R. J. Moffett, S. Quegan, and T. J. Fuller-Rowell (1996), A coupled thermosphere–ionosphere–plasmasphere model (CTIP). In: Schunk, R.W. (Ed.), Handbook of Ionospheric Models, STEP Report, 239–279.

Miyoshi, Y., and H. Fujiwara (2008), Gravity waves in the thermosphere simulated by a general circulation model, J. Geophys. Res., 113, D01101, doi:10.1029/2007JD008874.

Mukhtarov, P., and D. Pancheva (2011), Global ionospheric response to nonmigrating DE3 and DE2 tides forced from below, J. Geophys. Res., 116, A05323, doi:10.1029/2010JA016099.

Munteanu, C., Negrea, C., Echim, M. and Mursula, K. (2016), Effect of data gaps: Comparison of different spectral analysis methods, Ann. Geophys., 34, 437-449.

Murphy, D. J., Variations in the phase of the semidiurnal tide over Davis,Antarctica, J. Atmos. Sol. Terr. Phys., 1069 – 1081, 2002.

Negrea, C., M. V. Codrescu, and T. J. Fuller-Rowell (2012), On the validation effort of the Coupled Thermosphere Ionosphere Plasmasphere Electrodynamics model, Space Weather, 10, S08010, doi:10.1029/2012SW000818.

Negrea, C., N. Zabotin, T. Bullett, M. Codrescu, and T. Fuller-Rowell (2016a), Ionospheric response to tidal waves measured by dynasonde techniques, J. Geophys. Res. Space Physics, 121, doi:10.1002/2015JA021574.

Negrea, C., and N. A. Zabotin (2016), Mean spectral characteristics of acoustic gravity waves in the thermosphere-ionosphere determined from Dynasonde data, Radio Sci., 51, doi:10.1002/2015RS005823.

Negrea, C., N. Zabotin, T. Bullett, T. Fuller-Rowell, T.-W. Fang, and M. Codrescu (2016b), Characteristics of acoustic gravity waves obtained from Dynasonde data, J. Geophys. Res. Space Physics, 121, 3665–3680, doi:10.1002/2016JA022495.

Nguyen, N., Liu, Q. H. (1999), The Regular Fourier Matrices and Nonuniform Fast Fourier Transforms, SIAM J. Sci. Comput., 21, 1, 283-293.

Nicolls, M. J., and C. J. Heinselmann (2007), Three-dimensional measurements of traveling ionospheric disturbances with the Poker Flat Incoherent Scatter Radar, Geophys. Res. Lett., 34, L21104, doi:10.1029/2007GL031506.

Nicolls, M. J., M. C. Kelley, A. J. Coster, S. A. González, and J. J. Makela (2004), Imaging the structure of a large-scale TID using ISR and TEC data, Geophys. Res. Lett., 31, L09812, doi:10.1029/2004GL019797.

Nicolls, M. J., S. L. Vadas, J. W. Meriwether, M. G. Conde, and D. Hampton (2012), The phases and amplitudes of gravity waves propagating and dissipating in the thermosphere: Application to measurements over Alaska, J. Geophys. Res., 117, A05323, doi:10.1029/2012JA017542.

Nicolls, M. J., S. L. Vadas, N. Aponte, and M. P. Sulzer (2014), Horizontal parameters of daytime thermospheric gravity waves and E region neutral winds over Puerto Rico, J. Geophys. Res. Space Physics, 119, 575–600, doi:10.1002/2013JA018988.

Oberheide, J., M. E. Hagan, R. G. Roble, and D. Offermann, Sources of nonmigrating tides in the tropical middle atmosphere, J. Geophys. Res., 107(D21), 4567, doi:10.1029/2002JD002220, 2002.

Oberheide, J., J. M. Forbes, K. Ha¨usler, Q. Wu, and S. L. Bruinsma (2009), Tropospheric tides from 80 to 400 km: Propagation, interannual variability, and solar cycle effects, J. Geophys. Res., 114, D00I05, doi:10.1029/2009JD012388.

Oberheide, J., J. M. Forbes, X. Zhang, and S. L. Bruinsma (2011), Climatology of upward propagating diurnal and semidiurnal tides in the thermosphere, J. Geophys. Res., 116, A11306, doi:10.1029/2011JA016784.

Oliver, W. L., S. Fukao, Y. Yamamoto, T. Takami, M.D. Yamanaka, M. Yamamoto, T. Nakamura, and T. Tsuda (1994), Middle and upper atmosphere radar observations of ionospheric density gradients produced by gravity wave packets, J. Geophys. Res., 99(A4), 6321–6329, doi:10.1029/94JA00171.

Oliver, W. L., S. Fukao, M. Sato, Y. Otsuka, T. Takami, and T. Tsuda (1995), Middle and upper atmosphere radar observations of the dispersion relation for ionospheric gravity waves, J. Geophys. Res., 100(A12), 23763–23768, doi:10.1029/95JA02520

Oliver, W. L., S.-R. Zhang, and L. P. Goncharenko (2013), Is thermospheric global cooling caused by gravity waves?, J.Geophys.Res.SpacePhysics,118,3898–3908,doi:10.1002/jgra.50370.

Oliver, W. L., S. Fukao, Y. Yamamoto, T. Takami, M.D. Yamanaka, M. Yamamoto, T. Nakamura, and T. Tsuda (1994), MU radar observations of ionospheric density gradients produced by gravity wave packets, J. Geophys. Res., 99, 6321-6329

Oliver, W. L., S. Fukao, M. Sato, Y. Otsuka, T. Takami, and T. Tsuda (1995), Middle and upper atmosphere radar observations of the dispersion relation for ionospheric gravity waves, J. Geophys. Res.,, 100, A12, 23,763-23,768.

Ortland, D. A., and M. J. Alexander (2006), Gravity wave influence on the global structure of the diurnal tide in the mesosphere and lower thermosphere, J. Geophys. Res., 111, A10S10, doi:10.1029/2005JA011467.

Y. Otsuka, K. Suzuki, S. Nakagawa, M. Nishioka, K. Shiokawa, and T. Tsugawa (2013), GPS observations of medium-scale traveling ionospheric Discussions disturbances over Europe, Ann. Geophys., 31, 163–172, doi:10.5194/angeo-31-163-2013

Park, J., H. Lühr, C. Lee, Y. H. Kim, G. Jee, and J.-H. Kim (2014), A climatology of medium-scale gravity wave activity in the midlatitude/low-latitude daytime upper thermosphere as observed by CHAMP, J. Geophys. Res. Space Physics, 119, 2187–2196, doi:10.1002/2013JA019705.

Paul, A. K., J. W. Wright, and L. S. Fedor (1974), The interpretation of ionospheric radio drift measurements-VI. Angle-of-arrival and group path [echolocation] measurements from digitized ionospheric soundings: The group-path vector, J. Atmos. Terr. Phys., 36, 193214, doi:10.1016/0021-9169(74)90040-3.

Pitteway, M. L. V., and C. O. Hines (1963), The viscous damping of atmospheric gravity waves, Can. J. Phys., 41, 1935– 1948.

Pitteway, M.L.V. and J.W. Wright (1992), Toward an optimum receiving array and pulse-set for the dynasonde, Radio Science.27, 481-490Press, W. H., and G. B. Rybicki (1989), Fast algorithm for spectral analysis of unevenly sampled data, Astrophys. J., 338, 277–280, doi:10.1086/167197.

Press, W. H., and G. B. Rybicki (1989), Fast algorithm for spectral analysis of unevenly sampled data, Astrophys. J., 338, 277–280, doi:10.1086/167197.

Press,W. H., Teukolsky, S. A., Vetterling,W. T., and Flannery, B. P.: Numerical recipes in Fortran, Cambridge University Press, Cambridge, USA, 2 edn., 1992.

Richmond, A. D., and S. Matsushita (1975), Thermospheric response to a magnetic substorm, J. Geophys. Res., 80(19), 2839–2850, doi:10.1029/JA080i019p02839.

Richmond, A. D. (1978), Gravity wave generation, propagation, and dissipation in the thermosphere, J. Geophys. Res., 83(A9), 4131–4145, doi:10.1029/JA083iA09p04131.

Richmond, A. D. (1978), The nature of gravity wave ducting in the thermosphere, J. Geophys. Res., 83(A4), 1385–1389, doi:10.1029/JA083iA04p01385.

Richmond, A. D. (1979), Large-amplitude gravity wave energy production and dissipation in the thermosphere, J. Geophys. Res., 84(A5), 1880–1890, doi:10.1029/JA084iA05p01880.

Richmond, A. (1979), Thermospheric heating in a magnetic storm: Dynamic transport of energy from high to low latitudes, J. Geophys. Res., 84(A9), 5259–5266, doi:10.1029/JA084iA09p05259.

Richmond, A. D. (1995), Ionospheric electrodynamics using magnetic apex coordinates, J. Geomagnetism and Geoelectricity, 47, 191–212.

Rishbeth, H., and O. K. Garriott (1969), Introduction to Ionospheric Physics, International Geophysics Ser., vol. 14, pp. 331, Academic Press, New York.

A. Saito, S. Fukao and S. Miyazaki (1998), High resolution mapping of TEC perturbations with the GSI GPS network over Japan, Geophys. Res. Lett., VOL. 25, NO. 16, PAGES 3079-3082

K. J. F. Sedgemore, P. J. S. Williams, G. O. L. Jones, J. W. Wright (1996), A comparison of EISCAT and Dynasonde measurements of the auroral ionosphere, Ann. Geophysicae 14, 1403-1412,

Scargle, J. D. (1982), Studies in astronomical time series analysis. II. Statistical aspects of spectral analysis of unevenly spaced data, Astrophys. J., 263, 835–853, doi:10.1086/160554.

Scargle, J. D. (1989), Studies in astronomical time series analysis. III. Fourier transforms autocorrelation functions and cross-correlation functions of unevenly spaced data, Astrophys. J., 343, 874–887, doi:10.1086/167757.

Schimmel, M. (2001), Emphasizing difficulties in the detection of rhythms with Lomb-Scargle periodograms, Biol. Rhythm Res., 32(3), 341–346, doi:10.1076/brhm.32.3.341.1340.

Shannon, C. (1948), A mathematical theory of communication, Bell System Tech. J., 27, 379-623.

Shiokawa, K., C. Ihara, Y. Otsuka, and T. Ogawa (2003), Statistical study of nighttime medium-scale traveling ionospheric disturbances using midlatitude airglow images, J. Geophys. Res., 108(A1), 1052, doi:10.1029/2002JA009491.

Stoica, P., Li, J., He, H. (2009), Spectral Analysis of Nonuniformly Sampled Data: A New Approach Versus the Periodogram, IEEE Transactions of Signal Processing, 57, 3, 843-858.

Teitelbaum, H., and F. Vial (1991), On tidal variability induced by nonlinear interaction with planetary waves, J. Geophys. Res., 96 (A8), 14,169-14,178, doi:10.1029/91JA01019.

Thong, T., J. McNames, M. Aboy, and B. Oken (2004), Averaged Lomb Periodograms for Non-uniform Sampling, Conf. Proc., IEEE Eng. Med Biol. Soc., 1, 271–274.

Vadas, S. L., and D. C. Fritts (2005), Thermospheric responses to gravity waves: Influences of increasing viscosity and thermal diffusivity, J. Geophys. Res., 110, D15103, doi:10.1029/2004JD005574.

Vadas, S. L., and M. J. Nicolls (2008), Using PFISR measurements and gravity wave dissipative theory to determine the neutral, background thermospheric winds, Geophys. Res. Lett., 35, L02105, doi:10.1029/2007GL031522.

Vadas, S. L. and Fritts, D. C.: Reconstruction of the gravity wave field from convective plumes via ray tracing, Ann. Geophys., 27, 147-177, doi:10.5194/angeo-27-147-2009, 2009.

Vadas, S. L., and H. Liu (2009), Generation of large-scale gravity waves and neutral winds in the thermosphere from the dissipation of convectively generated gravity waves, J. Geophys. Res., 114, A10310, doi:10.1029/2009JA014108

Vadas, S. L., and G. Crowley (2010), Sources of the traveling ionospheric disturbances observed by the ionospheric TIDDBIT sounder near Wallops Island on 30 October 2007, J. Geophys. Res., 115, A07324, doi:10.1029/2009JA015053.

Vadas, S. L., and M. J. Nicolls (2012), The phases and amplitudes of gravity waves propagating and dissipating in the thermosphere: Theory, J. Geophys. Res., 117, A05322, doi:10.1029/2011JA017426.

Vadas, S. L., H.-L. Liu, and R. S. Lieberman (2014), Numerical modeling of the global changes to the thermosphere and ionosphere from the dissipation of gravity waves from deep convection, J. Geophys. Res. Space Physics, 119, doi:10.1002/2014JA020280.

Yamazaki, Y., and A. D. Richmond (2013), A theory of ionospheric response to upward-propagating tides: Electrodynamic effects and tidal mixing effects, J. Geophys. Res. Space Physics, 118, 5891–5905, doi:10.1002/jgra.50487.

Yigit, E., A. S. Medvedev, A. D. Aylward, P. Hartogh, and M. J. Harris (2009), Modeling the effects of gravity wave momentum deposition on the general circulation above the turbopause, J. Geophys. Res., 114, D07101, doi:10.1029/2008JD011132.

Van Dongen, H. P. A., E. Olofsen, J. H. Van Hartevelt, and E. W. Kruyt (1999), A procedure of multiple period searching in unequally spaced time series with the Lomb Scargle method, Biol. Rhythm Res., 30(2), doi:10.1076/brhm.30.2.149.1424.

Walterscheid, R. L., G. Schubert, and J. Straus (1987), A dynamicalchemical model of wave-driven fluctuations in the OH nightglow, J. Geophys. Res., 92, 1241– 1254.

Walterscheid, R. L., G. G. Sivjee, G. Schuberatnd, and R. M. Hamwey (1986), Large amplitude semi-diurnal variations in the polar mesopause: Evidence of a pseudotide, Nature, 324, 347.

Warner, K., and J. Oberheide (2014), Nonmigrating tidal heating and MLT tidal wind variability due to the El Niño–Southern Oscillation, J. Geophys. Res. Atmos., 119, 1249–1265, doi:10.1002/2013JD020407.

Welch, Peter D., "The use of fast Fourier transform for the estimation of power spectra: A method based on time averaging over short, modified periodograms," Audio and Electroacoustics, IEEE Transactions on , vol.15, no.2, pp.70,73, Jun 1967, doi: 10.1109/TAU.1967.1161901

Wright, J.W. and M.L.V. Pitteway (1979), Real-time data acquisition and interpretation capabilities of the Dynasonde. 1. Data acquisition and real-time display, Radio Sci. 14, 815-825

Wright, J.W., A.K. Paul, and M.L.V. Pitteway (1980), On the accuracy and interpretation of Dynasonde virtual height measurements, Radio Sci. 15, 617-626

Wright, J.W. and M.L.V. Pitteway (1982), Data processing for the Dynasonde: the Dopplionogram, J. Geophys. Res. 87, 1589-1598

Wright, J. W. and M. L. V. Pitteway (1999), A new data acquisition concept for digital ionosondes: Phase-based echo recognition and real-time parameter estimation. Radio Science 34, 871-882

Yuan, Z., R. Fujii, S. Nozawa, and Y. Ogawa (2005), Statistical height-dependent relative importance of the Lorentz force and Joule heating in generating atmospheric gravity waves in the auroral electrojets, J. Geophys. Res., 110, A12303, doi:10.1029/2005JA011315.

Zabotin, N.A., and J. W. Wright (2001), Ionospheric irregularity diagnostics from the phase structure function of MF/HF radio echoes, Radio Science 36, 757-772

Zabotin, N. A., J. W. Wright, and G. A. Zhbankov (2006), NeXtYZ: Three-dimensional electron density inversion for dynasonde ionograms, Radio Sci., 41, RS6S32, doi:10.1029/2005RS003352.

Zhou, Q. H., M. P. Sulzer, and C. A. Tepley (1997), An analysis of tidal and planetary waves in the neutral winds and temperature observed at low-latitude E region heights, J. Geophys. Res., 102, 11491-11505.